NON-DESTRUCTIVE CHARACTERIZATION OF DEGRADATION AND DRUG RELEASE PROCESSES IN CALCIUM POLYPHOSPHATE BIOCERAMICS USING MRI

by

Joshua Bray

Submitted in partial fulfillment of the
requirements for the degree of
Doctor of Philosophy

at

Dalhousie University
Halifax, Nova Scotia
December 2010

DALHOUSIE UNIVERSITY

DEPARTMENT OF PHYSICS AND ATMOSPHERIC SCIENCE

The undersigned hereby certify that they have read and recommend to the Faculty of Graduate Studies for acceptance a thesis entitled "NON-DESTRUCTIVE CHARACTERIZATION OF DEGRADATION AND DRUG RELEASE PROCESSES IN CALCIUM POLYPHOSPHATE BIOCERAMICS USING MRI" by Joshua Bray in partial fulfillment of the requirements for the degree of Doctor of Philosophy.

Dated: December 6, 2010

External Examiner: _____

Research Supervisor: _____

Examining Committee: _____

_____

Departmental Representative: _____

DALHOUSIE UNIVERSITY

DATE: December 6, 2010

AUTHOR: Joshua Bray

TITLE: NON-DESTRUCTIVE CHARACTERIZATION OF DEGRADATION AND DRUG RELEASE PROCESSES IN CALCIUM POLYPHOSPHATE BIOCERAMICS USING MRI

DEPARTMENT OR SCHOOL: Department of Physics and Atmospheric Science

DEGREE: PhD CONVOCATION: May YEAR: 2011

_____

Signature of Author

Table of Contents

List of Tables

List of Figures

List of Abbreviations and Symbols Used

ADC	apparent diffusion coefficient
CPMG	Carr-Purcell Meiboom-Gill
CPMM	calcium polyphosphate, monobasic, monohydrate
CPP	calcium polyphosphate
EPR	electron paramagnetic resonance
FFT	fast Fourier transform
ID	inner diameter
IR	inversion recovery
MIC	minimum inhibitory concentration
MRI	magnetic resonance imaging
MTC	minimum toxic concentration
NMR	nuclear magnetic resonance
OD	outer diameter
PGA	polyglycolic acid
PGSE	pulsed-gradient spin echo
PGSTE	pulsed-gradient stimulated echo
PLA	polylactic acid
PLGA	poly(lactic-co-gycolic) acid
PVA	polyvinyl alcohol
RCVR	receiver
RF	radiofrequency
RMS	root-mean-square
ROI	region-of-interest
SEM	scanning electron microscopy
STE	stimulated echo
TE	echo time
TI	inversion time
TR	repetition time
TSEE	two-site exchange equations

Abstract

A modern approach to the treatment of localized disease involves the use of advanced polymeric or ceramic implant materials for controlled-rate drug delivery. These implants are dynamic systems that maintain drug concentrations within the optimal therapeutic window via complex hydration, swelling, and degradation processes. To optimize the performance of these materials, however, requires a fundamental understanding of the mechanisms that govern drug release. Magnetic resonance imaging (MRI) provides a means of non-invasively characterizing the microstructure and transport properties in this type of material, and has proven to be an invaluable tool for their advancement.

Calcium polyphosphate (CPP) is a biomaterial that has shown promise as a degradable matrix for drug delivery and bone defect repair. Release rates are potentially governed by hydrogelation, swelling, and polymer chain scission. CPP bioceramics have previously been studied using models for drug elution, but these tend to be simplistic and unable to explain the many interrelated mechanisms. Structural analysis techniques have also been applied, but these tend to be inherently destructive and unable to characterize the material *in situ*.

With the aim of characterizing degradation/drug release mechanisms, a non-invasive approach based on MRI was developed and optimized for imaging two existing types of CPP device. Techniques included mapping of the T_1 and T_2 relaxation times and the apparent diffusion coefficient (ADC), which together provide sensitivity to local fluid transport parameters. The non-destructive nature of MRI permitted longitudinal observation, and structural degradation effects were investigated by correlation with concurrent drug elution measurements.

Temporal variation in the release mechanisms was treated by analyzing elution in stages. Large variation between samples was found, but on average, drug elution that was controlled by a structural-relaxation mechanism appeared correlated with the gradual formation of a highly-mobile "free" water component within the disk. Other characteristics, such as swelling rate, did not appear to correlate with drug release at all. While the data did not implicate a singular, governing scheme for drug release from CPP bioceramics, the approach did yield an assessment of the relative importance of the various contributing mechanisms.

Chapter 1

Introduction

With the increasing use of biomaterials for tissue regeneration and controlled drug release, there is a greater need for characterization techniques that can assist with the optimization of these materials. In particular, biodegradable implant materials that obviate the need for surgical removal represent highly dynamic systems that require a non-invasive approach to fully understand the fundamental mechanisms of degradation and drug release. In addition to being a non-invasive tool, magnetic resonance imaging (MRI) offers an arsenal of contrast mechanisms that are sensitive to the chemical and physical microstructure of materials. MRI is therefore a powerful technique for characterizing these materials, and for potentially speeding their development as an effective therapeutic option [1, 2].

The proposed research aims to develop and use an MRI-centered approach to characterize calcium polyphosphate (CPP) bioceramics. CPP is a material that is being developed for an alternative approach to the treatment of chronic, localized bone infections (osteomyelitis) [3–7]. The traditional approach to treatment involves systemic (i.e. oral or intravenous) administration of antibiotics [8–11], but one of the shortcomings of this method is that attempts to achieve therapeutic concentrations at the site of infection easily lead to toxic levels elsewhere in the body [12]. CPP bioceramics are similar in composition to bone [13, 14], and can be loaded with an antibiotic and implanted into the infected bone site. In this way, drug is released locally, where it is needed, and exposure to other tissues and organs is minimized.

In addition to localized drug release, CPP bioceramics also encompass the goals of controlled-rate delivery and biodegradation. A controlled rate is important because it ensures that inhibitory concentrations are maintained, that toxic levels are not exceeded, and that the release can be sustained for the period of time it takes to completely treat the infection [15]. Furthermore, biodegradable materials have the

attractive quality that no surgery is required to remove the device. This is beneficial because it both reduces patient discomfort and reduces the risk of reinfection during surgery [12, 16, 17]. The goals of controlled-rate release and biodegradation are related, because drug is eluted from the device by fluid absorbed from the environment (i.e. the body), and the fluid transport is in turn governed by the physical and chemical microstructure of the implant material. Therefore, to properly optimize CPP bioceramics for drug delivery, an understanding of the relationship between microstructural transformation and drug release behaviour is crucial, and must be obtained in a way that does not disrupt the dynamics of the system [18, p. 12].

Part of the draw of MRI for materials characterization is that it is a non-invasive technique that acquires images of the internal structure of materials [19]. While the spatial resolution is seldom finer than 10 µm [2], the NMR signal relaxation rates are sensitive to microscopic motions of molecules [20]. Moreover, when those molecules are in some confining geometry, such as within a porous solid, the changes in the relaxation times can serve as a probe of that geometry [21, 22]. Specifically, my previously published research demonstrates the proof-of-concept that MRI could be used to map the fluid distribution and the T_1 (spin-lattice) relaxation time in CPP disks immersed in a phosphate buffer [23]. Those experiments showed that changes occur within the CPP microstructure which affect molecular mobility, and that those changes produce a measurable change in the T_1 relaxation time.

Building on this foundation, the aim of the current project is to develop combined protocols for MRI and drug elution measurements that will allow analysis of the drug release in terms of structural changes in CPP biomaterials. In overview, the project can be seen as having three main stages: 1) development of the required magnetic resonance imaging tools, 2) using these and other complementary tools to characterize the CPP morphology and microstructure, and 3) correlating the CPP structure with drug release rates. The remainder of this chapter will provide background related to CPP materials and a survey of MRI techniques that have been used to characterize drug-delivery biomaterials. It will conclude with a short summary of research objectives and a preview of the following 4 chapters.

1.1 CPP Bioceramics for Controlled Release

1.1.1 Controlled Release and Tissue Regeneration

With the exception of intravenous delivery, conventional drug delivery systems release drug rapidly into the system, and the drug must be re-administered in cases where sustained therapeutic levels are required [15].

The primary goal of a controlled release drug delivery system is to reduce the frequency of dosage administration by sustaining a controlled rate of release over a prolonged period of time. The rate of release must be such that drug concentrations remain above the minimum inhibitory (i.e. effective) concentration (MIC), yet do not exceed the minimum toxic concentration (MTC). This range is called the "therapeutic window", and a requirement of a controlled-release system is that it must be able to sustain concentrations in this window for the duration of the treatment [15, 24].

Controlled release systems are characterized by their dominant mechanism of drug release. These may include the following [18]:

1. *Diffusion-controlled systems*: drug diffuses through water-filled pores or through the macromolecular mesh;

2. *Swelling-controlled systems*: drug is dispersed in a glassy polymer and diffuses out as the polymer swells in response to hydration;

3. *Chemically controlled systems*: drug is pendant to or entrapped within macromolecules and is released as these molecules degrade to lower-molecular weight species. The largest concentration of research has gone into this type of system;

4. *Environmentally responsive systems*: the material swelling is controlled by pH, temperature, or magnetic fields.

In actuality, diffusion is nearly always the *basic* mechanism for drug transport, but other mechanisms (related to structural relaxation) may modulate (and/or dominate) the observed release rates. Moreover, the drug release is generally the combined effect of multiple mechanisms, and systems are simply classified by the dominant mechanism.

Controlled release dosage forms exist for oral delivery, or for direct implantation subcutaneously, intraperitoneally, intramuscularly, or within bony tissue [15]. The advantage of direct implantation is that drug delivery is localized.

Several criteria govern the choice of material for an implantable device. Firstly, the material must form a stable interface with the host tissue, which may include chemically bonding with living tissue (bioactive fixation) or ingrowth of tissue into pores and surface irregularities (mechanical fixation). Additionally, the mechanical properties of the implant must be matched to those of the surrounding tissue, and the material must be biocompatible and non-toxic. Frequently, implant materials (especially those used for drug release) are designed to biodegrade naturally so as to eliminate the need for surgical removal. In the case of these materials, the rate of resorption must be matched to the rate of tissue regrowth, and the implant must maintain its strength until the tissue has fully regenerated [15, 18, 24–26]

The kinds of materials used for bone implants are diverse, and include polymers such as poly(lactic-co-glycolic) acid (PLGA) [27, 28] or polymethyl methacrylate (PMMA) [29], oxides of aluminum or zirconium, bioactive glasses [30, 31], and calcium phosphates such as beta-tricalcium phosphate (β-TCP) [32, 33] and hydroxyapatite [34–36]. These materials may be used in the form of particulate matter, beads, bone cement, or bulk implants. The family of calcium phosphate ceramics are of special interest for bone replacement applications because of their similarity to the mineral component of natural bone [24].

One particular type of calcium phosphate is called calcium polyphosphate (CPP), which belongs to a class of materials called the condensed phosphates. These are molecules in which phosphate tetrahedra form chains by sharing corner oxygen atoms of the tetrahedra (Fig. 1.1). Because of this chain-forming ability, CPP is sometimes referred to as an *inorganic polymer* [26, 37]. CPP has been investigated as a material for controlled drug release and bone replacement, and the next section will describe previous research that has been done on this material. The following two sections, respectively, will provide an overview of CPP chemistry and of what is known about CPP degradation. This is of particular importance because a basic understanding of the physical and chemical degradation mechanisms is useful in guiding the approach used in MRI.

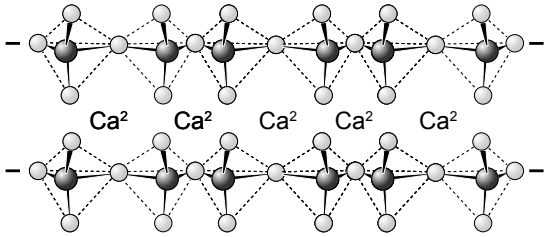

Figure 1.1: Schematic of the calcium polyphosphate (CPP) structure. White spheres represent oxygen and black spheres represent phosphorous (adapted from Dion *et al.* [38]).

1.1.2 CPP Biomaterials

Different forms of CPP have been explored as possible alternatives to degradable polymers or conventional calcium phosphates and glasses, which either lack adequate degradation or strength characteristics [37, 39]. A series of early studies investigating these properties in CPP bioceramics used porous, sintered CPP rods. Fabrication of raw CPP glass involved heating calcium phosphate monobasic, monohydrate crystals, $Ca(H_2PO_4)\cdot H_2O$, to produce a melt, then quenching the melt in deionized, distilled water. The glasses were milled and sieved to obtain powders of various size ranges, which were then sintered to produce CPP rods with different degrees of porosity [17, 26, 39].

Pilliar *et al.* [26] studied the strength, crystallinity, and degradation characteristics of sintered, porous CPP *in vitro* as a function of aging in Tris buffer . The mechanisms of failure were determined by strength testing followed by SEM examination, which showed that fracture occurred predominantly between CPP grains, and very rarely across individual grains. Disks that had undergone aging for different amounts of time showed little variation in strength, although there was a rapid loss in strength during the first day of aging. This was thought to occur because of rapid, preferential degradation of amorphous/poorly-crystallized regions localized at sinternecks. Subsequently, degradation of the crystalline regions also occurred, but at a much slower rate.

Pilliar's *in vitro* results showed that sintered CPP had potential as a degradable bone replacement material, and led to preliminary studies into the feasibility of this

material for bone repair and osteointegration [39]. It was found that CPP rods integrated well with bone, and that the rate of degradation was related to the starting particle size. The authors postulated that the rapid bone ingrowth that occurred in the samples was due to the presence of Ca^{2+} and $(PO_4)^{3-}$ ions as degradation products, which may have accelerated mineralization of the newly-formed bone [40].

The initial work done on CPP involved sintered matrices because of the desire for hard, strong bone replacement materials. Later work, however, done simultaneously by the groups of Filiaggi [41] and Kasuga [42], attempted to develop similar materials using a non-sintering, hydrogelation approach. Filiaggi explored the potential for incorporating a drug into the gelled materials for use in localized therapy. The gentle gelling approach used did not not involve high temperatures, which could otherwise denature the drug.

The gelled CPP ceramics (later referred-to as G1, or "generation 1" disks) were subsequently evaluated for their utility as a drug carrier matrix in a pair of papers by Dion [5,6]. The first of these examined the result of incorporating an antibiotic (vancomycin) on the structural integrity of the gelled matrices, and the second evaluated the drug release. It was found that the incorporation of vancomycin did not alter the strength of the samples, although the strength was ultimately insufficient for typical loads expected in bone. The effect of the gelling protocol was a modulation of drug release rates that permitted some degree of release control. However, there was an initial "burst" of drug from all samples that exceeded the MTC, and the effective antibiotic release period was too short to meet clinical requirements.

To address problems with the strength and drug release characteristics of the G1 disks, Petrone *et al.* [7] sought to develop an improved protocol that introduced a compaction step. The resulting disks (called G2, or "generation 2" disks) were denser and more uniform than G1 disks, and were found to have a more homogeneous distribution of antibiotic. Although the density of the G2 disks was greater than the G1 disks, this did not lead to any appreciable increase in tensile strength. However, the elution characteristics were improved: the G2 disks did not exhibit a burst effect, and it was found that they were capable of sustaining therapeutic concentrations for clinically-relevant time period.

The work done to date on CPP materials illustrates the iterative approach to

bioceramic development. Changes that are made to improve some aspect of the devices may also bring about a loss in some other performance metric. This underlines the importance of a fundamental understanding of the mechanisms that govern the behaviour of the material, which can enable proper optimization of the devices.

1.1.3 The CPP Molecule

Calcium polyphosphates belong to a class of compound called the condensed phosphates. The geometry of the phosphate anion is tetrahedral, and the condensed phosphates form when these tetrahedra share corner oxygen atoms, leading to a P/O ratio greater than $\frac{1}{4}$. Because of the doubly-bonded oxygen in the phosphate ion, only the remaining 3 oxygens are available to join tetrahedra together [13, 43].

The bonding characteristics of the phosphate tetrahedra result in three basic structures. When the molecule is comprised of linear linkages of phosphate tetrahedra, it is called a *polyphosphate*. The degree of polymerization of the polyphosphate chains can range from 2 units to 10^6 units, although the very long chains occur only in crystalline polyphosphates—in glassy polyphosphates the average chain length is only about 20 units [44]. *Cyclophosphates* (also called *metaphosphates*) are ring-shaped structures, and *ultraphosphates* are three-dimensional structures that occur when the molecule contains "branching" phosphate tetrahedra that form three bonds. Because of the instability of these bonds, however, the ultraphosphates degrade quickly in solution to polyphosphates or metaphosphates in solution.

The Ca^{2+} ions in calcium polyphosphate form ionic cross-links between the non-bridging oxygens of neighbouring polyphosphate chains, and chains are terminated by hydroxyl groups [45, 46].

1.1.4 Degradation Mechanisms of CPP Glass

In the presence of water, CPP bioceramics degrade essentially via three mechanisms: chain scission, chain dissolution, and bulk erosion [47].

Chain scission occurs hydrolytically when a water molecule interrupts a P-O-P bond to form two smaller, hydroxyl-terminated chains. This process can eventually lead to the disintegration of the entire chain into orthophosphate ions, PO_4^{3-}. Chain scission is an exothermic process, and is slow at neutral pH, but is faster at higher

temperatures and lower pH [13, 46].

Chain dissolution is a two-part mechanism involving both acid-base reactions and hydration of chains. There are three different acid/base sites on the polyphosphate molecule, and the presence of acids or bases disrupts the ionic interaction between molecules. With the Ca^{2+} cross-links disrupted, water molecules can then form hydrogen bonds with the non-bridging oxygens, although the solubility of CPP glass in water is poor overall [42].

In CPP bioceramics, *bulk erosion* may occur after the material has swollen in response to hydration. Depending on how vigorously the disks are agitated in an *in vitro* environment and depending on how confined the disks are, varying amounts of bulk CPP may erode from the matrix [7].

Ohashi and van Wazer [44] have reported on the length of chains of various dissolved crystalline and non-crystalline CPP materials as estimated using paper chromatography. Glassy CPP was dissolved in Na_2-EDTA (to accelerate dissolution) and the pH was kept in the neutral range to minimize chain hydrolysis. The average chain length was found to be approximately 20 units, and it was noted that there were a particularly large fraction of chains with 5 units (pentapolyphosphate).

Dion *et al.* [5] have studied the changes in chain lengths which occur during gelling and drying of CPP disks both with and without vancomycin incorporated into the fabrication process. This was to determine the effect of drug incorporation on the structure of chains and of exposure time to water. Chain lengths were measured using ^{31}P magic angle spinning (MAS) NMR spectroscopy. Using the chemical frequency shift of different sites on the CPP molecule in the NMR spectra, the relative numbers of internal and chain-terminating phosphates could be inferred and used to estimate average chain lengths. Gelling times from 0 hours to 48 hours were used, and it was found that chain lengths decreased steadily over this period. It was found that an added drying stage resulted in shorter chains, due to the longer exposure to water as the drying took place. Furthermore, the incorporation of vancomycin appeared to have no effect on the length of chains.

In the work involving the addition of the compaction regelling step (G2), Petrone *et al.* [7] studied disks made from three different particle sizes (< 45, $45 - 212$, and $212 - 500$ µm) and three compaction strengths (30, 133, and 452 MPa). In comparison

with G1 disks, these disks showed improved homogeneity and greater density (due to a reduction in porosity). Because of this, the G2 protocol effectively eliminated the "burst" release of drug that was found to take place over the first 8 hours of elution from G1 disks, and the effective release times were prolonged to 3 weeks (as opposed to approximately 1 week for the G1 disks).

One of the most interesting findings of the work by Petrone *et al.* [7] concerns the Higuchi analysis of the release concentrations. In a plot of the concentration against the square root of time, curvature of the plots is indicative of different kinds of release mechanisms. For G1 disks, release was characteristic of a Fickian, or diffusion-controlled release mechanism. G2 disks, on the other hand, which exhibit prolonged drug release, were found to progress through three different stages. In the first stage, release is characterized by a diffusion-controlled mechanism, although at rates much lower than for G1 disks. After some time, there is a transition to a non-Fickian mechanism, where drug release is controlled by structural relaxation. The transition in the release seemed to coincide with visual observation of matrix swelling and a large increase in the release of calcium and phosphate degradation products. After 24 hours, there is a return to a Fickian-controlled release again.

Upon the basis of the established G1 and G2 protocols, Djogbenou *et al.* [48, 49] explored the interactions of the CPP molecule with water. Using mixtures of raw CPP powder with water, it was found that gelling is dependent on the availability of water, both in the amount of water present and the exposure time. Moreover, in addition to a reduction in chain length, gelling also causes conversion to crystalline by-products at longer times. By systematically varying the G1 gelling time during processing, it was shown that some degree of gelling is required to incorporate a drug in the CPP matrix. Conversely, extensive gelling leads to CPP with a very short average chain length. CPP disks made from short-chain material cannot gel further during drug release, and these materials do not show the same release control that the standard G1/G2 formulations do.

The net degradation and release behaviour of the G1 and G2 disks is a function of many different processes and factors, from the molecular to the macroscopic. We wish to shed light on what mechanisms are taking place, observe their shifting importance in time, and understand how they actually determine the drug release. The MRI

techniques contained in the following section all, in some way, characterize the internal transformation that may be taking place, without disrupting the matrix itself, so that the dynamical evolution of the material may be followed *in situ*.

1.2 MRI of Controlled Release Systems and Implant Materials

The body of work on using MRI to study biomaterials is relatively small, and the work by Bray *et al.* [23] is the only one to date that has reported on CPP bioceramics. Other studies have focused primarily on polymers for both oral delivery and implantable controlled release devices, with a few studies dedicated to degradable tissue scaffolds. Despite differences in materials and function, the same MRI methods have potential for characterizing CPP matrices, and it is worthwhile to examine what has been learned about these other materials using MRI. This section contains reference to several MRI-related concepts, and the reader is referred to Chapter 2 for a full discussion of these ideas.

1.2.1 Imaging Oral Controlled Release Devices

Several groups have used various MRI approaches to characterize the changing structure and behaviour of hydroxypropylmethylcellulose (HPMC) tablets. [50–54]. These tablets are water-swellable, hydrophilic matrices that may be loaded with a therapeutic agent and administered orally for controlled-rate release. The rate-controlling mechanism is a gel layer that forms on the surface of the tablets when they are exposed to water, limiting further fluid ingress and acting as a diffusional barrier to drug release. Although it is possible to partially characterize swelling behaviour using optical photography, this method cannot resolve the relative contributions of gel-layer and core expansion. In one paper by Rajabi-Siahboomi *et al.* [50], spin echo imaging is used to acquire two-dimensional images of fluid density that are used to study fluid ingress into the tablets *in situ*.

A subsequent paper by the same group [51] expands the MRI characterization techniques to include spatially-resolved profiles of the apparent diffusion coefficient (ADC) and the T_2 relaxation parameter. Both of these quantities are strongly dependent on local water mobility, which has a bearing on polymer hydration, drug dissolution, and drug release.

Further characterization of the gel layer in HPMC was done by Fyfe *et al.* [52], who devised a method for obtaining quantitative local polymer concentrations from measurements of the T_1 and T_2 (spin-spin relaxation time) of water absorbed into the matrix. It is a characteristic of polymers that the NMR signal lifetime is often very short, and this makes direct imaging difficult. Alternatively, water molecules in swollen, hydrophilic polymers like HPMC experience a reduction in mobility via hydrogen bonding interactions with the chains, and this can be detected by a change in the water relaxation times. The authors exploited this fact to obtain a calibration for determining polymer concentration from the relaxation times of imbibed water.

With swelling, diffusion, and polymer concentration in the HPMC gel layer already characterized, Fyfe *et al.* [53] turned their attention to investigating the actual transport of drug from HPMC tablets. Measurements of drug transport have traditionally been limited to sampling the concentration of drug released into solution, but MRI offers the capability to directly detect the drug distribution within the matrix itself. The authors used this capability to investigate two different mechanisms for drug release: diffusion through the swollen polymer and release of drug at the edges of the tablet through erosion.

In a recent paper, Dahlberg *et al.* [54] revisited the problem of studying the concentration and dynamics of HPMC polymers and their relation to drug release. They devised *in situ* NMR methods that combined direct imaging of the HPMC matrix with measurement of the released drug concentration. As mentioned previously, direct polymer imaging is made challenging because of the short T_2 relaxation times of polymers. The authors circumvented this issue by using heavy water as a deuterated solvent and by using a constant-time imaging (CTI) technique [55]. The CTI sequence acquires signal a single point at a time, allowing for ultra-short delays between excitation and acquisition, which is important for detecting short-T_2 species. The concentration of drug released was measured *in situ* via a spectroscopic technique whereby the HPMC tablet is shifted out of the RF coil, and an NMR spectrum of the drug in solution is acquired.

1.2.2 Imaging Implantable Controlled Release Devices

Several synthetic polymers presently in use as biodegradable implant materials are also useful as drug delivery matrices. These include polylactic acid (PLA), polyglycolic acid (PGA), poly(lactic-co-glycolic) acid (PLGA), and polyvinyl alcohol (PVA), to name but a few. These materials offer excellent biocompatibility and biodegradation properties, and can be used in the form of microspheres, microcapsules, nanoparticles, pellets, implants, and films [27]. Some of the studies using MRI to study these materials are discussed here.

Following theoretical work on the dissolution of polymers, Snaar *et al.* [56] have used MRI to study water absorption and ADC in hydrating PVA matrices designed for drug delivery. Previous theoretical work has suggested that reptation—the snake-like disentanglement of chains in a hydrating polymer—is an important mechanism for the dissolution of biodegradable polymers [57]. This theoretical model predicts a change in the diffusion mode as the dissolution proceeds, and the imaging results showed that there is indeed a change in the diffusion mechanism as the PVA becomes progressively more hydrated.

PLGA materials intended for implantable drug delivery systems have been reported to degrade via a mechanism whereby acidic products generated by the polymer degradation accumulate in the inner region of the device and catalyze the hydrolytic scission of chains. A similar mechanism has been observed in CPP glasses [46]. Because the acid-catalyzed reaction occurs preferentially in the center of the disk, this leads to non-uniform degradation of the material, which was investigated by Djemai *et al.* [28] using MRI of the fluid penetrant concentration and ADC.

Milroy *et al.* [58] used MRI to seek evidence of a four-stage degradation model for PGA disks postulated in a previous paper. The stages include 1) initial water absorption, 2) polymer chain scission, 3) propagation of erosion fronts, and 4) a stage in which the erosion fronts meet . As in the study done by Djemai *et al.* [28], drug elution measurements are conducted in conjunction with MRI to draw correlations between the transport of fluid and the drug release.

The NMR signal comes from the magnetic moments of atomic nuclei, but the same principles can be used to obtain signal from the spins of unpaired electrons. This

technique is called Electron Paramagnetic Resonance (EPR), and can be used to non-invasively detect drug-derived free radicals and to study the impact of antioxidants on them. Mäder *et al.* [59] have used both MRI and EPR to obtain complementary information on the *in vitro* and *in vivo* degradation of poly(fatty acid dimer–sebacic acid), P(FAD–SA). The MRI was performed to assess changes in the morphology of P(FAD–SA) during degradation, and the EPR spectra were acquired to detect the mobility of a drug loaded in the material. The additional utility of EPR is that pH measurements can be done non-invasively as well. The results of this study underline the important differences that can occur with *in vitro* and *in vivo* degradation studies, and how the non-invasive character of MRI allows it to be used for both kinds of study.

1.2.3 Imaging Materials for Tissue Repair

In the only imaging study that was found to study a calcium phosphate implant, Ramanathan *et al.* [60] used solid-state ^{31}P MRI to quantitatively measure the mass of hydroxyapatite in orthopedic implant materials. The aim of the study was to devise a way to selectively image the implant material in the presence of bone. The difference in T_1 of hydroxyapatite and bone is substantial (1.8 seconds for hydroxyapatite and 15 seconds for bone at the field strengths used), and this fact was used for selective imaging. Using materials of different density, it was found that image intensity varied linearly with density, showing that MRI is capable of following the resorption and remodeling of calcium phosphate implants *in vivo*.

A study of poly(3–hydroxybutyrate–3–hydroxyvalerate) (PHBHV) by Marcos *et al.* [61] uses MRI, relaxometry, and diffusometry in concert with optical microscopy and electron microscopy (SEM) to characterize the porosity in these materials, which are intended for use as morphologic guides for tissue regeneration. Like CPP and the degradable polymers discussed above, degradation of PHBHV chains occurs by hydrolytic scission, and the authors sought to characterize the chemical and physical changes arising from the aging process. The MRI was performed on porous PHBHV samples immersed in phosphate buffered saline (PBS), and the signal intensity in the images was used to quantify the average open porosity in the materials. These results were then compared to optical images, and it was determined that the MRI porosity measurements agreed fairly well with the macroporosity observed by the

optical measurements. The SEM results showed microporosity in the disks as well, and the variations in T_1 and T_2 (measured in bulk) could be explained by a gradual filling of the micropores over time.

1.2.4 Imaging CPP Bioceramics

As was mentioned previously, the only imaging studies of CPP bioceramics so far have been performed by our group [23]. This work involved maps of fluid concentration and T_1 relaxation times in hydrating CPP disks. Both G1 and G2 disks were studied, so as to determine if the imaging methods could resolve differences in the microstructures of differently-processed materials. The disks, each 4 mm in diameter, were sealed into place in NMR tubes (4 mm I.D.), and the sides and bottom sealed to ensure only 1-D transport of phosphate buffer. Images were acquired using a spin echo sequence and an inversion-recovery sequence to produce maps of fluid density and T_1 relaxation times, respectively, over an extended time period. For this preliminary work, blank disks (not loaded with an antibiotic) were used, so as to focus attention on the CPP microstructure.

The fluid concentration maps showed that the buffer was absorbed in two stages: one involving rapid absorption of low concentrations of fluid in the first hour, then another involving a slower front of hydration that penetrated inwards from the exposed face of the disk over several days until the fluid level reached saturation. The amount of fluid absorbed in the early stages was less for G2 disks than for G1 disks, which was attributed to the lower initial porosity of the compacted G2 disks. The fluid maps at this time were also much smoother in the more homogeneous G2 disks. The rate at which the fluid front penetrated the disks was greater for the G2 disks, but resulted in a lower saturation level overall than in the G1 disks.

The T_1 maps revealed additional differences between the two types of disks. The T_1 was found to have two exponential components (i.e. biexponential), indicative of multiple microenvironments within the material with different relaxation times, with water exchange between the two environments [21]. From what is known about the CPP molecule, and from the observation that one of the relaxation components is very close to that of free water, it was hypothesized that one component is water of hydration on the CPP molecules and the other component is due to water that can

diffuse freely, with exchange between the two governed by the extent of degradation. The major difference between the two types of disks is that, initially, there is both a long and short component of T_1 in the G1 disk, but in the G2 disk, there is only a single component (with about the same magnitude as the short G1 component). After some time this changes, and a long component forms in the G2 disk as well, indicating that the second microenvironment is then detected.

Further changes in both the long and short T_1 components are brought on by changes in the mobility of water molecules that occur due to microstructural changes taking place in the material. An observation of special interest is that the fluid density maps reach a state of equilibrium fairly early on, and subsequent changes to the T_1 maps are therefore not associated with more buffer being absorbed into the matrix.

1.3 Characterizing Mechanisms of Degradation and Drug Release in CPP Bioceramics

A successful drug delivery biomaterial is one that can sustain concentrations in the therapeutic window between the inhibitory and the toxic concentration levels. Particularly when this target is narrow, optimization of this type of device requires understanding both the mechanisms of degradation in the physical/chemical microstructure as well as how degradation affects drug release.

Previous techniques for characterizing release mechanisms in CPP bioceramics have relied on interpretation of elution curves or the use of destructive techniques. However, mechanisms inferred from bulk drug transport are overly simplistic, and do not account for the specific effect of the microstructure. Destructive methods, by definition, alter the material, and cannot be used for *in situ* characterization. MRI techniques can uniquely benefit the study of CPP materials because they allow repeated observation of a sample over its entire lifetime, and the available contrast mechanisms offer sensitivity to the internal microstructure.

The present work focusing on CPP aims to use an MRI-centered approach to study mechanisms of degradation and drug release in CPP bioceramics. This larger goal is broken into three main stages, which are presented here along with points highlighting the major objectives and hypotheses in each one.

Stage 1: Development and optimization of techniques

While CPP has already been studied in our previously-published work using fluid density and T_1 mapping techniques, there are advantages to mapping the T_2 and ADC parameters as well. The T_2 relaxation time, like T_1, is sensitive to molecular tumbling motions, but it offers greater sensitivity to exchange between different microenvironments and has the potential to better differentiate between high- and low-mobility water involved in drug transport. The ADC is of interest because it represents translational fluid self-diffusion on a local scale, which is potentially related to the bulk time-release of drug.

The first stage will be the development and optimization of protocols for T_2 and ADC imaging so that the complementary information they provide can be used for more detailed characterization of the CPP microstructure.

Objective 1 Develop and optimize non-invasive techniques for characterizing CPP bioceramics.

Hypothesis 1.1 MRI methods can spatially and temporally resolve microstructural and fluid transport properties in CPP bioceramics.

Hypothesis 1.2 Previously-reported drug elution protocols can be adapted to the physical constraints associated with the MRI apparatus.

Stage 2: MRI-based characterization of morphology and microstructure

The primary aim of the second stage will be to form a more complete picture of degradation in CPP using MRI techniques. In addition to the microstructure, however, drug release is potentially affected by mechanisms related to bulk morphological changes (i.e. swelling and bulk erosion). Previously, CPP has been found to exhibit stages in the swelling and bulk erosion [7, 23], and by analyzing the MRI in these stages separately, we aim to consider periods dominated by a single mechanism of morphological change.

In stage 2 of this thesis, MRI mapping of relaxation times (T_1 and T_2) and the ADC will be used to study different aspects of the microstructure, and optical photography will be used to characterize swelling and bulk erosion.

Objective 2 Describe the physical characteristics of CPP bioceramics exposed to a buffer fluid.

Hypothesis 2.1 Stages of morphological change can be identified using optical photography to define stages for MRI analysis of microstructural degradation.

Hypothesis 2.2 Measurements of T_2 will better resolve free- and bound-water contributions to the MRI signal than measurements of T_1.

Hypothesis 2.3 The ADC (sensitive to material properties on the micron scale) can be used to infer information complementary to relaxation times (sensitive to material properties on the molecular scale) pertaining to local microstructural length scales in CPP.

Stage 3: Correlating drug elution with physical characteristics of CPP

The third and final stage will be to correlate drug elution with structure as a means of understanding release mechanisms. This involves development of a protocol for drug elution measurements that is compatible with concurrent MRI acquisition. By comparing the drug release with the physical characteristics on an average and on an individual level, we aim to elucidate the factors of greatest importance in drug release from CPP bioceramics.

Objective 3 Perform concurrent drug elution, optical, and MRI measurements on CPP loaded with vancomycin.

Hypothesis 3.1 Macroscopic changes due to swelling and bulk erosion, observed via optical photography, will correlate with differing rates of release.

Hypothesis 3.2 Changes observed at a local microstructural level using MRI relaxation/ADC measurements will show temporal changes in the proportion of free/bound water.

Hypothesis 3.3 Changes in the proportion of free/bound water will correlate with a structural relaxation-dominated contribution to drug release.

* * *

The three stages described here are presented in detail in chapters 3, 4, and 5, respectively. The necessary background in MRI theory is presented in chapter 2.

Chapter 2

Physics of Magnetic Resonance Imaging, Relaxation, and Diffusion

The impact of magnetic resonance imaging (MRI) on the modern world has been enormous. Particularly in the domain of medical imaging and diagnosis it is a mainstay, offering a safe and non-invasive method for three-dimensional imaging of the body, plus sensitivity to a broad range of soft tissue properties. Diagnosis of cancer, stroke, and other forms of tissue damage is possible and routine with modern MRI.

For the same qualities that make it a powerful medical imaging modality, MRI is an important tool in numerous other scientific fields as well. It has been used in the diverse realms of materials engineering, oil exploration, polymer physics, plant biology, food science, and in the study of biomaterials and controlled-release devices. MRI is capable of non-destructively providing information about the absorption of fluid into materials such as CPP, as well as probing the microstructure via relaxation times and diffusion coefficients.

The purpose of this chapter is to to describe the MRI theory used for *in vitro* imaging of water-saturated CPP bioceramic materials. MRI techniques are based upon the phenomenon of nuclear magnetic resonance (NMR), so the description will begin with a basic review of NMR physics and signal acquisition. This will be followed by sections on NMR relaxation measurement, imaging and k-space, and diffusion. In the last section, all of the concepts will be put together to describe the series of four MRI techniques used in the present work characterizing the physical/chemical microstructure of CPP bioceramics.

As an added note, there is some ambiguity in the use of the term NMR. Strictly speaking, it refers to the phenomenon of resonant absorption/emission of energy by atomic nuclei. In common usage, however, it is also taken as a short form for NMR spectroscopy. In the present discussion, the term NMR will be used for the *general* resonance phenomenon, and any reference to spectroscopy will be stated explicitly.

2.1 Spin, Magnetization, and the NMR Signal

2.1.1 Nuclear Magnetism and the Origin of the NMR Signal

NMR techniques (imaging and spectroscopy) are based on a quantum phenomenon—namely, the Larmor precession of nuclear magnetic moments in a strong magnetic field. Despite this, however, the NMR signal is never in practice observed from just one, or even a small number of nuclei. In a sense, then, it is a macroscopic effect, and can be described while largely ignoring quantum principles. There are exceptions, of course, such as MRI of nuclei with spin $\neq \frac{1}{2}$. Most MRI, however, is done on hydrogen nuclei (spin $\frac{1}{2}$), for which a deep quantum understanding is not necessary. Accordingly, then, this section will begin with a brief explanation of quantum spin and angular momentum, but thereafter will largely take a semi-classical perspective.

Angular Momentum

The spin of a *classical* body is the angular momentum that it possesses due to rotation about it own axis. The spin angular momentum of an *elementary* particle such as a proton, neutron, or electron is different, however, in that it does not actually involve physical rotation of the object. The electron is a perfect illustration, as it is not even believed to have any spatial extent whatsoever, so any similarity with classical spin is purely mathematical [62].

Quantum spin is a vector quantity, with components S_x, S_y, and S_z. Although it is possible to obtain eigenvalues and eigenfunctions for any component of $\vec{S}$, the three components are mutually incompatible observables, meaning only one of them can be known at a time. Quite arbitrarily, the z component may be chosen as the observable, and its eigenequation written as

$$S_z\psi = \hbar m\psi, \tag{2.1}$$

with ψ being the wave function for some particle (the meaning of m will be described below). The symbol $\hbar$ is Plank's constant.

Though the components are mutually incompatible, the *total spin angular momentum squared*, S^2, is compatible with the three components. Its eigenequation is

$$S^2\psi = \hbar^2 s(s+1)\psi. \tag{2.2}$$

Here, the value s is called the *spin quantum number* and is what is most often meant when referring to "spin". It is a non-negative integer or half-integer that is characteristic of the particle. In particular, electrons, neutrons, and protons all have spin $\frac{1}{2}$. This fact again demonstrates the profound difference between classical and quantum spin, because it implies that the magnitude of a particle's spin angular momentum is an intrinsic and immutable property of that particle, just like its mass or its charge.

The value m can take on integer-spaced values from $-s$ to $+s$. That is,

$$m = \ -s,\ -s+1,\ -s+2,\ \cdots\ +s-1,\ s. \tag{2.3}$$

For a spin-$\frac{1}{2}$ particle, that means that S_z can take on two possible values: $+\frac{\hbar}{2}$ or $-\frac{\hbar}{2}$. These states are often referred to respectively as "spin-up" and "spin-down".

Nuclear Magnetism

A particle possessing spin also possesses an associated magnetic moment. This is equally true for fundamental particles, such as electrons, muons and quarks, as well as for all kinds of "composite" particles like protons, atomic nuclei, and whole atoms. Though it has already been stated that quantum spin is not related to any *real* rotation, this concept can be illustrated by thinking of a charged particle (e.g. a positively charged atomic nucleus) as a spinning sphere. Because of the circulating charge, a dipolar magnetic field exists about the nucleus, which is described by a magnetic dipole moment ($\vec{\mu}$). The relation between a particle's spin and its magnetic moment is

$$\vec{\mu} = \gamma \vec{S} \tag{2.4}$$

where the constant of proportionality (γ) is called the gyromagnetic ratio, and is specific to and characteristic of a given nuclear species. The values of γ for several important NMR nuclei are given in Table 2.1. Also included is the related constant γ, which is defined as follows:

$$\gamma = \frac{\gamma}{2\pi} \tag{2.5}$$

Nucleus	γ ($\times 10^6$ rad/s/T)	γ (MHz/T)
^{1}H	267.5	42.58
^{13}C	67.2	10.7
^{17}O	36.	5.8
^{19}F	251.	40.0
^{23}Na	71.0	11.3
^{31}P	108.	17.2

Table 2.1: The gyromagnetic ratio for several nuclei important in NMR [63]

Zeeman Splitting

The phenomenon of nuclear magnetic resonance is based upon the observation that magnetic fields cause the nuclear spin energy levels to exhibit Zeeman splitting. In the *absence* of a field, there is no preferential direction of alignment for the magnetization, so the "spin-up" and "spin-down" states are degenerate in energy. When a magnetic field, $\vec{B}$, is present however, a particle will have an energy that depends on the orientation of its nuclear magnetic moment. The Hamiltonian for such a particle is

$$H = -\vec{B} \cdot \vec{\mu}. \tag{2.6}$$

Arbitrarily choosing the field direction to be along the z axis, the field vector can be written as $\vec{B} = B\hat{z}$, where B is the magnitude. The Hamiltonian can thus be rewritten as

$$H = -(B\hat{z}) \cdot \vec{\mu} = -B\mu_z. \tag{2.7}$$

From equation 2.4,

$$\mu_z = \gamma S_z, \tag{2.8}$$

and because $S_z = \hbar m$, the Hamiltonian becomes finally

$$H = -\gamma \hbar m B. \tag{2.9}$$

For a spin-$\frac{1}{2}$ system, $m = \pm\frac{1}{2}$, so the energy of the spin-down state is

$$H_- = +\frac{\gamma\hbar}{2}B,$$

and the energy of the spin-up state is

$$H_+ = -\frac{\gamma\hbar}{2}B.$$

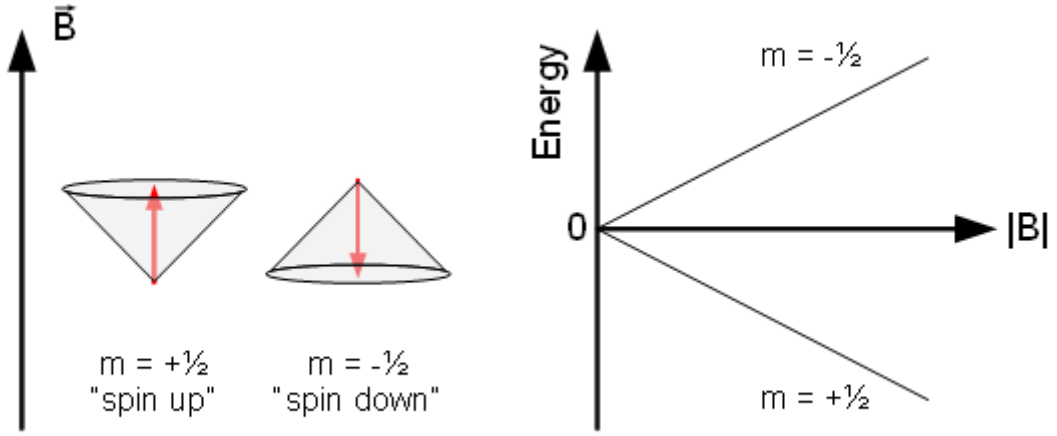

(a) (b)

Figure 2.1: (a) Spins align with their z component either parallel ("spin-up") or antiparallel ("spin-down") to the magnetic field, $\vec{B}$. The quantized z component of spin is shown in red, and the cones illustrate that the x and y components are incompatible observables, and remain uncertain. (b) When $B = 0$, the spin-up and spin-down states are degenerate in energy, but they diverge as B increases.

It should be noted that it is common to refer to nuclear spins/magnetic moments as being "parallel" or "antiparallel" to the field depending respectively on whether they are in the spin-up or spin-down state. This terminology is not strictly accurate, because it suggests that the spin vector itself lies parallel or antiparallel to the field, when in reality it is only the z component that points with or against the field (Fig. 2.1).

Boltzmann Polarization

A macroscopic sample of material contains a large number of nuclei, and in a strong magnetic field each nucleus is polarized as described in the preceding section. Although there is a tendency for nuclear spins to occupy the lower energy (spin-up) level, random thermal fluctuations ensure that a certain fraction occupies the higher (spin-down) level. With the approximation that the spins are not mutually interacting, their distribution between the two available energy levels is governed by Boltzmann statistics.

For a system of N spins in equilibrium at temperature T, which are divided into energy levels ϵ_i, the Boltzmann equation gives the fractional number of spins (f_i) in each level [19].

$$f_i = \frac{N \exp(-\epsilon_i/kT)}{\sum_j \exp(-\epsilon_j/kT)} \tag{2.10}$$

The sum in the denominator is just the partition function, which is a constant. If N_+ and N_- are, respectively, the number of spins parallel and antiparallel to the field, we have the following:

$$\frac{N_+}{N_-} = \frac{f_+}{f_-} = \frac{N \exp\left(-\left(-\frac{\gamma\hbar}{2}B\right)/kT\right)}{N \exp\left(-\left(+\frac{\gamma\hbar}{2}B\right)/kT\right)} \tag{2.11}$$

$$= \exp\left(\gamma\hbar B/kT\right)$$

For an ensemble of hydrogen nuclei (^{1}H) in typical experimental conditions,

$$B = 11.7\,\mathrm{T} \quad T = 293\,\mathrm{K} \quad \gamma_{^1\mathrm{H}} = 2.676 \times 10^8\,\mathrm{rad/s/T}$$

the value of $\frac{N_+}{N_-}$ is 1.000095, corresponding to a 0.0095% excess of spins parallel to the field. This implies that, although there are a large number of nuclear spins in a macroscopic sample (on the order of Avogadro's number), the numbers of spins parallel and antiparallel to the field are nearly equal. Nevertheless, the slight excess that are aligned with the field add together to give the object a net magnetization, $\vec{M}$. Though this small magnetization is detectable, NMR is comparatively a low-sensitivity method.

The techniques of NMR all in some way involve influencing the spin system, then measuring the time-evolution of the magnetization. Because of the great number of spins in most systems of interest, it is seldom necessary to pay detailed attention to the quantum nature of the phenomenon, and as mentioned previously, it suffices to treat the spins semi-classically.

Larmor Precession

From classical electromagnetism, it is known that a loop of electric current creates a dipolar magnetic field, which can be described by a magnetic moment, $\vec{\mu}$. If placed in a magnetic field, the sum of all forces on the loop will cancel out, leaving no net

force. There will remain a torque ($\vec{T}$), however, whose magnitude depends on $\vec{\mu}$, $\vec{B}$, and their orientation with respect to one another.

$$\vec{T} = \vec{\mu} \times \vec{B}, \tag{2.12}$$

This expression, although originally for a current loop dipole, can actually be extended to apply to *any* magnetic dipole, including the magnetic moments of nuclei.

Newton's law allows for torque to be written as the time derivative of angular momentum. For the spin angular momentum of a nucleus ($\vec{S}$), this becomes

$$\vec{T} = \frac{d\vec{S}}{dt}. \tag{2.13}$$

Combining the previous two equations yields

$$\frac{d\vec{S}}{dt} = \vec{\mu} \times \vec{B}. \tag{2.14}$$

Using the equation relating $\vec{\mu}$ and $\vec{S}$, ($\vec{\mu} = \gamma\vec{S}$), the last equation can be rewritten as

$$\frac{d\vec{\mu}}{dt} = \gamma\vec{\mu} \times \vec{B}. \tag{2.15}$$

Re-writing this as a scalar equation (rather than in vector form), one obtains

$$\frac{d\mu}{dt} = \gamma\mu B \sin\theta \tag{2.16}$$

where θ is the angle between the vectors $\vec{\mu}$ and $\vec{B}$.

In an infinitesimal time dt, the vector $\vec{\mu}$ will change by an amount $d\vec{\mu}$, perpendicular both to itself and to $\vec{B}$. This results in precessional rotation of the vector, with a corresponding infinitesimal angle of rotation $d\phi$. By consideration of the geometry of the inclined $\vec{\mu}$, it is easily obtained that the angle $d\phi$ is given by

$$\mu \sin\theta d\phi = d\mu \tag{2.17}$$

By equating this result with the previous equation, one obtains

$$\mu \sin\theta d\phi = \gamma\mu B \sin\theta dt, \tag{2.18}$$

which can subsequently be rearranged to obtain

$$\frac{d\phi}{dt} = \gamma B. \tag{2.19}$$

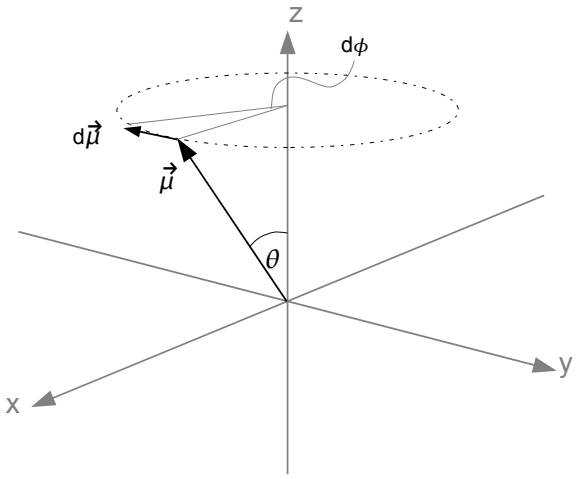

Figure 2.2: Precession of a dipole in a magnetic field. The $\vec{B}$ field is not shown, but points along the z axis.

Since $\frac{d\phi}{dt}$ is the angular velocity, ω, we now have an equation linking precessional frequency to the magnetic field—the Larmor equation. All that remains is to establish the direction, and this is done by examination of the coordinate system in Fig. 2.2. Using the standard convention that a positive rotation is one that would cause the advance of a right-hand screw along the positive z axis, the *vectorial* Larmor equation has an additional negative sign.

$$\vec{\omega} = -\gamma \vec{B} \tag{2.20}$$

This equation embodies the fundamental idea of MRI. It says that the frequency of precession varies linearly with magnetic field through a constant of proportionality (γ) that is characteristic of the nuclear species being imaged. It also shows that the Larmor frequency is independent of the angle of inclination, θ.

In practice, it is common to express equation 2.20 as an ordinary frequency (f, in Hz) rather than an angular frequency (ω, in rad/s), and to prefer a scalar equation that leaves the precessional direction implicit.

$$f = \gamma B \tag{2.21}$$

Given that γ for protons is 42.57 MHz/T, and that actual fields used in NMR fall into a range from about 0.1 T to 20 T, this puts the Larmor frequency in the radiofrequency

range.*

2.1.2 Basic NMR Signal Acquisition

The previous section introduced the concepts of nuclear magnetism and how spin dipoles in a magnetic field undergo Larmor precession. The magnetization of a macroscopic object, though, comes from the additive effects of a large quantity of spins, and it will therefore precess as well. Although due to a vanishingly small excess of spins in the $+\frac{1}{2}$ state, it remains possible to detect the time-varying magnetization in a receiver coil, and this is the NMR signal.

To explain magnetization, consider a volume V in a sample, where V is small enough that the magnetic field can be considered to be essentially uniform throughout V. In this case, V can be considered a "spin isochromat", which simply means that the Larmor precessional frequency is the same for all of the spins. The magnetization is the sum of all the spin magnetic moments within V, and its equation of motion is

$$\frac{d\vec{M}}{dt} = \gamma \vec{M} \times \vec{B}_{\text{eff}}. \tag{2.22}$$

This equation is nearly identical to the one for individual spins dipoles (equation 2.15), save that $\vec{\mu}$ has been replaced by the magnetization ($\vec{M}$), and the magnetic field is written as $\vec{B}_{\text{eff}}$ to highlight the fact that it may be the sum of more than one type of field. The kinds of fields that add together to produce $\vec{B}_{\text{eff}}$ can include the main static field, magnetic interactions between spins, and radiofrequency (RF) fields used to excite the spins.

In the simplest conceptual case, interactions between spins are neglected, and the effective field is just the strong, static background field. By convention, this field is referred to as B_0 and lies along the $+z$ axis.

$$\vec{B}_{\text{eff}} = B_0 \, \hat{z} \tag{2.23}$$

A general magnetization vector can be written in terms of components aligned along the field and transverse to the field, as in Fig. 2.3.

$$M_z = M \cos\theta \tag{2.24}$$

$$M_\perp = M \sin\theta \tag{2.25}$$

*medical imagers fall in a narrower range, from about 1 T to 7 T

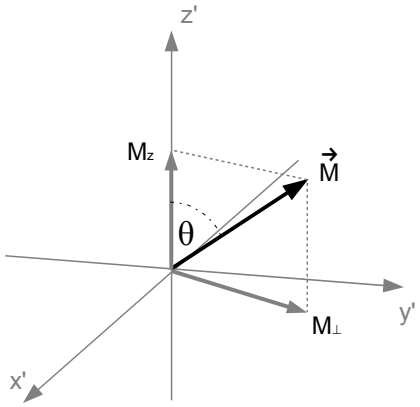

Figure 2.3: Magnetization, $\vec{M}$ can be broken into longitudinal (M_z) and transverse ($M_\perp$) components

Doing so allows the equation of motion to be re-written in the following way.

$$\frac{dM_z}{dt} = 0 \tag{2.26}$$

$$\frac{d\vec{M}_\perp}{dt} = \gamma \vec{M}_\perp \times (B_0\,\hat{z}) \tag{2.27}$$

The solution to these decoupled equations is that the z component remains static while the transverse component precesses at the Larmor frequency. As a convention throughout the rest of this chapter, the nominal Larmor frequency associated with the B_0 field will be referred to as $\omega_0 = \gamma B_0$.

As already mentioned, the above assumes that the only interaction is between the spins and the B_0 field. Other interactions include additional applied fields (such as RF pulses), as well as the mutual interactions of spins, which give rise to NMR relaxation. Concepts related to RF pulses and signal detection are described in the following section, and the physics of NMR relaxation and its effect on the signal is covered in the section after that (§2.1.4).

2.1.3 Radiofrequency Excitation and Detection

For a sample volume in a B_0 field, the equilibrium condition is one in which the magnetization $\vec{M}_0$ is static and aligned along the field direction. Before signal may be acquired, the magnetization must be "tipped" with respect to the $\vec{B}_0$ field, causing it to precess. This is accomplished using an RF probe, which creates a powerful burst of polarized radio waves at the Larmor frequency to introduce a strong magnetic field

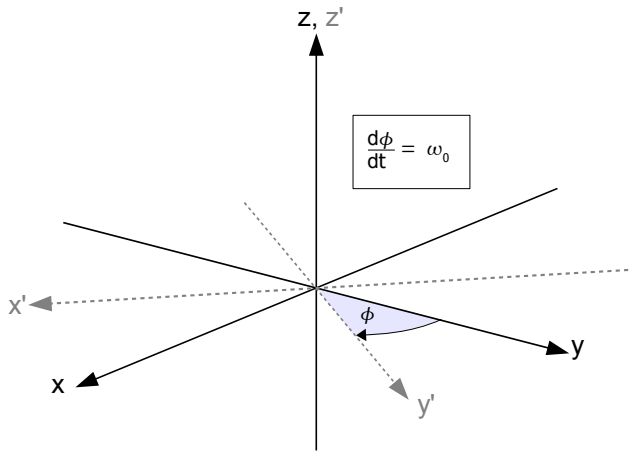

Figure 2.4: The laboratory reference frame (x-y-z) is static and the rotating reference frame (x'-y'-z') rotates with angular frequency ω_0. Both the z and z' axes are collinear with the $\vec{B_0}$ field. Frequencies expressed in the rotating frame are $\Omega = \omega - \omega_0$.

($\vec{B_1}$) perpendicular to $\vec{B_0}$. While it is turned on, this field causes precession about itself, rotating the $\vec{M}$ vector away from $\vec{B_0}$.

The most important characteristic of the radiofrequency (RF) pulse is that it must be matched to the Larmor frequency. This is, in fact, the origin of the term "magnetic resonance". As for direction of the $\vec{B_1}$ field, the most efficient rotation of $\vec{M}$ away from $\vec{B_0}$ will be when $\vec{B_1}$ is aligned perpendicular to the magnetization at all times. Because of the precession, this means that $\vec{B_1}$ is a circularly polarized field rotating at the Larmor frequency. To express this field, we define a reference frame rotating with angular frequency ω_0, the Larmor frequency (Fig. 2.4). To distinguish this frame from the laboratory frame (x-y-z axes), the rotating frame axes are primed (x'-y'-z'), and the z and z' axes are collinear along the B_0 field direction. Frequencies expressed in this rotating frame are given by

$$\Omega = \omega - \omega_0. \tag{2.28}$$

The net (or effective) magnetic field is the sum of the B_0 and B_1 fields in their respective reference frames.

$$\vec{B}_{\text{eff}} = B_0\,\hat{z} + \vec{B_1} \tag{2.29}$$

Hence, the equation of motion becomes

$$\frac{d\vec{M}}{dt} = \gamma\vec{M} \times (B_0\,\hat{z} + \vec{B_1}). \tag{2.30}$$

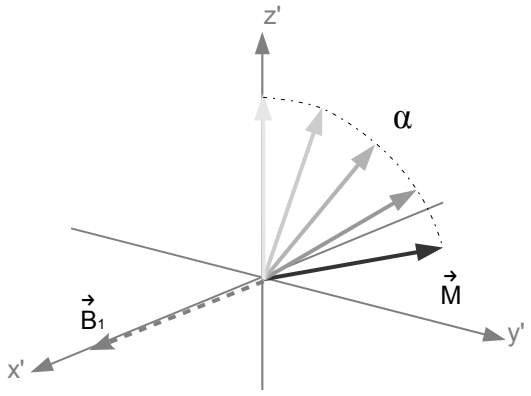

Figure 2.5: Effect of a circularly polarized pulse (B_1) on the magnetization ($\vec{M}$) in a reference frame rotating at the Larmor frequency (ω_L). The so-called flip angle, α is determined according to equation 2.34.

Expressing this equation in the rotating reference frame has the effect of canceling off the B_0 term, leaving only B_1. Also, there is some choice for the direction of $\vec{B_1}\ldots$ it is free to lie anywhere within the x'-y' plane. Arbitrarily selecting the $+x'$ direction, the previous equation becomes

$$\frac{d\vec{M}}{dt} = \gamma\vec{M} \times (B_1\,\hat{x'}). \tag{2.31}$$

The result is a rotation of $\vec{M}$ down towards the $+y'$ axis (see Fig. 2.5).

The angle α to which $\vec{M}$ rotates is called the "flip angle". It is determined by the strength of the RF field (B_1) and by the amount of time that B_1 is turned on (t). Experimentally, B_1 is referred to as the "pulse power" and t is referred to as the "pulse width".

$$\begin{aligned} \alpha &= \omega_1 t && (2.32)\\ &= \gamma B_1 t \ \ldots \text{ in radians, or} && (2.33)\\ &= \frac{180^\circ}{2\pi}\gamma B_1 t \ \ldots \text{ in degrees.} && (2.34) \end{aligned}$$

90° and 180° Pulses

An RF pulse may act to tip $\vec{M}$ to any arbitrary angle (equation 2.34), but 90° and 180° pulses are of special importance. An RF coil is mounted so that maximum

signal is detected when the magnetization is entirely in the transverse (xy) plane. This condition is satisfied when $\alpha = 90°$. In the quantum picture, the result of a 90° pulse is that the spins add to give zero net z component, meaning that they are equally distributed between the spin-up and spin-down states. In contrast, a 180° pulse flips the magnetization around completely onto the $-z$ axis, and results in no signal induced in the receiver (see Fig. 2.6). In the quantum picture, this corresponds to a complete reversal of the equilibrium populations in the spin-up and spin-down states.

The signal, which oscillates rapidly at the Larmor frequency, is picked up by a single receive coil, and a hardware processing step called "demodulation" is performed. This involves multiplication of the signal by a cosine and a sine function that are each oscillating at the Larmor frequency, which separates the signal into two components that (respectively) represent the x and y components of the precessing magnetization. Because the signal is oscillatory, and oscillations are often easiest to treat mathematically by using complex exponentials, the x and y components are often referred to as the real and imaginary parts, despite the fact that they are both equally real and observable signals. The demodulation step also has the effect of putting the signal in the rotating reference frame, wherein its apparent frequency is denoted by Ω. The distribution of frequencies is shifted so that the Larmor frequency becomes the origin, with lower frequencies being negative and higher frequencies being positive (see equation 2.28)

RF Phase

It was mentioned briefly that the direction of $\vec{B_1}$ in the rotating reference frame can be chosen arbitrarily within the x'-y' plane. The direction of the pulse determines the orientation of the magnetization in the transverse plane following an RF pulse, and as such, it is called the *phase* of the pulse.

To indicate the pulse phase, the axis of the $\vec{B_1}$ vector is added as a subscript to the the flip angle. Fig. 2.7 illustrates this with four separate RF pulses, each having the same magnitude, but different phase.

Switching the RF pulse phase can become important when multiple pulses are involved. Consider the simple example of two consecutive 90° pulses. If the phases

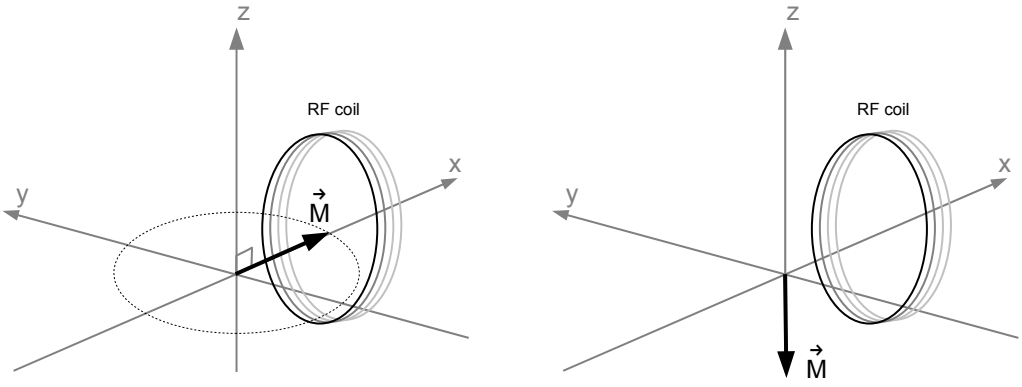

(a) 90° rotation

(b) 180° rotation

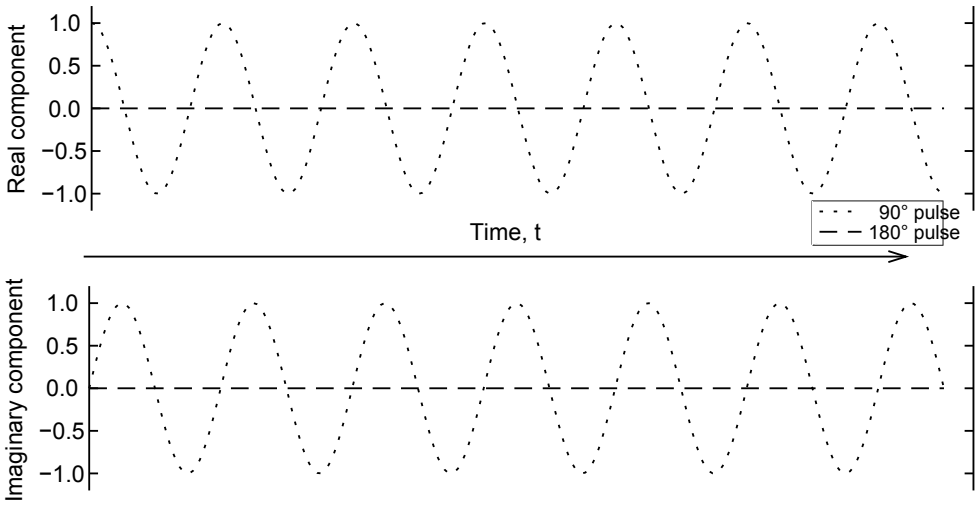

(c) Real and imaginary signal components

Figure 2.6: Magnetization after (a) a 90° pulse and (b) after a 180° pulse. (c) Real and imaginary signal after each pulse. A perfect 180° pulse does not produce any signal.

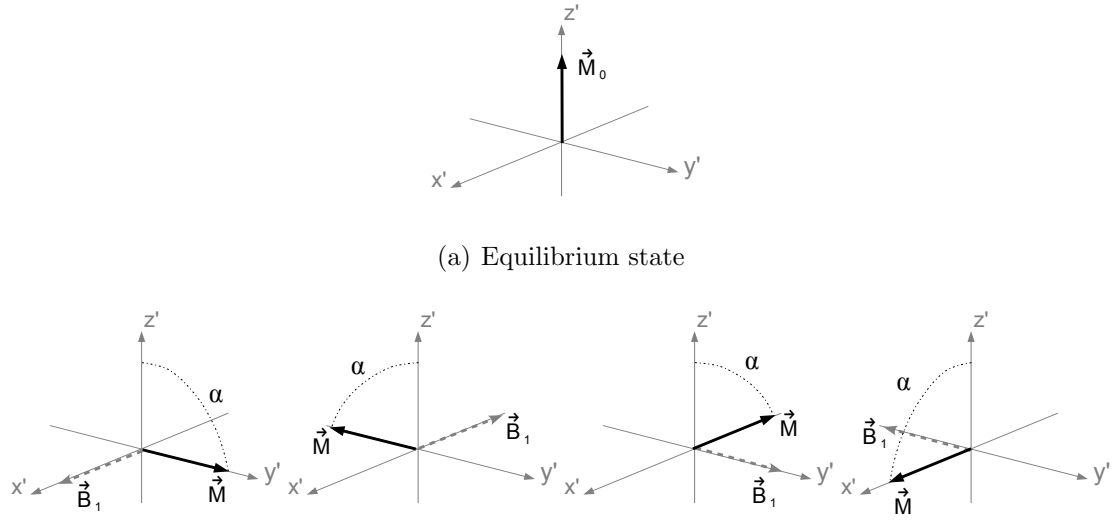

(a) Equilibrium state

(b) $\alpha = 90°_{x}$ (c) $\alpha = 90°_{-x}$ (d) $\alpha = 90°_{y}$ (e) $\alpha = 90°_{-y}$

Figure 2.7: The equilibrium magnetization and four RF pulses, each having different phase

are identical, $90°_{x}$ – $90°_{x}$, the net result is a 180° flip. On the other hand, if the phases are reversed, $90°_{x}$ – $90°_{-x}$, the magnetization returns back to the original $+z'$ direction.

Just as the phase of the RF pulse may be set, so can the RF receiver phase—a fact that can be used for selective addition or subtraction of signal. As an example, consider a single pulse followed by signal readout (via the receiver), as shown in Fig. 2.8. If the phase of the RF pulse is $90°_{x}$ and the receiver phase is the same, the signal readout will be the oscillating function shown in (a). If the same measurement is repeated with the receiver phase *inverted* (i.e. set to $90°_{-x}$ instead), then the detected signal will be negative, as shown in (b). If the sum of the two is computed, the signals null one another (c).

In NMR techniques, repeated experiments are often added together. This may be done to *enhance* signal and improve the signal-to-noise ratio (SNR), or it may be done to *subtract* unwanted signal to eliminate artifacts. These techniques rely on judicious selection of RF transmit/receive phase.

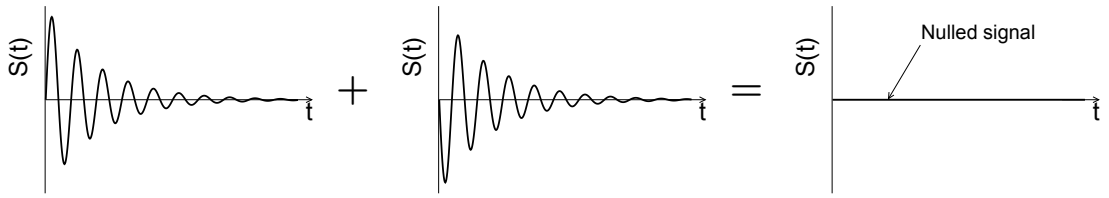

(a) $90°_{x}$ (b) $90°_{-x}$ (c)

Figure 2.8: The effects of alternating receiver phase: following a $90°_{x}$ RF pulse, signal detected with receiver phase (a) $90°_{x}$ and (b) $90°_{-x}$ are inverted, and therefore (c) null each other when added.

2.1.4 Physics of NMR Relaxation

The coherent precession of nuclei does not continue indefinitely, and stochastic processes eventually cause the signal to die away. Signal relaxation is at the heart of magnetic resonance imaging. MRI utilizes the fact that different materials may have different relaxation rates, which can be used to both characterize and create contrast in a system being imaged, even when the materials have very similar densities [22]. In this way, MRI is more versatile than x-ray computed tomography, in which contrast is based primarily on density variations.

While relaxation can be a powerful tool, it can also have undesired effects on images, and must be well-understood so that these effects may be compensated for when necessary. This is especially important to the MRI of solid materials, where the relaxation times tend to be much shorter than in liquids, and experimental imaging parameters which may have worked in a medical context must be modified.

T_1 Relaxation

When a material is placed in a magnetic field, the nuclear spins take some time to settle into equilibrium. From the initial, unpolarized condition, the Zeeman splitting between the spin-up and spin-down energy levels causes a gradual shift of the spin populations from the high energy level to the low one. This is an exponential process, with the rate of relaxation depending on the fraction of spins still remaining in the high energy state. Macroscopically, this is seen as the growth of the bulk magnetization vector along the z axis from $\vec{M} = 0\,\hat{z}$ to $\vec{M} = M_0\,\hat{z}$, as shown in Fig. 2.9.

Phenomenologically, this observation can be accounted by adding a term in the

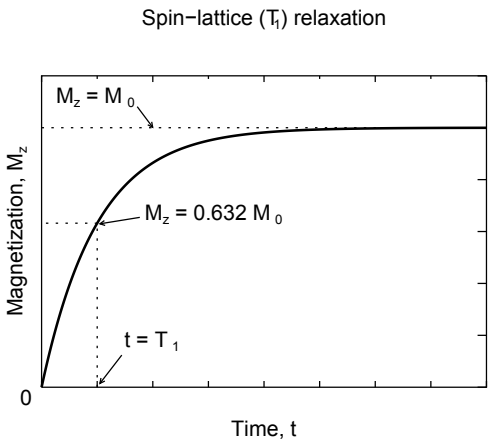

Figure 2.9: Spin-lattice relaxation: the longitudinal magnetization exponentially approaches the equilibrium magnetization ($M_z = M_0$) with a time constant T_1.

equation for the z magnetization (equation 2.26).

$$\frac{dM_z}{dt} = \frac{M_0 - M_z(t)}{T_1} \tag{2.35}$$

Here, T_1 is time constant that characterizes the rate of recovery, and is called the "spin-lattice" relaxation time. Integrating yields an expression for $M_z(t)$.

$$M_z(t) = M_0 - (M_0 - M_z(0))e^{-t/T_1} \tag{2.36}$$

In the special case where $M_z(0)$ starts from zero,

$$M_z(t) = M_0 \left(1 - e^{-t/T_1}\right). \tag{2.37}$$

This effect is called "spin-lattice relaxation", which comes from the interaction that causes the relaxation. Random thermal motions (translations, rotations, and vibrations) of atoms and molecules occur with a range of coherence times, and thus photons are emitted with a range of energies (frequencies). The distribution of frequencies is referred to as the *spectral density function*. Photons having frequency ω_0 (the Larmor frequency) are capable of stimulating spins to transition from the spin-down state to the spin-up state. Relaxation is thus due to an interaction between nuclear spins and molecules in the surrounding environment, or "lattice" (although this is not meant to imply any degree of order or crystallinity—T_1 relaxation occurs in gases, liquids, glasses, and crystals alike) [20, 22].

Though the dynamics which determine T_1 are complicated, they may be summarized by the general principle that a greater rate of photon exchange between the nuclei and the lattice will result in a shorter T_1 (i.e. faster relaxation). Because the spectral density function is dependent on temperature, molecular species, and anything else that affects the molecular motion, the T_1 relaxation time will vary depending on these parameters.

In addition to a dependence on the motional parameters of molecules in "the lattice", it was reported by Bloembergen, Purcell, and Pound [20] that T_1 is especially influenced by the presence of paramagnetic ions. The strong magnetic field about the unpaired electrons of these ionic species is very effective at stimulating spin transitions in nearby nuclei, and in certain cases they may be added as "doping" agents to a sample to artificially reduce the relaxation time.

T_2 relaxation

In addition to the longitudinal magnetization recovery, there is a second type of relaxation, which affects the *transverse* magnetization. In an ideally homogeneous magnetic field, the Larmor equation would suggest that every nuclear spin would precess at the exact same rate. The truth, however, is that surrounding each nucleus is a dipolar field that slightly perturbs the B_0 field about it. Nuclei in the locally-perturbed field will precess at rates that deviate slightly from ω_0, with the result that an ensemble of spins that are initially precessing coherently will gradually lose that coherence, and the magnetic moments that initially added constructively will ultimately cancel out over time.

This loss of coherence is called "spin-spin relaxation" because it is due to the field perturbations of nearby spins. Like T_1 relaxation, it is also an exponential process. Similarly, then, a phenomenological term may be added to the transverse component of the magnetization (equation 2.27) to account for the effect.

$$\frac{d\vec{M}_\perp}{dt} = \gamma \vec{M}_\perp \times (B_0\,\hat{z}) \;-\; \frac{\vec{M}_\perp}{T_2} \tag{2.38}$$

As the first term affects only the *direction* of $\vec{M}_\perp$, an integrated expression for the magnitude involves only the second term.

$$M_\perp = M_0\, e^{-t/T_2} \tag{2.39}$$

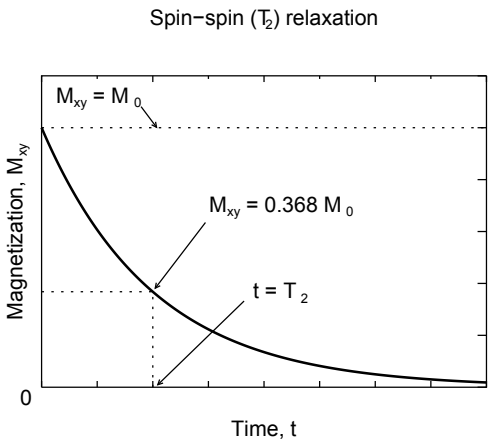

Figure 2.10: Spin-spin relaxation: the transverse magnetization decays exponentially with a time constant T_2 as spins dephase.

The decay of the transverse magnetization is represented in Fig. 2.10.

The mechanism governing T_2 is related to the dipolar field surrounding nuclei and the changes in that field as molecules tumble. Consider the two proton nuclei in a water molecule. If the molecule were tumbling slowly, the nuclei would each see a relatively slowly-changing field, albeit one perturbed by the presence of the other nucleus. The slower the molecule tumbles, the more constant the field that the other nucleus sees, and the more quickly their differing precessional rates cause them to lose phase coherence. In contrast, a very rapidly-tumbling molecule will encounter both positive and negative perturbations to the B_0 field. The time average of these perturbations, even over short times, will be zero, and the precessional rates of the two nuclei will be nearly equal on average. In this way dephasing will be less rapid than in an environment of slowly tumbling molecules [21] (see Fig. 2.11).

Because T_2 most commonly involves fields *within* a molecule and T_1 involves energy exchange between molecules within the (so-called) lattice, spin-spin relaxation can be thought of as an *intra*molecular interaction[†] and spin-lattice relaxation can be thought of as an *inter*molecular interaction. Incidentally, for nearly every material, the T_2 relaxation time is less than or equal to T_1.

[†]Exceptions include interactions within a crystal lattice, which may take place over much larger distances.

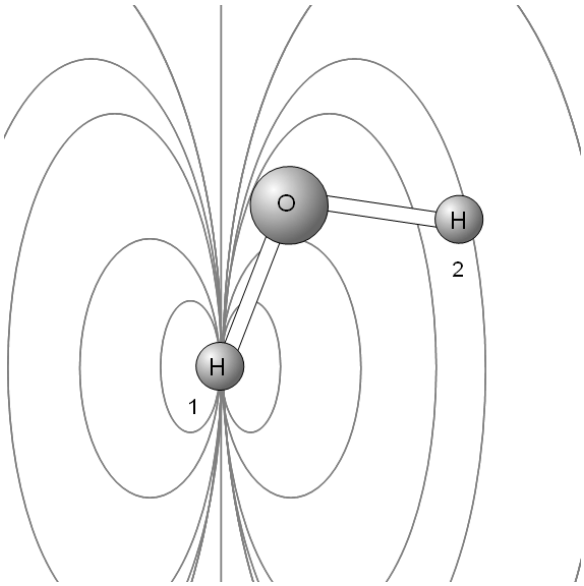

Figure 2.11: Mechanism of T_2 relaxation: hydrogen atom #2 is in the dipole field of atom #1. Fast tumbling will randomize the dipolar field the nucleus sees.

T_2^* Relaxation

In the discussion of T_2 it was assumed that the B_0 field was entirely homogeneous, but in reality this is never the case (although in modern magnets, every effort is taken to design the apparatus for the most homogeneous field, and the field profile is shimmed to correct for perturbations). Even if perfect hardware existed, however, a sample that is being imaged will *itself* distort the field around it through the effect of magnetic susceptibility. At the edges of the sample and at interfaces between different materials the transition between regions of different susceptibilities leads to distortion of the field. In addition to these *undesirable* field inhomogeneities, the whole of magnetic resonance imaging is built upon imposing *controlled* magnetic field gradients to spatially encode the Larmor precessional frequency (to be discussed in detail in a later section). This causes neighboring nuclei to experience different magnetic field strengths, and the rate of dephasing becomes greater.

In light of the effect of field inhomogeneities, the T_2 as discussed in the previous section is referred-to as the "intrinsic" T_2. With the added contributions to the field, the *effective* relaxation time is referred to as T_2^*, and is given by the following equation.

$$\frac{1}{T_2^*} = \frac{1}{T_2} + \frac{1}{T_2'} \tag{2.40}$$

Here, T_2' is a decay constant associated with only the static field inhomogeneities. Effective spin-spin relaxation has the same functional form as intrinsic spin-spin relaxation (equation 2.39), only with the substitution of T_2^* for T_2.

$$M_\perp = M_0 e^{-t/T_2^*} \tag{2.41}$$

Bloch Equations

At the beginning of the section, the general equation of motion was introduced (equation 2.22).

$$\frac{d\vec{M}}{dt} = \gamma \vec{M} \times \vec{B}_{\text{eff}}$$

By breaking $\vec{M}$ into longitudinal and transverse components and by including terms for the B_0 field, the B_1 (RF) field, and the spin-lattice and spin-spin interactions, this equation evolves into the following.

$$\frac{dM_z}{dt} = \gamma \vec{M}_z \times \vec{B}_1(t) + \frac{M_0 - M_z(t)}{T_1}\,\hat{z} \tag{2.42}$$

$$\frac{d\vec{M}_\perp}{dt} = \gamma \vec{M}_\perp \times (B_0\,\hat{z}) + \gamma \vec{M}_\perp \times \vec{B}_1(t) - \frac{\vec{M}_\perp}{T_2} \tag{2.43}$$

These equations are a general description of the NMR magnetization, and are called the Bloch equations.

2.2 Measuring Relaxation Times

The previous section introduced the underlying physics that govern NMR relaxation. The purpose of this section is to introduce the techniques that are used to measure the relaxation times, along with some experimental issues that must be considered with those measurements.

2.2.1 T_2^* — the FID

A measurement of T_2^* is the simplest one possible, and involves a 90° RF pulse to rotate the magnetization into the transverse plane, then detection of the signal in the probe. Because the signal is due to the simple, undisturbed response of the tipped magnetization, this type of experiment is called a "free-induction decay", or FID for short.

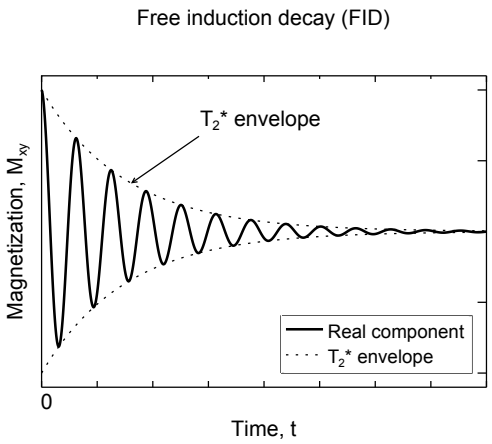

Figure 2.12: Effective spin-spin relaxation: transverse magnetization decays exponentially with a time constant T_2^* ($< T_2$). Here, only the real component is shown; the imaginary component has a phase difference of $\pi/2$.

During signal detection, the hardware performs a demodulation operation that yields real and imaginary components. In general, the functional form of these two components is a sinusoidal oscillation modulated by an exponential decay envelope, with the frequency of oscillation being Ω and the time constant for the decay being T_2^* (see Fig. 2.12).

2.2.2 T_2 — the Spin Echo

Recall that T_2^* arises from the combination of two types of interactions: 1) the interaction with the dipolar fields of nearby spins (with time constant T_2), and 2) the interaction with non-uniformities (offsets) in the main B_0 field (with time constant T_2'). The T_2 interaction is inherently random, owing to the thermal reorientation of molecules, and is thus completely stochastic and irreversible. The T_2' interaction is different, however, because the non-uniformities in the field are static, so their effects can be reversed using a technique called the "spin echo".

The invention of the basic spin echo technique is credited to Erwin Hahn. He realized that following a 90° RF pulse, the base precessional rate of a spin isochromat at position $\vec{r}$ is determined by the magnitude of the local magnetic field,

$$B(\vec{r}) = B_0 + \delta(\vec{r}), \tag{2.44}$$

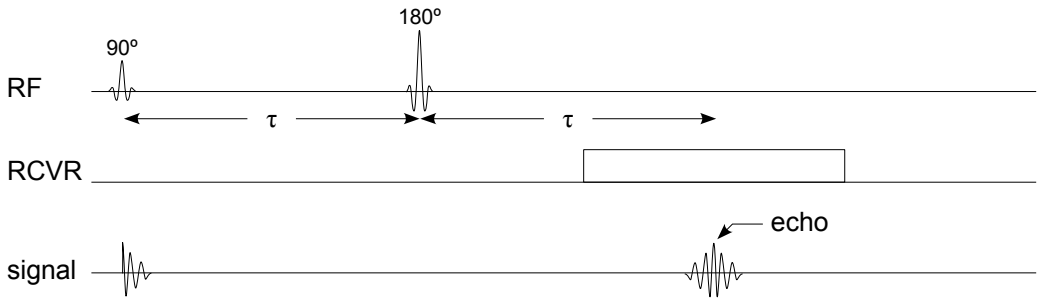

Figure 2.13: The spin echo sequence. A 180° pulse at time τ causes refocusing of the the magnetization (an echo) at TE $= 2\tau$.

where B is expressed as the sum of B_0 and the local field offset, $\delta(\vec{r})$. In a time τ, provided the field offset does not change and the spins are effectively static, the isochromat will accrue phase according to the strength of the field offset.

$$\phi(\vec{r}) = \tau\, \delta(\vec{r}) \tag{2.45}$$

A spin echo is created by inverting the phase using a 180° RF pulse at time τ. Following the pulse, the spins will continue to precess at the same rate as before, except in a sense that causes momentarily re-alignment at time 2τ. This realignment effectively nullifies the effect of the static field offsets, and the amplitude at that time is weighted by the intrinsic T_2 only. The time 2τ is called the echo time (TE).

The sequence diagram used for a spin echo measurement is shown in Fig. 2.13. A sequence diagram is a schematic representation of an NMR experiment, where the lines in the diagram represent the state of the transmitter (RF), the receiver (RCVR), and the signal itself (signal). Time advances along the horizontal direction. The effect of a spin echo on the spins is shown diagrammatically in Fig. 2.14.

Since the echo amplitude is not affected by field inhomogeneities, T_2 may be measured by generating spin echoes at various echo times (t = TE) and determining T_2 from the echo amplitudes, as expressed in the following equation.

$$M(\mathrm{TE}) = M_0 e^{-\mathrm{TE}/T_2} \tag{2.46}$$

A plot of the signal during a spin echo is illustrated in Fig. 2.15.

One of the assumptions in using a simple Hahn echo is that spins are not in motion. In reality, the spins actually undergo diffusive motion through the field

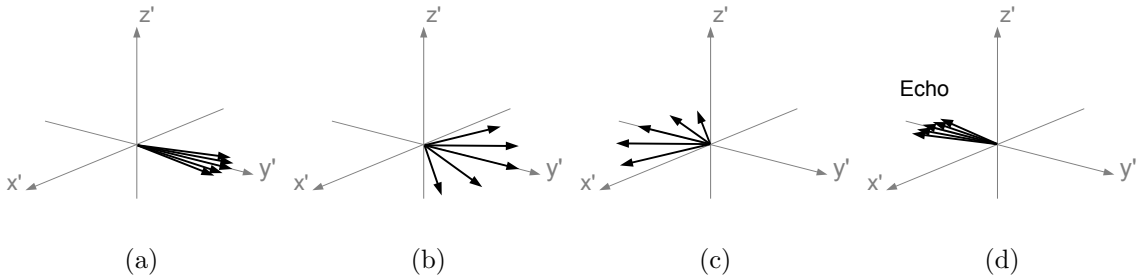

Figure 2.14: A spin echo shown in the rotating reference frame: (a) Spins are initially in phase. (b) B-field inhomogeneities cause dephasing. (c) At time τ, a $180°_{-x}$ pulse flips the spins about the x axis. (d) The spins refocus to form an echo at time, $\mathrm{TE} = 2\tau$.

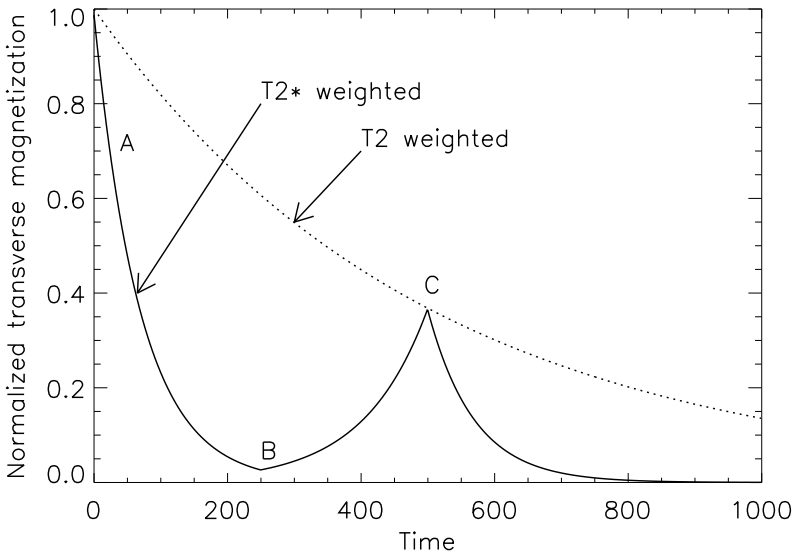

Figure 2.15: Transverse magnetization during a spin echo. (A) Signal originally decays according to T_2^*. (B) A 180° pulse causes rephasing. (C) An echo forms. Its magnitude is weighted by T_2 (dotted line).

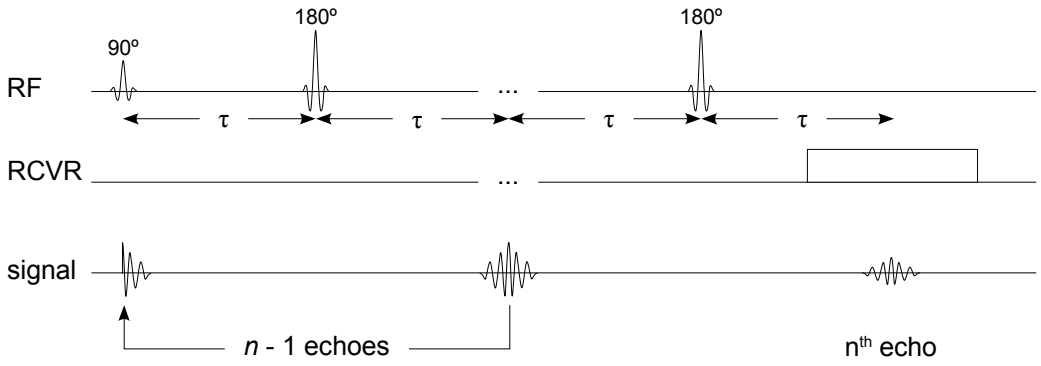

Figure 2.16: The CPMG sequence. A train of 180° pulses is used to create a series of echoes, each progressively weighted by T_2.

inhomogeneities. The effects of diffusion may be diminished by choosing a short τ, which reduces the distance traveled by a diffusing molecule and thus reduces the field variations that it "samples". This principle forms the basis of a method introduced by Carr and Purcell [64], which is to use a train of evenly-spaced 180° pulses to generate the series of spin echoes one after the other (see Fig. 2.16). The amplitude of the n^{th} echo is weighted by the "total" echo time (TE $= 2\,n\tau$)), and the series of peak amplitudes can be obtained in a single measurement (Fig. 2.17).

A further modification to the Carr-Purcell sequence was made by Meiboom and Gill [65]. This modification was developed to address the experimental problem of imperfect 180° pulses. That is, even with the best hardware and calibration, it is impossible to generate a perfect 180° flip *everywhere* within a sample. In a train of pulses, then, the resulting small errors accrue and result in a loss of transverse magnetization. By simply alternating the phase of the pulses ($+\hat{y}$, $-\hat{y}$ for example), the error in the flip angle is corrected in every second echo. This technique is thus called a CPMG echo train after Carr, Purcell, Meiboom, and Gill, and is the standard technique for measuring T_2. By using only the even or odd echoes in a CPMG train, one obtains a series of echoes free of error from imperfect 180° pulses.

2.2.3 T_1 — Inversion Recovery

The most common technique for measuring T_1 is called inversion recovery (IR). Since T_1 relaxation occurs in the longitudinal ($\hat{z}$) direction, the method involves perturbing

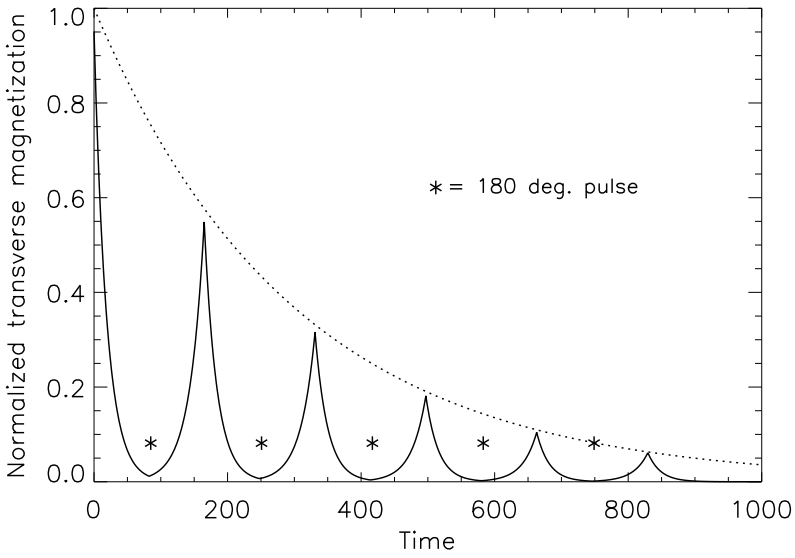

Figure 2.17: Repeated 180° pulses (occurring at the * symbols) will form a train of spin echoes from which T_2 can be determined. This is called a CPMG echo train.

the z magnetization and allowing it to return exponentially back to equilibrium. This is done using a 180° pulse to completely invert the magnetization, hence the term "inversion recovery". To measure the magnetization at any point in the recovery involves using a 90° pulse to rotate it into the transverse plane so that the magnetization can be detected. The IR pulse sequence is shown in Fig. 2.18 and the effect on the magnetization is illustrated in Fig. 2.19.

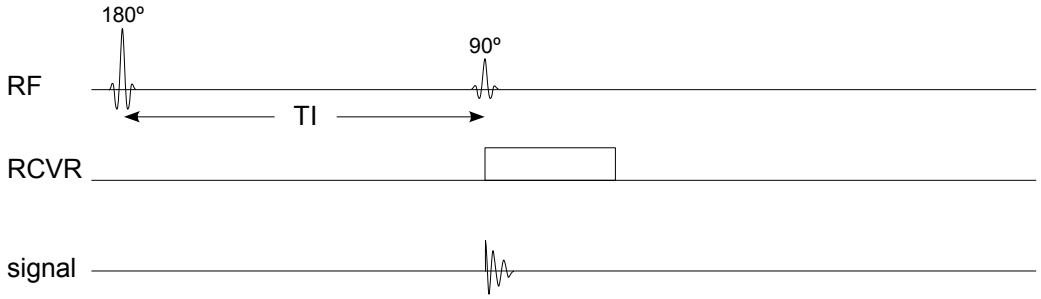

Figure 2.18: The IR sequence: A 180° pulse inverts the magnetization, which then recovers for time TI, at which point it is sampled using a 90° pulse.

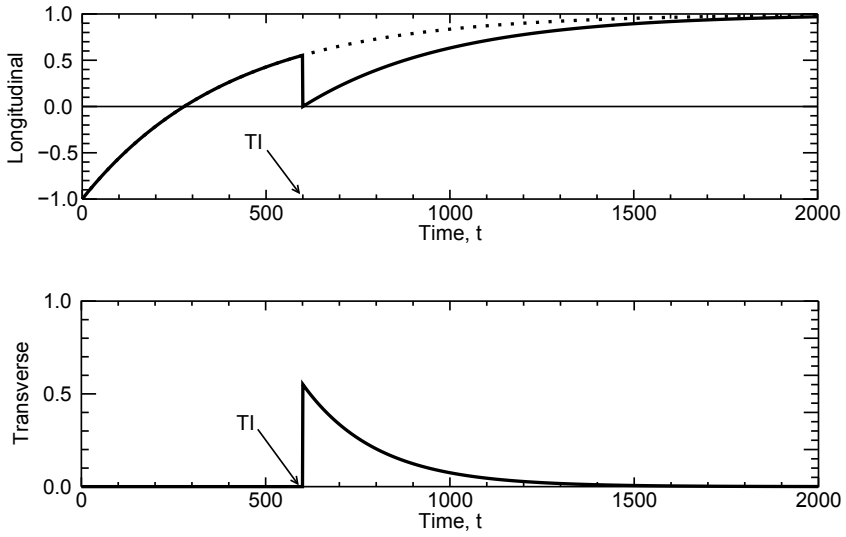

Figure 2.19: Inversion recovery: a 180° pulse inverts M_z, and at TI, a 90° pulse tips it into the transverse plane so it can be detected. The horizontal scale is time, and the vertical scales are normalized longitudinal magnetization (top graph) and normalized transverse magnetization (bottom graph).

The equation for the z magnetization in an IR experiment is

$$M_z(t) = M_0 - (M_0 - M(0))\, e^{-t/T_1}. \tag{2.47}$$

Here, M_0 is the equilibrium magnetization, and $M(0)$ is the magnetization immediately following the inversion pulse. For a perfect 180° pulse, $M(0)$ should equal M_0, and the equation should be

$$M_z(t) = M_0(1 - 2e^{-t/T_1}). \tag{2.48}$$

Because of the possibility for incomplete inversion, though, the preceding equation is more general.

In terms of signal magnitude immediately following the 90° pulse that tips the z magnetization into the transverse plane, it is

$$M(\mathrm{TI}) = M_0 - (M_0 - M(0))\, e^{-\mathrm{TI}/T_1}. \tag{2.49}$$

The T_1 relaxation time can be obtained by repeating the inversion recovery experiment for several TI.

Because T_1 dictates how rapidly the magnetization returns to equilibrium, it is an important consideration when designing any NMR experiment. Care must be taken in selecting the "repetition time" (TR), which is the delay between subsequent NMR acquisitions, because a TR that is too short can lead to an attenuation of the amount of signal available in consecutive measurements. The effects on the signal are referred to as "saturation effects", and they can be prevented by choosing a sufficiently long TR (see Fig. 2.20). As a general rule, this usually means a TR equal to $5 - 6 \times T_1$, corresponding to 98.6% – 99.5% recovery, respectively.

2.2.4 Multi-Component Relaxation and Chemical Exchange

So far in the discussion of relaxation times, the focus has been only on simple, homogeneous systems, such as pure liquids. In more complicated systems, however, there may be distinct states or "microenvironments", which are defined by local differences in either the precessional frequency (ω) or in the relaxation times. In systems such as these, the observed relaxation behaviour becomes a product not only of the conditions within each state/microenvironment, but also of exchange between them.

The effect of chemical exchange on relaxation times can be fairly complex, particularly when there exist multiple states/microenvironments within the sample. The simplest situation is exchange between only two sites, but more complicated situations can be built up from consideration of pairs of exchanging environments.

The mathematics for NMR in the presence of chemical exchange are referred to as the "two-site exchange equations" (TSEE) [66–68]. The essential components to the TSEE theory are as follows. Firstly, there are 2 states having different relaxation times. All the spins together in a given state are referred to as "pools". Each pool has a characteristic relaxation time, which represents the "true" relaxation rate of the spins while they are in that pool. The theory applies to both spin-spin and spin-lattice relaxation, so the symbol T will be used here to represent a general relaxation time. By convention, the pools are assigned the label "a" or "b", with pool "a" arbitrarily being the one having the greater relaxation time: $T_a > T_b$. In addition to their respective relaxation times, each pool is defined by the fraction of spins contained at equilibrium. This is expressed as normalized probabilities, P_a and P_b.

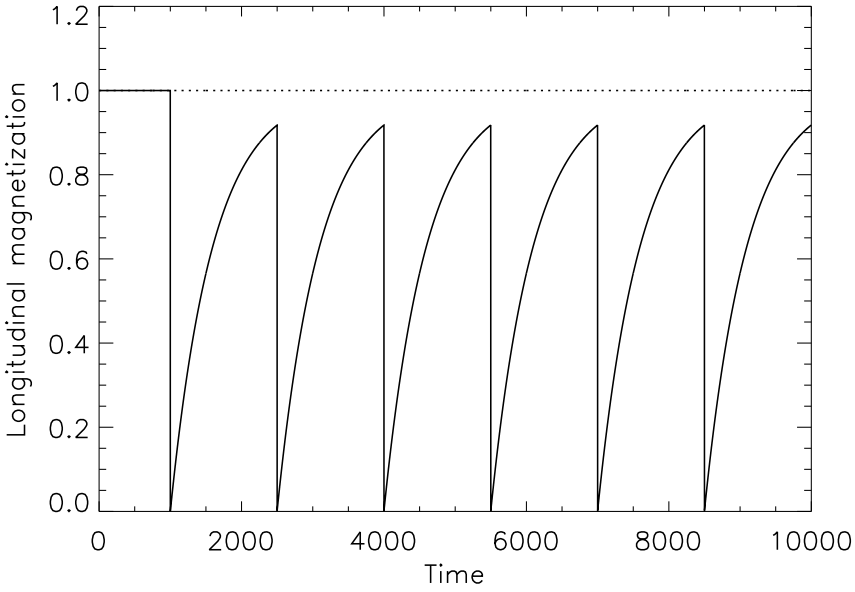

(a)

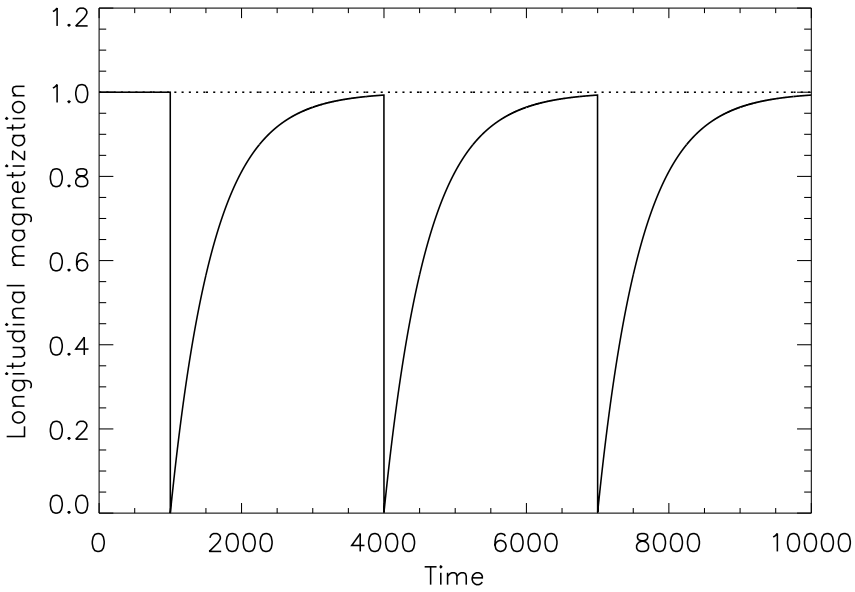

(b)

Figure 2.20: Saturation effects: (a) a short TR limits the magnetization available for all 90° pulses after the initial one. (b) This is corrected by lengthening the TR to approximately $5 - 6 \times T_1$.

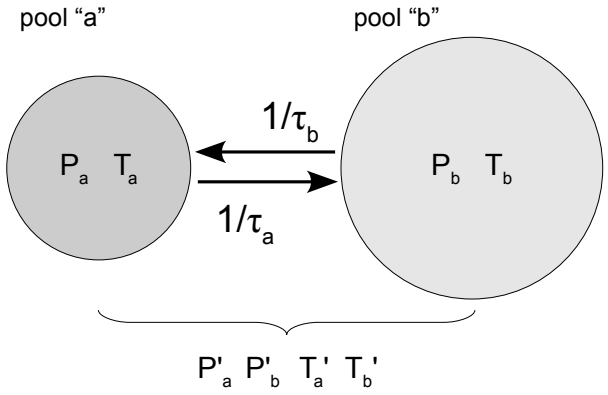

Figure 2.21: Schematic of two-site exchange. The “true” parameters are intrinsic, physical characteristics of the system. The measured quantities (primed) are a function of the rates of spin exchange between pool a and pool b.

The purpose of the exchange equations is to describe how the *measured* characteristics of the system arise from the *true* relaxation times and spin fractions in the presence of exchange. Exchange is quantified by the residence times of spins in each environment, τ_a and τ_b, which are the average times spent in the respective environment before “hopping” to the other. The overall exchange rate, $1/\tau$, is defined as the sum of the two rates.

$$\frac{1}{\tau} = \frac{1}{\tau_a} + \frac{1}{\tau_b} \tag{2.50}$$

Furthermore, in equilibrium, there must be flux balance:

$$\frac{\tau_a}{\tau_b} = \frac{P_a}{P_b} \tag{2.51}$$

A prime is used to denote the measured equivalent of each of the “true” quantities in the system (e.g. $P_a \rightarrow P'_a$). Fig. 2.21 illustrates two-site exchange schematically.

While the reader is referred to Herbst and Goldstein [69] for a complete derivation, the final expressions for the relaxation-based TSEE are as follows:

$$P'_a + P'_b = 1 \tag{2.52}$$

$$P'_b = \frac{1}{2} - \frac{1}{4}\left[(P_b - P_a)\left(\frac{1}{T_a} - \frac{1}{T_b}\right) + \frac{1}{\tau_a} + \frac{1}{\tau_b}\right]/c_2 \tag{2.53}$$

$$\frac{1}{T'_a} = (c_1 - c_2) \tag{2.54}$$

$$\frac{1}{T'_b} = (c_1 + c_2) \tag{2.55}$$

$$\tag{2.56}$$

where the constants c_1 and c_2 are

$$c_1 = \frac{1}{2}\left(\frac{1}{T_a} + \frac{1}{\tau_a} + \frac{1}{T_b} + \frac{1}{\tau_b}\right) \tag{2.57}$$

$$c_2 = \frac{1}{2}\sqrt{\left(\frac{1}{T_b} - \frac{1}{T_a} + \frac{1}{\tau_b} - \frac{1}{\tau_a}\right)^2 + \frac{4}{\tau_a\tau_b}} \tag{2.58}$$

Qualitatively, here are the implications of the TSEE. Firstly, the observed relaxation behaviour is actually the sum of two components, each having its own apparent relaxation time (T_a' and T_b') and probability (P_a' and P_b'). The general result is that the previous relaxation equations take on a "biexponential" form. For T_1, equation 2.36 becomes

$$M_z(t) = M_0 - \left(M_0 - M_a e^{-t/T_{1a}'} - M_b e^{-t/T_{1b}'}\right), \tag{2.59}$$

and for T_2, equation 2.39 becomes

$$M_{xy}(t) = M_a e^{-t/T_{2a}'} - M_b e^{-t/T_{2b}'}. \tag{2.60}$$

Fig. 2.22 shows an example of what biexponential T_2 relaxation looks like. In a measured data set, the probabilities correspond to the measured signal amplitudes, and the relaxation times and amplitudes are affected by the exchange correlation times, τ_a and τ_b, which can greatly alter the characteristics of the signal. Example calculations are shown in appendix A to demonstrate the effects of exchange on a model system.

The effect of exchange depends on the exchange correlation times relative to the relaxation times. These relations are frequently expressed in terms of the *rates* of exchange ($1/\tau$) and of relaxation ($1/T$). The extreme of $1/\tau \ll 1/T_a$ is called "slow exchange" and the extreme of $1/\tau \gg 1/T_b$ is called "fast exchange". Between the two extremes is the regime of "intermediate exchange". The characteristics of the different regimes are as follows:

Slow exchange: In the regime of very slow exchange, the components behave as if they are effectively non-exchanging, with the result that the $T_{a/b}$ and $P_{a/b}$ approximate the true values closely.

Intermediate exchange: In this regime, the measured parameters are a mixture of the true components. The relaxation times are lower than the true ones, and the probabilities no longer correctly indicate the fraction of spins in each pool.

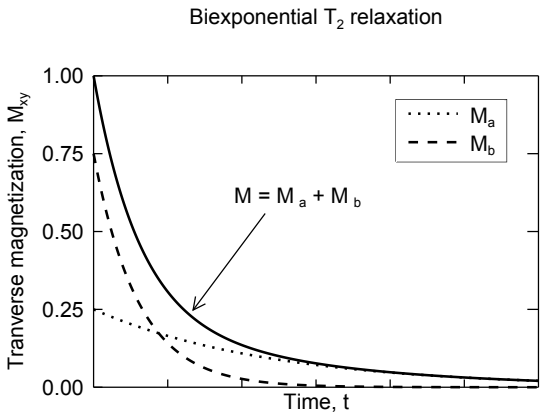

Figure 2.22: Biexponential relaxation of transverse magnetization. Signal M is the sum of two monoexponential functions, M_a and M_b. Although transverse relaxation is shown in this example, the same effect can be observed with longitudinal relaxation as well.

Fast exchange: When exchange is very rapid, spins "hop" between the two environments repeatedly over the relaxation timescale. Although technically still biexponential, the amplitude of one component approaches zero, and the result is an *apparently* single-exponential relaxation curve. The probability/amplitude of the remaining signal becomes the sum $P_a + P_b$ and the relaxation time becomes a weighted average of the two components.

In general, T_2 tends to be shorter than T_1, and in some systems the difference between these two parameters is large. Added to the fact that the relaxation timescale influences the exchange regime, this means that a T_2 measurement can potentially resolve multiple components in exchange better than T_1.

While the TSEE are useful for understanding qualitatively how exchange affects relaxation, in general it is the true (unprimed) quantities that are not known. In this case, there are ways to use the TSEE to obtain them. One major caveat, however, is that there are 3 equations and 4 unknowns, and the techniques for inverting the TSEE generally require more than just one measurement, as well as careful control over experimental conditions.

2.3 Imaging and k-Space

The Larmor equation says that spins in a uniform magnetic field of strength B_0 will precess with frequency $\omega_0 = \gamma B_0$. Because of this, imaging is made possible by using a spatially-varying field to effectively "label" points in space via the Larmor frequency. To understand how this is done, begin by considering the complex, demodulated signal from an infinitesimal volume d^3r at point $\vec{r}$ in some sample [19].

$$ds(t) = d^3r\, \rho(\vec{r})\, e^{i(\Omega t + \phi(\vec{r},t))} \tag{2.61}$$

Here, Ω is the demodulation frequency, which in the case of no offset is ω_0. The phase accumulated from Larmor precession is $\phi(\vec{r}, t)$. By imposing a linear gradient,

$$G = G_z = \frac{\partial B}{\partial z}, \tag{2.62}$$

the magnetic field strength becomes a function of position,

$$B(z) = B_0 + Gz \tag{2.63}$$

and the Larmor frequency is made to vary spatially.

$$\omega(z) = \omega_0 + \gamma G z \tag{2.64}$$

The accumulated phase due to precession, ϕ, then becomes

$$\phi = -\int_0^{t'} dt' \, (\omega_0 + \gamma G z) \tag{2.65}$$

$$\phi = -\omega_0 t - \int_0^{t'} dt' \, \gamma G z \tag{2.66}$$

Here, use has been made of the negative directional convention of the Larmor equation. Replacing this expression in equation 2.61, the argument of the exponential becomes

$$\Omega t - \omega_0 t - \gamma z \int_0^{t'} dt' \, G(t'), \tag{2.67}$$

which, because $\Omega = \omega_0$, becomes

$$-\gamma z \int_0^{t'} dt' \, G(t') \equiv \Phi \tag{2.68}$$

For the full, three-dimensional sample, it suffices to integrate equation 2.61 over all areas of non-zero spin density. In the case where imaging is done only in a single dimension, the problem may be simplified by integrating $\rho(\vec{r})$ over x and y.

$$\rho(z) = \iint dx\, dy\, \rho(\vec{r}) \tag{2.69}$$

The signal from the whole sample is thus

$$s(t) = \int dz\, \rho(z) e^{\Phi(z,t)}. \tag{2.70}$$

Inspired by the mathematics of crystal diffraction theory, the following variable substitution is made.

$$k = \frac{\gamma}{2\pi} \int_0^t dt'\, G(t') \tag{2.71}$$

In terms of this new variable, k (called the "spatial frequency"), the signal becomes

$$s(k) = \int dz\, \rho(z) e^{-i2\pi kz}. \tag{2.72}$$

This is an exciting result, because it says that the MRI signal and the proton spin density are Fourier inverses of one another. The inverse can then easily be written down as the Fourier transform of the signal

$$\rho(z) = \int dk\, s(k)\, e^{+i2\pi kz} \tag{2.73}$$

The introduction of the variable k gives a very useful way of thinking about imaging sequences. Sampling a signal can be thought of as sampling an abstract "space", aptly-called k-space, where position within the space is determined by gradient strength and time (see equation 2.71). It is often the case that the gradients are constant in time, so that

$$k = \frac{\gamma}{2\pi} G\, t. \tag{2.74}$$

A simple example will help to illustrate this concept of k-space. It will also introduce field gradients as an element of sequence diagrams. Fig. 2.23 shows a simple gradient imaging sequence, which is essentially an FID measurement, but with the addition of a field gradient during the signal digitization period.

$$G_z = \frac{\partial B(\vec{r})}{\partial z} \tag{2.75}$$

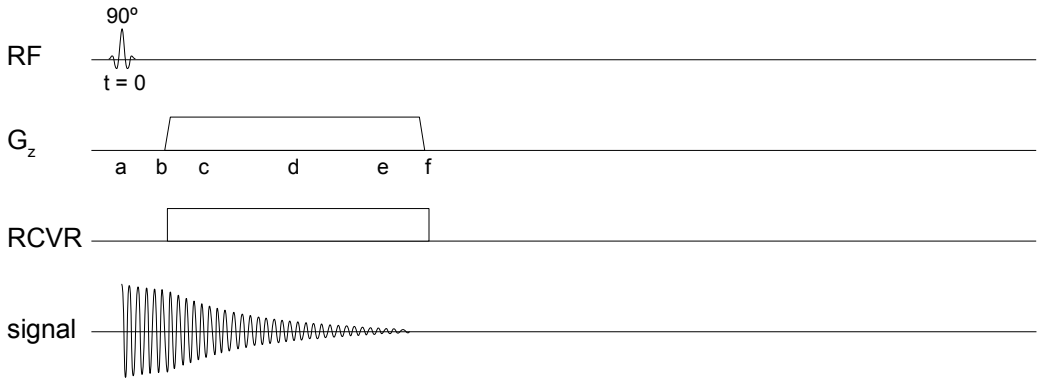

(a) Gradient imaging

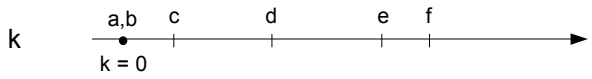

(b) k-space

Figure 2.23: Gradient imaging and k-space. Only positive values of k are sampled. The points a – f in the sequence correspond to positions a – f in the k-space trajectory. While other pulse sequences shown in this chapter show the signal in iconic form, a more realistic signal profile is presented here to illustrate the enhanced signal decay due to the gradient.

Here the subscript z indicates that the gradient is along the z direction (chosen arbitrarily for this example).

Time $t = 0$ begins at the onset of the 90° RF pulse. At this moment no time has passed, so the corresponding k-space position is 0. From a to b, again, there is no k-space motion, as the gradient is zero. From b through points c, d, and e, the k-space position is increasing linearly with time due to the constant gradient. At f, when the gradient turns off, the k-space position remains stationary once more. Following acquisition, a Fourier transform of the k-space signal will yield a one-dimensional image (or "profile") of the sample.

2.3.1 Image Resolution

The manner in which k-space is sampled ultimately determines the resolution in MRI. Assuming the signal is digitally sampled with a dwell time Δt, k-space is therefore sampled in intervals of $\Delta k = \gamma G \Delta t$. From the Fourier theory, this corresponds to the image having a field of view (FOV) of

$$\text{FOV} = \frac{1}{\Delta k} = \frac{1}{\gamma G \Delta t} \tag{2.76}$$

If N evenly-spaced points are acquired in total,

$$\Delta x = \frac{\text{FOV}}{N} = \frac{1}{N \gamma G \Delta t}. \tag{2.77}$$

2.3.2 Spin Echo Imaging

An improvement on the basic gradient imaging sequence in Fig. 2.23 is the spin echo imaging sequence (Fig. 2.24). The incorporation of a 180° pulse produces a spin echo, which refocuses signal attenuated by field inhomogeneities. The result is greater signal strength, and it will also prevent signal dropout artifacts from regions near susceptibility mismatches. Further still, the fact that the spin echo signal is weighted by T_2 means that this sequence helps to eliminate undesired relaxation weighting that can occur in materials with short T_2^*. This concept will be discussed further in section 2.27.

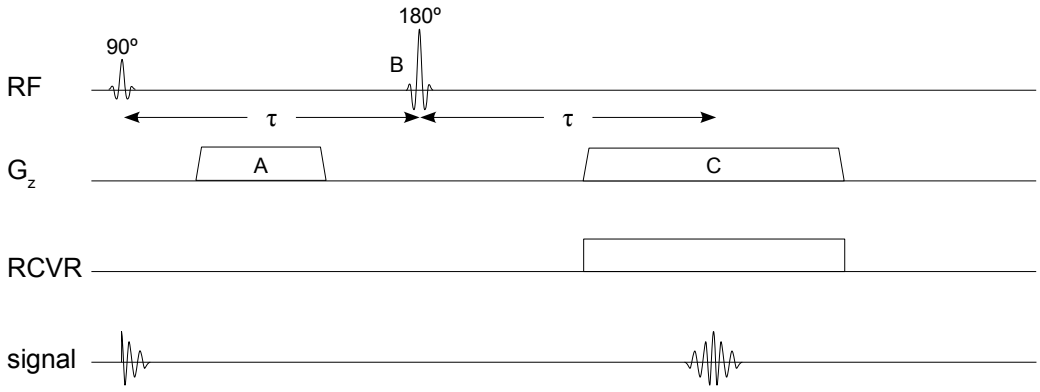

(a) Spin echo imaging

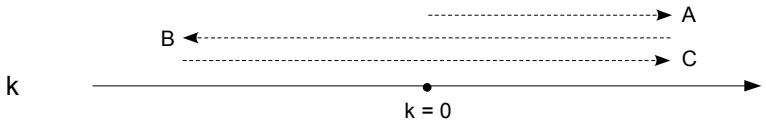

(b) k-space

Figure 2.24: Spin echo imaging. The sequence uses a positive gradient (A) to cover positive k-space values, then a 180° pulse (B) flips the k-space position about the origin. Another positive gradient (C) is used to acquire the image data. The spin echo occurs at $t = \mathrm{TE} = 2\tau$.

2.4 Pulsed Field Gradients and Diffusion

In a manner of speaking, field gradients in NMR serve to "label" positions in space according to the local Larmor frequency. This labeling is not solely restricted to times when the gradients are on; once they are turned off, it persists in the form of the phase accumulated by the spins. This fact leads to an inherent sensitivity to molecular diffusion in experiments involving field gradients. The Brownian motion that causes spins to move randomly from their starting position will result in a mixing of phase from those spins, which then enhances the apparent rate of relaxation.

Diffusion can be used as a form of contrast in MRI experiments. It is an important physical parameter in many systems, and knowledge of diffusion coefficients can be used to diagnose certain types of disease, understand chemical reaction rates, and parameterize transport in materials.

This section will briefly describe the physics of diffusion, how it affects the NMR signal, and how diffusion contrast is created in NMR experiments.

2.4.1 Diffusion Physics: the Random Walk

The physics of diffusion were described by Einstein using a single-atom model that yields a time-dependent probability distribution for the position of the atom. What follows is a concise overview of how the model works.

Consider a series of points lying along a z axis, each separated by a distance ζ. A particle begins at position $z = 0$ and, every τ_d seconds, hops a distance of ζa_i, where a_i is randomly either +1 or -1. The atom will therefore jump randomly back and forth between points on the z axis. After some time $t = j\tau_d$, the atom will be found at position

$$z = \zeta \sum_{i=1}^{j} a_i. \tag{2.78}$$

Through further derivation one can determine $f(z,t)$, the discrete probability distribution function of $z(t)$. By then taking the limit as ζ and τ_d become very small, the description becomes continuous rather than a discrete. Comparing with the diffusion equation,

$$D\nabla^2 f = \frac{\partial f}{\partial t}, \tag{2.79}$$

one obtains an expression for the diffusion coefficient,

$$D = \frac{\zeta^2}{2\tau_d}. \tag{2.80}$$

This constant has units of cm^2/s, and represents the rate at which molecules in a fluid are displaced from their initial position via random Brownian motion. In the absence of a molecular concentration gradient, it is called the *self-diffusion coefficient*, D^*. For many common fluids (including water), this is a well-defined function of temperature.

When a fluid is contained within biological tissue or absorbed within a material, the influence of a confining local microstructure may lead to a reduced effective rate of diffusion over a given time scale. The effective transport is referred to as the *diffusivity*, and a measured value of D^* is called the *apparent* diffusion coefficient (ADC). More generally, diffusivity can include additional effects, such as turbulence, but in the present context the terms "diffusivity" and "ADC" are used interchangeably. A measurement of the the ADC is valuable because it can provide insight into structural characteristics and fluid transport at the local scale.

2.4.2 Diffusion Effects and the NMR Signal

The effect of diffusion on the NMR signal was first observed in early spin echo measurements of T_2. While the relaxation of *viscous* liquids followed the expected form of a decaying exponential,

$$M_\perp \propto e^{-t/T_2}, \tag{2.81}$$

non-viscous liquids exhibited a t^3 dependence instead.

$$M_\perp \propto e^{-Ct^3} \tag{2.82}$$

Here, C is simply a constant. It was shown that this kind of behaviour is consistent with diffusion through a magnetic field gradient. The problem with the spin echo measurement was later solved by using a train of 180° pulses instead of single echoes. By treating the spin phases with consideration for the statistics of diffusion, the amplitude of the n^{th} spin echo is

$$M_\perp(t) = M_0 \exp\left(\left(\frac{-t}{T_2}\right) + \left(-\frac{\gamma^2 G^2 D t^3}{12n^2}\right)\right). \tag{2.83}$$

In this equation, G is the field gradient and n is the echo number. The equation contains the additional t^3 dependence that was previously observed, and it also shows that the diffusion contribution becomes weaker as n is increased for a fixed time period (i.e. the echo time is made smaller). By using a series of echoes that are closely-spaced, it is possible to attenuate the effects of diffusion on the signal, leaving only the T_2 relaxation component. It is the elimination of diffusion effects that is the primary motivation for using a Carr-Purcell echo train (later called the CPMG method).

2.4.3 Measurement of the Diffusion Coefficient

Pulsed Gradient Spin Echo (PGSE)

While diffusion effects are undesirable in a T_2 measurement, the presence of the effect means that NMR can be used as a tool for measurement of diffusion coefficients. The method for doing so is called the pulsed-gradient spin echo (PGSE) [70], and is shown in Fig. 2.25. In overview, the pulse sequence is based around a 180° pulse that generates a spin echo. Positioned about the 180° pulse are two strong, short-duration field gradients that introduce the diffusion encoding. The first gradient pulse dephases the spins, while the other refocuses them. The two gradient pulses have the same polarity because of the 180° pulse. The gradient reversal is complete only for spins that have remained stationary in the intervening delay. For spins that have moved, the rephasing is incomplete, and the resulting signal attenuation is a function of random molecular displacements (i.e. diffusion).

The expression for the the signal strength at the echo in the PGSE sequence is the following.

$$M_\perp = M_0\, e^{-D\gamma^2 g^2 \delta^2 (\Delta - \delta/3)} \tag{2.84}$$

In this equation, the values δ and g represent the duration and the amplitude of the gradient pulse, respectively. The value Δ is called the diffusion time, and is the time allowed for spins to diffusively mix. Finally, D is (nominally) the self diffusion coefficient, although for a fluid contained in a material, it is actually the *apparent* diffusion coefficient, because of the influence on physical boundaries within the material.

Examination of equation 2.84 reveals three quantities that can be varied to introduce diffusion weighting (δ, Δ, and g). The most common approach is to hold δ and

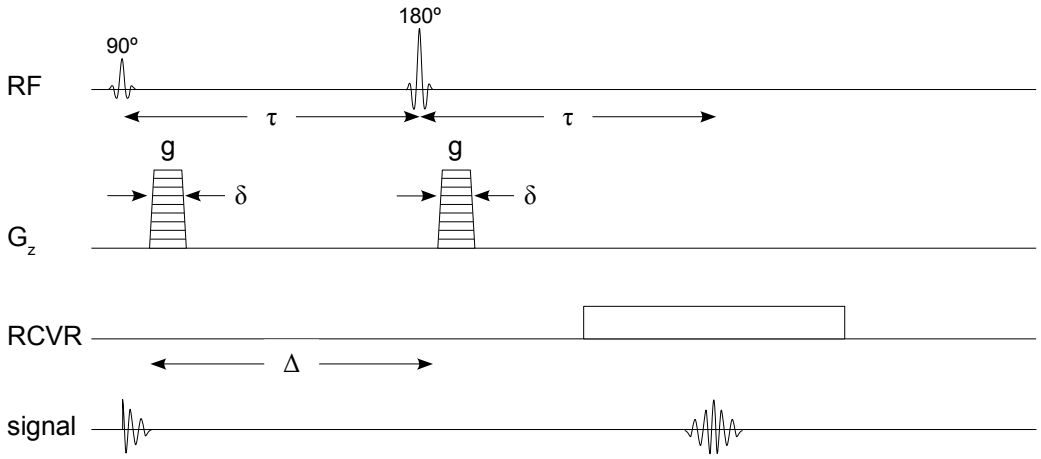

Figure 2.25: The pulsed-gradient spin echo (PGSE) sequence. A pair of pulsed field gradients of duration δ and separation Δ create the diffusion encoding. To prevent relaxation weighting, the δ and Δ delays are held constant, and the gradient amplitude, g, is varied.

Δ constant while g is varied. The advantage to this approach is that, by keeping the time constant, no explicit dependence on the T_1 or T_2 relaxation times is introduced. A practical rule-of-thumb for selecting the dynamic range of this type of experiment is that the δ and Δ parameters should be chosen so that the signal amplitude at $g = 0.95\, g_{\max}$ is 5% of the signal at $g = 0.05\, g_{\max}$ [71].

Stimulated Echo Variant (PGSTE)

While the PGSE sequence eliminates *errors* in the diffusion measurement caused by relaxation, the signal amplitude from this spin echo based technique is ultimately weighted by T_2. As such, in systems with short T_2, the signal may drop below the noise before the diffusion weighting is sufficient to make a measurement. When T_1 relaxation is much longer than T_2, another technique can be used for "storing" magnetization on the z axis, resulting in a pulse sequence that is weighted by T_1 rather than by T_2. This sequence is called the pulsed-gradient stimulated echo, and is shown in Fig. 2.26.

The PGSTE sequence is nearly the same as the PGSE sequence, except that the 180° pulse is replaced by a pair of 90° pulses instead. The first of these has the effect

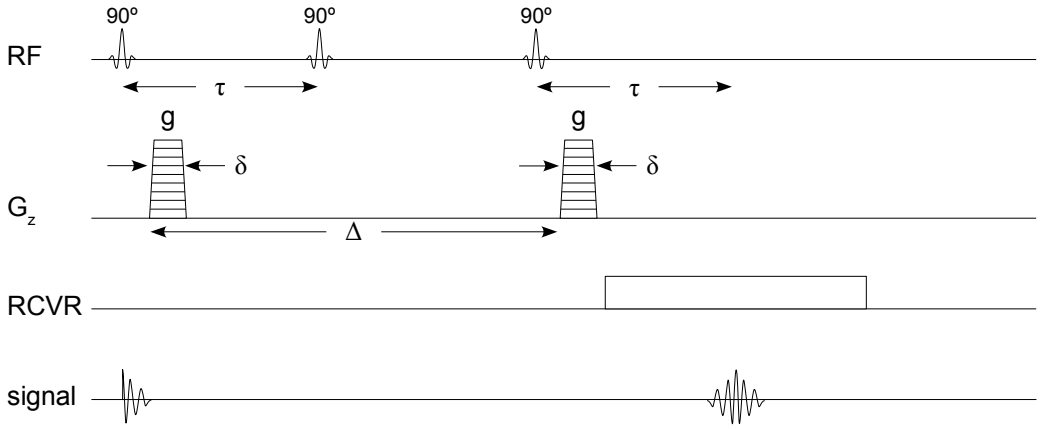

Figure 2.26: The pulsed-gradient stimulated echo (PGSTE) sequence. A variant on the PGSE sequence in which the 180° pulse is replaced by a pair of 90° pulses. By z-storing the magnetization, relaxation weighting comes from T_1, which can afford improved signal strength in materials having short T_2.

of rotating the magnetization onto the z axis, where the magnetization continues to relax at a rate governed by T_1. At a later time, the third 90° pulse is used to bring the magnetization back to the transverse plane. At time τ after the third pulse, the signal gets refocused in what is referred to as a *stimulated echo* (STE). The effective echo time is 2τ, just like a spin echo, but the weighting of the signal amplitude is a combination of T_1 and T_2.

One caveat when using PGSTE is that 50% of the signal amplitude is lost by the 90° storage pulse. This occurs because of dephasing leading up to the pulse, and the fact that transverse magnetization loses coherence in the (typically long) Δ delay. As a result, the 50% "overhead" signal loss of the PGSTE sequence must be weighed against the advantage of using the T_1-based z-storage step. On this topic, it should also be mentioned that a crusher gradient is sometimes applied during the Δ delay to ensure complete destruction of the residual transverse magnetiztion (thus preventing spurious signal from interfering with the measurement).

Anisotropy and Exchange

NMR diffusion measurements are special because the directionality of the pulsed gradient, $\vec{g}$, limits the motion sensitivity to only one axis at a time. In certain systems, however, anisotropy in the physical/chemical microstructure imposes a preferred direction for diffusion. This occurrence is fairly common in biological tissue, such as capillaries in plant tissues [21] and white matter fibers in the brain [72]. Where there is anisotropic diffusion, it is possible to conduct NMR diffusion measurements in multiple directions ($\hat{x}$, $\hat{y}$, and $\hat{z}$, for example) to characterize the anisotropy.

One final point regarding diffusion measurements is that it is subject to the same kind of exchange effects as the T_1 and T_2 relaxation times. In systems that contain multiple environments that restrict molecular translation differently, the diffusion signal may be multi-exponential as well. For the case of biexponential diffusion, there are two apparent diffusion coefficient, D_a and D_b, and the signal equation becomes the following.

$$M(g) = M_a e^{-D_a \gamma^2 g^2 \delta^2 (\Delta - \delta/3)} + M_b e^{-D_b \gamma^2 g^2 \delta^2 (\Delta - \delta/3)} \tag{2.85}$$

2.5 Mapping of Spin Density, Relaxation Times, and Diffusion

The effects of relaxation and diffusion must be understood to make accurate MRI measurements, but they can also be exploited to probe microstructural characteristics in a sample being imaged. In previous sections, the fundamentals of relaxation and diffusion, as well as imaging, were introduced. In this section, these concepts are combined to present techniques for creating maps of an NMR parameter, be that spin density, relaxation times, or the ADC.

2.5.1 Spin Density Imaging

Conceptually, the most basic type of imaging is spin density imaging. The output of this kind of imaging sequence is a profile of signal intensity, which is related to the local density of spins. In water-based systems, this in turn is related to the spatial distribution of water throughout the sample.

The challenge in a density-weighted sequence is to acquire all of the data in a time very short compared to T_2 to prevent relaxation time weighting. Although the

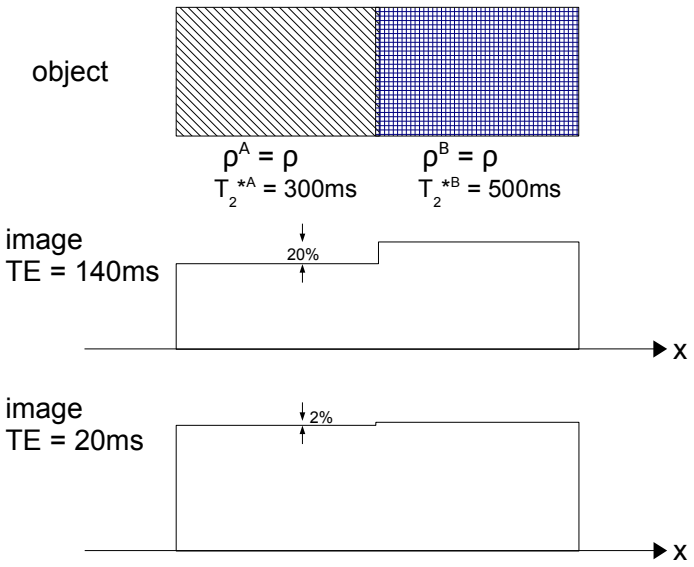

Figure 2.27: Signal weighting in an object with multiple relaxation times is reduced by using shorter delays.

initial image signal is proportional to the spin density, spatially-varying relaxation times may lead to an inaccurate representation of the true spin-density distribution. Relaxation effects become negligible in the limit that the time delay between signal excitation and acquisition is small compared to T_2:

$$\frac{\mathrm{TE}}{T_2} \ll 1 \tag{2.86}$$

As an example, consider the simple object in figure 2.27 and images acquired using a spin echo sequence (Fig. 2.24). The object is made of two different components, each having different values of T_2 ($T_{2A} = 300\,\mathrm{ms}$ and $T_{2B} = 500\,\mathrm{ms}$) but equal spin density. If the echo time is long ($\mathrm{TE} = 140\,\mathrm{ms}$, for instance), then the two components in the resulting image will not appear equal—because of relaxation, their intensities will differ by 20%. If, instead, the echo time is shortened (to, say, 20 ms), then the percent difference between the two materials in the image will drop to a more acceptable 2%.

2.5.2 NMR Parameter Mapping (T_1, T_2, ADC)

Spin echo imaging is a basic method for spatially-resolving the MRI signal. Beyond simple spin density imaging, though, it is possible to create maps of any of the other NMR parameters discussed thus far: T_1, T_2, and D. A generalized approach for this is to use a "magnetization preparation" to introduce sensitivity to the desired parameter followed by a spin echo sequence to spatially-resolve the signal. A series of images with varied weighting can then be fit voxel-wise to create a map of the desired parameter. The following describes the specific approaches for mapping the relaxation times and the ADC.

T_1: To map the T_1 parameter, an inversion-recovery magnetization preparation is used (Fig. 2.18). Additionally, a strong crusher gradient is placed immediately after the 180° inversion pulse to prevent refocusing of signal from imperfect inversion by the imaging gradients.

T_2: Mapping of T_2 is done using a CPMG magnetization preparation (Fig. 2.16). One advantage of the CPMG mapping sequence is that the spin echo imaging sequence simply adds one more echo to a *series* of echoes. As such, the signal amplitude of T_2 maps is free from relaxation weighting.

ADC: The ADC can be mapped using either a PGSE or a PGSTE magnetization preparation. The selection of one or the other depends on the relaxation times of the system: when T_2 is much shorter than T_1, the PGSTE variant may be advantageous.

Chapter 3

Materials and Methods

This chapter provides details about CPP bioceramic fabrication and the techniques used to measure drug elution and MRI in these materials. It includes sections on fabrication and handling of the CPP materials, the acquisition of optical photographs, the MRI apparatus and imaging sequences, and a protocol for drug elution measurements. Special focus is given to the optimization of the MRI sequences for the specific CPP system.

3.1 CPP Bioceramics Fabrication

CPP bioceramics are in the form of disks made from amorphous CPP powder. Through continued development, and using "gentle" incorporation techniques, two distinct types of material have been formulated. The first type incorporates vancomycin directly via mixing of a drug solution with powdered amorphous CPP. The material is then gelled by exposure to a humid environment for a set period of time, which has the effect of limiting drug release rates. This type is referred to as a "generation 1" or "G1" disk. The second type is fabricated using G1 disks as a starting material. Drug-loaded G1 disks are milled into a powder, which is then compacted and re-gelled. The resulting material offers even greater control over the release rates than G1 disks, and is referred to as a "generation 2" or "G2" disk.

This section contains the details of the CPP biomaterials used, including the fabrication of the raw CPP powder, the G1 disks, and the G2 disks, as well as storage, handling, and preparation of the samples for the MRI protocol.

3.1.1 Raw Powder

Calcium phosphate, monobasic, monohydrate ($Ca(H_2PO_4)_2{:}H_2O$) crystals (J.T. Baker company) are measured into a a Pt-5%-Au crucible. The crystals are placed in a

digitally-controlled furnace (Lindberg/Blue) and calcined by increasing the temperature linearly from 80 °C to 500 °C over a period of 1.5 hours. The temperature is then held at 500 °C, during which time hydrate water is progressively eliminated, and calcium polyphosphate (CPP) chains grow according to the reaction [26, 73]

$$n\mathrm{Ca(H_2PO_4)_2} : \mathrm{H_2O} \longrightarrow [\mathrm{Ca(PO_3)_2}]_n + 3n\mathrm{H_2O}.$$

After roughly 24 hours, the crucible is removed from the furnace and allowed to cool in a desiccating chamber. It is then weighed to verify that all hydrate water has been eliminated, as evidenced by a 21.97% mass loss.

The next step is to melt the crystals, which is done by increasing the temperature from 500 °C to 1100 °C at a rate of 10 °C/min, then holding at the high temperature for exactly 2.5 hours. The melt is then quenched by quickly pouring it into deionized water at room temperature, producing a CPP glass frit. To prevent reaction of the CPP glass, the water is quickly drained off, and the glass is washed twice in cleaning-grade ethyl alcohol, then once more in anhydrous ethyl alcohol. The glass frit is next placed in a vacuum desiccator for 2 days to allow the alcohol to evaporate.

Once completely dry, a powder is made from the CPP glass. Larger chunks of the glass are crushed into smaller pieces by pounding them in a steel container using a hammer. The glass chunks are then ground into a powder by repeated milling in a Fritsch Planetary Ball Mill. The powder is separated according to size by sieving in an Octagon Digital sieve shaker using an intermittent pulse pattern for 10 minutes, and a particle size range of $< 45\,\mu$m is extracted.

Once milling and size-separation is complete, the finished powder is stored in a vacuum desiccator in quartz scintillation vials to inhibit exposure to ambient air and humidity. Using solid-state nuclear magnetic resonance (NMR), the average CPP chain length of the amorphous powder has previously been found to be about 67 units [49].

3.1.2 G1 Protocol

The protocol for G1 disk fabrication largely follows that which was developed by Dion *et al.* [5]. Originally, this protocol was used to produce disks that were about 2 mm thick and 8 mm in diameter that were used both for experimentation and as the

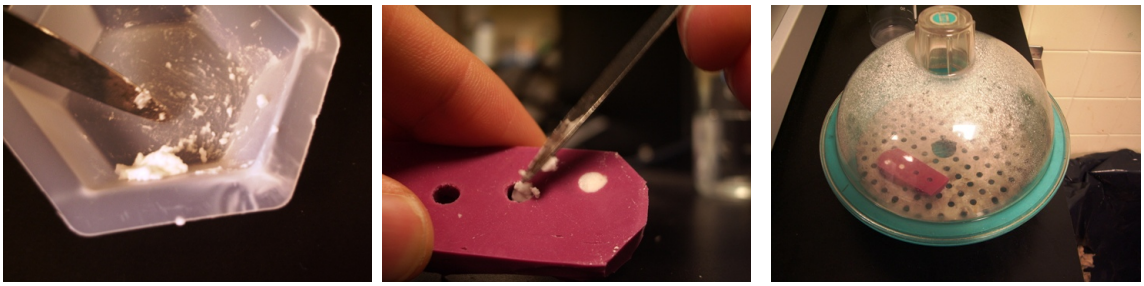

(a) (b) (c)

Figure 3.1: Steps in G1 disk fabrication: (a) the CPP, deionized H_2O and vancomycin are mixed together to form a paste; (b) the paste is formed into a disk shape using a polyvinylsiloxane mold; (c) during the gelling phase, the G1 disks are sealed in a plastic container maintained at 100% relative humidity and 37 °C.

precursor material for G2 disks. In the current context, however, a smaller disk size (4 mm diameter) is required for experimentation in the NMR apparatus. The large-size (8 mm diameter) disks are still used, but only as the G2 precursor. Additionally, the mass of vancomycin loaded in each disk has been adjusted because of changes in the scale of the elution apparatus. Considerations related to the modification of the drug loading protocol, including an experiment to assess sink conditions in the elution medium are addressed in detail in Appendix B.

In the first step of G1 disk fabrication, raw CPP powder (< 45 µm particle size) is mixed with deionized water and vancomycin (VCM) in the ratio 150 mg CPP : 60.2 µl H_2O : 3.630 mg VCM. In practice, the vancomycin is first dissolved in deionized water to make a solution with a concentration of 60.29 mg/ml, then 60.2 µl of the solution is combined with 150 mg of CPP in a polypropylene weigh boat. Using a metal spatula, the dry powder is incorporated bit-by-bit into the fluid to form a consistent, thick, white paste.

To cast the CPP into a disk shape, the paste is pressed into a flexible polyvinylsiloxane mold, taking special care to fill in the corners. Molds were produced for fabrication of large (8 mm) and small (4 mm) diameter disks, but in either case the disk thickness is about 1.6 mm. For efficiency, batches of several disks can be produced, but never more than 15 at a time, to prevent the paste from drying out during the process.

The gelling step is done in a sealed container stored in an incubator, which is maintained at a temperature of 37 °C. Within the container is a perforated metal

platform for supporting the disk molds, and below that the container is filled with deionized water, which acts as a reservoir to maintain 100% humidity. Once the disks are positioned on the platform, the lid is placed on the container forming an airtight seal to maintain the humidity. During the gelling stage, water reacts with the CPP powder to break the Ca^{2+} cross-links and hydrolyze the chains. Although the ambiant moisture supplies some water to the reaction, the greatest influence on the reaction rate is water that was directly mixed in to form the paste [49]. The gelling time is different for the two disk sizes: 5 hours and 2 hours for large and small G1 disks, respectively.

At the end of the gelling period, the disks and molds are removed from the sealed container and left in the incubator at ambient humidity to dry for 24 hours. The mean loading for G1 disks was (633.8 ± 5.2) µg, calculated in a method described in Appendix B.2.

3.1.3 G2 Protocol

The G2 protocol was originally developed to create CPP bioceramics with improved control over drug release [7]. It involves uniaxial compaction of a powder made from G1 disks, followed by an additional gelling step. For this reason it is referred to as a "compaction, re-gelling" protocol. Because G2 disks are used only for experimentation (and not as a stage in any further processing), only small-diameter (4 mm) G2 disks are produced.

To create the starting material for G2 disks, a number of large-diameter (8 mm) G1 disks are made using the steps described in the previous section. These disks are broken in half by hand and distributed between the two bowls of the planetary ball mill (to balance the weight), and are then milled for 30 seconds. The powder is then emptied into the test sieve system and run for 10 minutes using the intermittent pulse mode to extract a particle size range of 45 – 212 µm. Remaining particulate of size greater than 212 µm is then iteratively milled and sieved to obtain more powder in the desired size range, which is referred to as "G1 powder".

The compaction step is done using a hydraulic press (Carver ®) and a custom die-punch system. The die is a stainless steel slab with several chamfered holes bored through it (see Fig. 3.2(a)). The two punches are slightly different from each other:

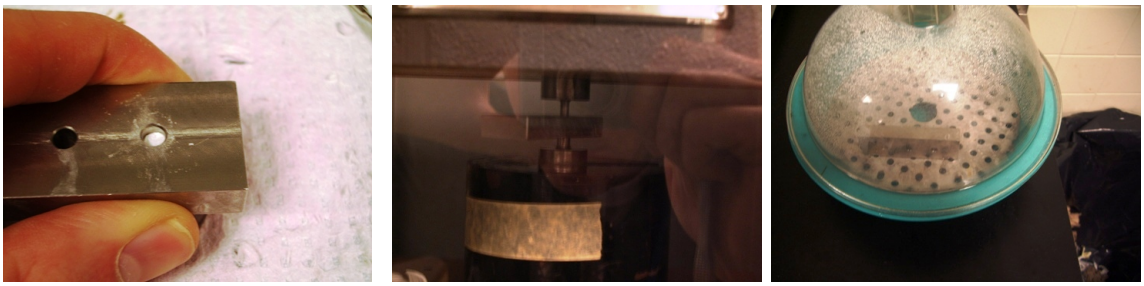

(a) (b) (c)

Figure 3.2: Steps in G2 disk fabrication: (a) G1 powder is measured into the metal die; (b) the powder is compacted in the die-punch system using a hydraulic press; (c) in the same manner as G1 disks, the G2 disks are gelled in a humid container.

one fits stably into place in the bottom hole, while the other plugs the top hole and slides to compact whatever is inside. To begin making a G2 disk, approximately 58 mg of G1 powder is measured out onto a piece of weighing paper, which is then used to funnel the powder into the die-punch system. The powder is then compacted under a pressure of 113 MPa for 5 minutes.

After compaction, the disks are gelled for 2 hours in much the same way as in the G1 protocol. One major difference is that the steel die exposes both faces of the disk to the humid air, so both faces are exposed to the gelling reaction. After gelling, the die is removed and placed in the warm, dry incubator so the disks can dry.

To remove the disks from the die, one of the punches, which is longer than the hole in the die, can be used to pop the disks out. The theoretical mass of vancomycin in the G2 disks was calculated using knowledge of the disk mass and the drug content of the G1 powder used in G2 disk fabrication. The theoretical loading for G2 disks was (650.7 ± 15.3) µg.

3.1.4 Storage, Handling, and Sample Preparation

A summary of the different types of materials and protocols used in CPP fabrication is given in Fig. 3.3. After fabrication and drying, all G1 and G2 disks are stored in quartz scintillation vials in a vacuum desiccator chamber until needed.

For imaging in the MRI apparatus, samples are prepared by mounting the disks in glass NMR test tubes (Wilmad-Labglass), which are 7″ long and have an inner diameter of (4.2065 ± 0.0065) mm. The samples are assembled so that the disks

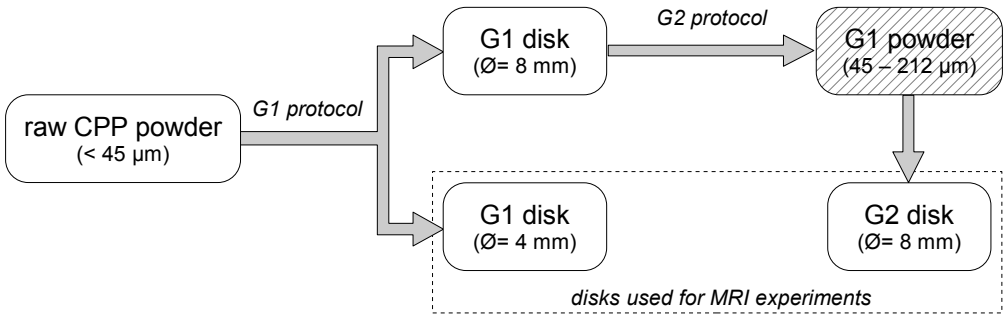

Figure 3.3: An overview of the materials and protocols involved in G1 and G2 disk fabrication. The boxes indicate the different kinds of materials involved and the arrows represent the protocols. *G1 protocol:* raw CPP powder is used to produce either large or small-size G1 disks. *G2 protocol:* large G1 disks are milled into G1 powder, which is then used to make G2 disks. The G1 powder is an intermediate material that is part of the G2 process (the hatching in this box is to highlight this distinction). Only the small G1 and G2 disks are used for MRI experiments.

are positioned away from the end of the tube using an Ultem^{TM} spacer, which is susceptibility-matched to water and helps to reduce the effects of magnetic field gradients near the air-tube interface. The cylindrical spacers are made flush with the end of the tube by actually positioning them at the *open* end, and the other (rounded) end is removed to provide access to the sample.

To prevent movement of the disk during the experiment, a small drop of cyanoacrylate cement (Krazy Glue ®) is used to affix the disk to the spacer. Additionally, to prevent fluid from leaking down along the sides, a thin bead of cement is applied around the end of the spacer before the disk/spacer assembly is quickly inserted into the NMR tube (because the cyanoacrylate sets very quickly). Once the cement is dry, the fully-assembled samples are stored in the vacuum desiccator until just before the start of the experiment. Figure 3.4 illustrates the steps in sample assembly.

The fluid medium used in the experiments is a deuterium-enriched phosphate buffer at physiological pH. Previously, Petrone *et al.* [7] used a 0.1 M TRIS buffer at physiological pH (7.4). The TRIS was selected because it is devoid of calcium or phosphorous, which would otherwise interfere with measurements of eluded calcium or phosphorous. In contrast, the element detected in MRI experiments is *hydrogen* (^{1}H), and to prevent interference with proton density measurements a phosphate

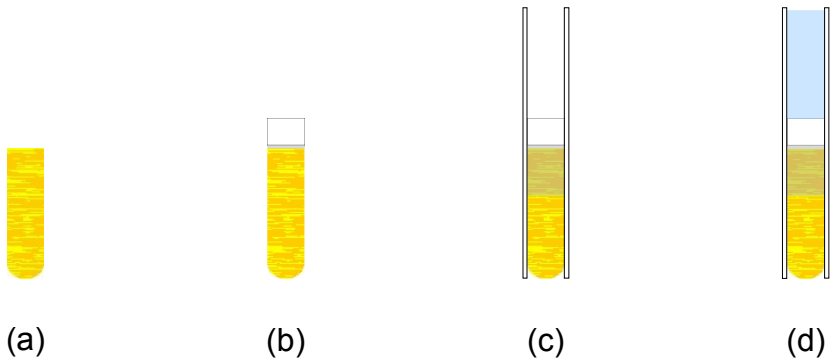

Figure 3.4: The assembly of a CPP sample for an imaging experiment: (a) An Ultem spacer is used to reduce gradients caused by magnetic susceptibility mismatch; (b) the disk is affixed to the spacer using cyanoacrylate cement; (c) a thin bead of cement is applied to the top of the spacer before the spacer/disk assembly is jammed into the open end of an NMR test tube; (d) the seal created by the cement prevents leakage from the bottom of the tube when the buffer solution is introduced.

buffer is selected.

The buffer stock is prepared by mixing 0.2 M solutions of $NaH_2PO_4{\cdot}H_2O$ and $Na_2HPO_4{\cdot}7H_2O$ and adjusting to pH 7.2. The stock is then diluted with 30% deuterium oxide (D_2O 99.9%, Cambridge Isotope Labs), yielding a final buffer concentration of 0.14 M. The reasons for including the D_2O are twofold. Firstly, the deuterium does not contribute to the imaging signal, and it is therefore a chemically-equivalent way to dilute the water and reduce radiation damping effects [74–76]. The second reason is that the MRI spectrometer can "lock" to the (independently-detected) deuterium signal for automatic field stabilization and to gauge the field uniformity while shimming.

At the very beginning of an experiment ($t = 0$), each sample tube is filled with approximately 1.8 ml of the deuterated phosphate buffer, which acts as a reservoir of fluid for the disks and the medium for drug elution. When not in the imager, the sample tubes are stored upright on an orbital lab shaker (Lab-Line), which is set to a rotational frequency of 40 rpm to simulate light agitation in a physiological environment.

3.2 Optical Photography

Digital photographs were taken of each sample at every timepoint so that macroscopic changes and swelling could be observed and recorded (see sample photograph, Fig. 3.5). Photos were acquired using a Pentax Optio S40 4.0 megapixel camera in macro mode using no flash. An NMR sample rack was positioned on a lab bench with the sample inserted into one of the slots, and the camera was positioned on a tripod so that the disk was located at the center of the field of view. The positions of the tripod and the rack were marked off to ensure that they were the same from shot-to-shot. In each photograph, a plastic ruler is held against the side of the NMR tube for scale .

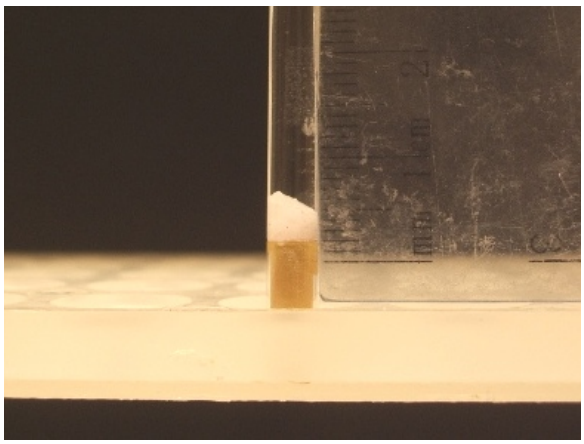

Figure 3.5: An example of an optical photograph taken of a CPP disk. The image shows the black background with the disk near the center in the NMR tube. The tube is positioned in a sample holder (white, bottom) and a ruler is positioned at the side of the test tube for scale.

3.3 Magnetic Resonance Imaging

As an imaging modality, MRI offers the ability to map parameters that are sensitive to different spatial and temporal scales. These parameters can be used in a complementary way to form a detailed description of the microstructure that controls the drug transport. This multi-faceted approach requires careful optimization of the imaging sequences to ensure accurate results. Depending on the kind of sample, challenges may arise due to changing morphology or relaxation times of the sample, or due

to complex biexponential relaxation/diffusion behaviour. This chapter describes the apparatus, imaging sequences, and basic data processing steps required for mapping spin-density, T_1, T_2, and the ADC in CPP bioceramics.

3.3.1 Apparatus

The MRI image acquisition was performed using a Bruker 500 Ultrashield vertical-bore superconducting magnet (11.7 Tesla) with an Avance 500 spectrometer. The spectrometer was controlled using the XWin-NMR software (version 2.6). The probe was a 5 mm ^{1}H probe with built-in, triple-axis (xyz) gradients (although a damaged y gradient meant that only the x and z directions were available). The maximum gradient strengths were measured to be the following:

$$\begin{aligned} G_x &= 50.838\,\mathrm{G/cm} \pm 0.15\% \\ G_z &= 70.67\,\mathrm{G/cm} \pm 1.48\% \end{aligned}$$

Prior to each MRI acquisition, the field was shimmed and the RF pulse width was calibrated. The probe was detuned with respect to the resonant frequency to give a 90° pulse, calibrated to 14.5 µs to ensure consistent detuning. This detuning step was done as a measure to reduce probe/sample coupling (i.e. radiation damping). Temperature in the probe was maintained at 20 °C at all times, chosen for consistency with the room temperature where the samples were stored, and because the diffusion coefficient of water is a well-characterized standard ($D = 2.0 \times 10^{-5}\,\mathrm{cm^2/s}$) at this temperature [77].

3.3.2 Pulse Sequences

The MRI pulse sequences used to image CPP are based on the sequences described in Chapter 2, although some have been modified slightly and the sequence parameters have been selected and optimized for CPP. This section describes important highlights of each sequence.

Sequence: Spin Echo Imaging

The spin echo imaging sequence (Fig. 2.13) maps the fluid distribution in CPP disks, but it also acts as the basis for spatial resolution in all the other sequences. As

such, the same imaging-related parameters discussed here apply generally to all the sequences.

The readout (imaging) gradient was aligned along the z direction to acquire a one-dimensional profile along the axis of the sample, and the magnitude was set to 37% of maximum, or $G_z = 2.615\,\mathrm{G/mm}$. The signal digitization involved sampling 256 complex points with a dwell time of 10 µs. The resulting field-of-view (FOV) was 8.98 mm and the resolution was $\Delta x = 35.1\,\mu\mathrm{m}$.

Because the T_2 in CPP contains a short component ($T_{2b} \approx 5\,\mathrm{ms}$), the echo time (TE) was selected to be as short as possible to prevent weighting in the images. This was aided by shortening the rewind gradient lobe while keeping the total gradient area the same by increasing the amplitude to 99%. The resulting TE was 1.547 ms.

Another element to the sequence is a short delay between turning on the readout gradient and turning on the digitizer. To acquire accurate image data, it is crucial that the gradients be steady, so a delay of 81 µs was included to allow them time to settle before the start of image acquisition.

The repetition time was chosen to be 5× the T_1 of the phosphate buffer. A TR of 15.9 s ensured full recovery of the signal between MRI scans (more on this in the following section on T_1 measurement).

Sequence: Spin Echo Imaging with an IR Preparation

The basic T_1 mapping sequence was modified slightly by including a crusher gradient following the initial inversion pulse to eliminate any transverse magnetization left due to imperfect 180° rotations. This gradient is directed in the xy direction so that the magnetization cannot be accidentally refocused later by the imaging gradient (which points along the z direction).

Initial measurements of T_1 in the phosphate buffer were made to determine the TR for all MRI acquisitions. The effect of dissolved vancomycin on T_1 was also measured to ensure the required TR would not change as the drug was released. The T_1 of the buffer alone was found to be found to be 3158 ms, and the T_1 of a 710 µg VCM solution (the highest value in the VCM calibration) was found to be 3179 ms. This is a mere 0.6% difference, and so the T_1 can be considered effectively invarient with the concentration of drug in solution. The TR reported in the previous section was

based on these measured values: TR $= 5\,T_1 = 15.9\,\mathrm{s}$.

A TR of 15.9 s is generally quite long for an imaging sequence. To illustrate this, the T_1 measurement itself involves $n = 4$ averages and 32 inversion times, making the total scan time about 34 minutes. Normally in a situation such as this, a contrast agent would be used to reduce the TR, but it has been found that CPP reacts readily with dissolved metal ions [78], forming a gel [23]. To prevent such reactions, no contrast agents were used, and the long scan times were accepted.

It was known that the longest/shortest T_1 components in the CPP system were about $T_{1a} = 3200\,\mathrm{ms}$ and $T_{1b} = 400\,\mathrm{ms}$, so a set of inversion times was chosen to cover both time scales. Thirty-two (32) values of TI were chosen between 1 ms and 6200 ms in equal steps of 200 ms. With respect to the relaxation times themselves, this set of times contains 10 points in the range $t = 0$ – $6\,T_{1b}$, and extends out to about $t = 2\,T_{1a}$, providing ample coverage of both components.

Sequence: Spin Echo Imaging with a CPMG Preparation

The CPMG magnetization preparation uses a short echo delay of $\tau = 1\,\mathrm{ms}$. Images were acquired from only the even echoes and at 16 total echo times ranging from TE = 6.4 to 500 ms. The number of images used to sample the T_2 relaxation is fewer than for the T_1 and ADC curves. This is because the phase program for the T_2 mapping sequence is twice as long as the the others, and sampling a full 32 points would make the acquisition prohibitively long.

Sequence: Spin Echo Imaging with a PGSTE Preparation

The basic ADC mapping sequence was modified slightly to include a low-level crusher gradient during the entire delay between the pulsed gradients. This serves to dephase any residual transverse magnetization due to imperfect z-storage. The imaging component of the sequence is also slightly different from those used in the other sequences in that there is no 180° pulse between the rewind/readout gradient lobes. There is still an echo formed, but it is a stimulated echo, and is formed from the delay between the excitation and storage pulses, with an effective echo time TE = 6.998 ms.

The pulsed gradients were sinusoidally-shaped lobes with 32 evenly-spaced gradient amplitudes between 11% and 98% of $g_{\max}$. The upper limit was chosen just short

of 100% to avoid potentially overloading the circuitry.

The selection of the δ and Δ parameters for the PGSTE magnetization preparation is based on diffusion-attenuation of the signal as well as on the T_2 and T_1 relaxation times, which dominate the relaxation in the δ and Δ time periods (respectively). Ideally, the τ delay (containing δ) should be small relative to the the shortest T_2, and the Δ delay should be small relative to the shortest T_1. Given preliminary knowledge of the short relaxation time components ($T_{1b} = 400\,\text{ms}$; $T_{2b} = 6\,\text{ms}$), the following diffusion parameters were selected.

$$\begin{aligned} \delta &= 2.000\,\text{ms} \\ \Delta &= 250.0\,\text{ms} \end{aligned}$$

A special calibration was performed to acquire accurate diffusion maps. While the same gradient hardware is used for both imaging and diffusion encoding, rapid gradient-switching (such as the pulsed gradients in a PGSTE sequence) can introduce errors that ultimately affect the scaling of the ADC. The effects that contribute to systematic ADC error are many and varied, and correcting for all of them individually can be excessively complicated. A pragmatic alternative is simply to use the diffusion sequence to acquire an ADC map of a sample that has a known diffusion coefficient. This map can then be used to scale all ADC maps obtained with similar sample geometry and acquisition parameters.

This approach was used to obtain a calibration for the ADC maps of CPP samples and was based on the known diffusion coefficient of water, $D = 2.0 \times 10^{-5}\,\text{cm}^2/\text{s}$ at $20\,^\circ\text{C}$ [77]. A phantom was made by using a pair of Ultem spacers to create a column of buffer fluid extending over the entire FOV of the experiment (just under 8.98 mm). A diffusion measurement was made using the using the same sequence and diffusion imaging parameters as used when imaging CPP.

Once the PGSTE data had been acquired, the data in each voxel were fit to a diffusion curve to obtain a spatial map of the diffusion coefficient (Fig. 3.6(a)). The spatial map, in turn, was fit to a 4th order polynomial to extrapolate the curve in the "gap" between the bottom and the (wrapped-around) top of the phantom, as well as to de-emphasize the noise. The diffusion profile, $D(z)$, obtained from the polynomial fit was then used to calculate a "scaling function", $S(z)$, which would then serve as

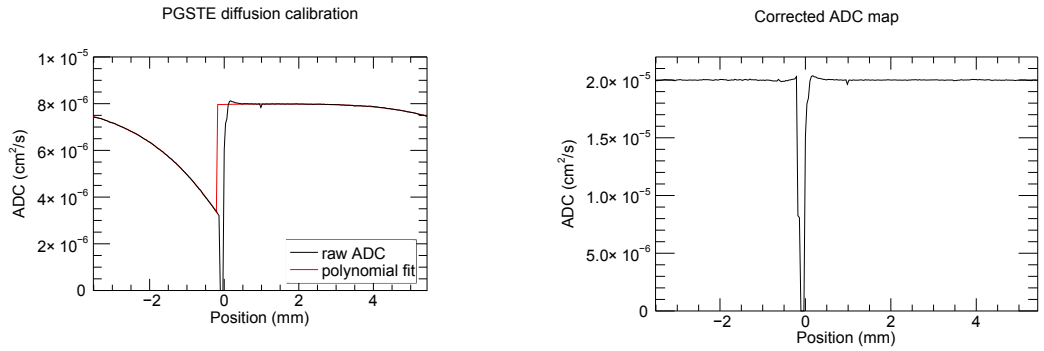

(a) (b)

Figure 3.6: Calibration of diffusion measurements: (a) the raw ADC map and the polynomial fit (b) the raw ADC, scaled by the correction function. The sample contains a water-based buffer at 20 °C, and thus the diffusion coefficient is $2.0 \times 10^{-5}\,\mathrm{cm}^2/\mathrm{s}$.

a multiplicative correction to other ADC maps.

$$S(z) = \frac{2.0 \times 10^{-5}\,\mathrm{cm}^2/\mathrm{s}}{D(z)} \tag{3.1}$$

Through multiplication by $S(z)$, ADC maps were corrected both for scaling errors, as well as for spatial non-uniformity. Fig. 3.6 shows the original diffusion calibration data with the $S(z)$ correction applied—the profile is now uniform and scaled to the known D-value for water at 20 °C.

3.3.3 General MRI Data Processing

The data from the MRI scans are one-dimensional (for spin density) or two-dimensional (for relaxation/diffusion) arrays of k-space data. Prior to analysis and interpretation, these are subjected to a series of processing steps to turn them into images or MRI parameter maps. The map data are then scaled/shifted to allow comparison between samples. This section describes these steps, as well as the least-squares fitting approach that is used to derive parameter maps for the relaxation/diffusion data.

k-Space Operations and Fourier Transform

A Fast Fourier Transform (FFT) is used to convert raw k-space data into images. Prior to the FFT operation, however, the k-space data are baseline-corrected to remove any DC spikes from the images and a Hanning filter is applied to eliminate

Gibbs ringing. The complex k-space data are also phased to ensure they are fully real.

A simplistic approach to the problem of phasing is to take the *magnitude* of the complex points. This approach, however, sacrifices the sign $(+/-)$ of the data, which can be important when 1) T_1 inversion recovery data is concerned, because the starting magnetization is negative; and 2) in T_2 or ADC data when the signal is low, because a straightforward magnitude calculation may positively bias the noise. To correct phase without loss of the sign, a map of the phase error is obtained from an image in which every point is known to possess positive signal. For inversion-recovery data, this is generally an image acquired at late t (TI $\gg T_1$); for T_2 or ADC data, this is generally the first image in the series (at TE $\ll T_2$ or $g \ll g_{\max}$, respectively).

Image Intensity Scaling and Alignment

Consistent scaling of the images is required for comparison of data over several days in a timecourse experiment. One approach would be to include an object in the image that possessed constant proton density so that, at each timepoint, that object could be used as a scaling reference.

In effect, this was done previously [23], where the phosphate buffer in the region above the disk was used as an endogenous reference. There are two problems with this approach, however. Firstly, as a disk swells, it may intrude on the buffer region used for scaling. Secondly, this reference region is necessarily *away* from the middle of the probe where the disk is centered. The roll off in this region is different for each acquisition due to the energy absorbed by a changing water distribution in the disk, so this approach can lead to incorrect image scaling.

An alternative is to simply scale the images by the gain of the receiver amplifier. This ensures normalized data, even when the receiver gain is changed. This is particularly important in the present experiment, where one of the measures to reduce radiation damping was detuning of the probe. The 90° pulse width was always intentionally set to the same value (`p1` = 14.5 µs), and as a result, the receiver gain was always set to the same level (for each distinct type of scan).

A second step required for comparing images was alignment along the z direction. A sample gauge was set and used for consistent positioning at each time point, but this

could not account for the slight differences in position of the disks *between* samples.

For averaging data from several disks, the images had to be shifted so the bottom of each disk lined up. This was done by masking out regions containing only noise. In practice, in the aliased (wraparound) images, this region was in the space between the top of the water column roll off and the bottom of the disk. The images were masked to zero in this region based on the noise threshold, and the bottom of the disk was shifted to appear at $z = 0$ in the image.

Least-Squares Fitting

In the T_1, T_2, and ADC data sets only, the series of images needed to be fit to model equations so as to derive the corresponding parameters. The canonical equations for these parameters are as follows:

$$M(\mathrm{TI}) = M_0 - M_{\mathrm{inv}} e^{-\mathrm{TI}/T_1} \tag{3.2}$$

$$M(\mathrm{TE}) = M_0 e^{-\mathrm{TE}/T_2} \tag{3.3}$$

$$M(g) = M_0 e^{-D\gamma^2 g^2 \delta^2 (\Delta - \delta/3)} \tag{3.4}$$

These are a 3-parameter model for T_1 and 2-parameter models for T_2 and D. The final equation is frequently simplified by defining the variable

$$b \equiv \gamma^2 g^2 \delta^2 (\Delta - \delta/3). \tag{3.5}$$

The diffusion equation thus becomes

$$M(g) = M_0\, e^{-Db}. \tag{3.6}$$

When describing data that are apparently biexponential, the following modified forms are used to account for the additional component:

$$M(\mathrm{TI}) = M_0 - M_a e^{-\mathrm{TI}/T_1 a} - M_b e^{-\mathrm{TI}/T_1 b} \tag{3.7}$$

$$M(\mathrm{TE}) = M_a e^{-\mathrm{TE}/T_2 a} + M_b e^{-\mathrm{TE}/T_2 b} \tag{3.8}$$

$$M(g) = M_a e^{-D_a b} + M_b e^{-D_b b} \tag{3.9}$$

The last equation includes the b-value, which is not to be confused with the subscript (i.e. D_b), which is just a label for one of the pools involved in spin-exchange.

The factors M_a and M_b in equations 3.7–3.9 represent the amplitude (or "weighting") of the "a" and "b" components in the signal. In the limit of slow exchange, these are proportional to the population of spins in the respective pools, although in general the amplitudes are a function of the spin-exchange rate (this effect is termed "exchange weighting").

The relaxation/diffusion data were fit using the Minpack-1 least-squares fitting algorithm [79]. The uncertainties used in the algorithm were obtained in a special error measurement. Repeated single scans are performed with each sequence and its default parameters, and the uncertainty is estimated as an average of the standard deviation over all the voxels in the image (this characterizes the noise).

In the images of the CPP samples, the pure buffer is the only region that is monoexponential at all times. Within the disk, the relaxation/diffusion parameters may be either mono- *or* biexponential, depending on the position, and this can also change as a function of time. To address this characteristic, the data at each time point was fit to both the monoexponential and biexponential versions of the function. The quality of *any* fit will always improve when using a model that contains more parameters, so a cost function was used to gauge the the improvement to the fit against the cost of including the extra parameters. This function was based on the χ^2 of the two types of fits, and had the following form,

$$\frac{(\chi_m^2 - \chi_b^2)}{\chi_b^2}, \tag{3.10}$$

where the subscripts m and b denote monoexponential or biexponential, respectively.

After computing the cost function, map regions were designated mono- or biexponential based on thresholding this function. Subsequently, the data were classified into components (a and b) according to continuity of the component amplitudes. Specifically, the buffer region was identified as the long/"free-water" a-component. At the interface between the disk and the buffer, where there exists the second component, the a-component is identified by matching the amplitude with that of the pure buffer at the interface.

3.3.4 Averaging MRI Data

The result of data acquisition and processing is a series of single-valued spin-density maps and biexponential T_1, T_2, and ADC maps for each sample at each time point. These maps may be analyzed using various approaches. The simplest is to display the time-series of maps for each sample separately, but to analyze trends requires averaging the data. This is particularly challenging with the biexponential data format, which is defined by no fewer than four parameters. The goal of this section is to describe how data from multiple samples at a given time point are averaged together, as well as to describe how a region-of-interest analysis was used to show trends in the time-evolution of the MRI parameters.

Averages of Parameter Maps

To obtain averages of MRI parameters requires summing data from multiple samples. This is most straightforward in the case of the spin-density maps, which are always single-valued functions. At a given z position, one can simply compute the average and standard deviation of the spin density for a number of samples, s. The resulting spin-density maps represent the average fluid distribution in the disks.

The computation of averages is more complicated when analyzing maps of relaxation times or the ADC, because the signal contains contributions from "free" and "bound" water, where both components are in exchange. Depending on the exchange regime (slow, intermediate, or fast) the signal may appear to be biexponential (two components) or monoexponential (one component). It is important to emphasize the distinction between the *water* components and the *signal* components. One is a physical classification of the water in the local CPP microstructure based on rates of molecular motion, and the other is a function of 1) the signal from these components, 2) the method used to detect the signal, and 3) the exchange between the components. The following is a description of the approach for averaging biexponential maps.

Defining P as a general parameter (i.e. either T_1, T_2, or D), the problem of biexponential averaging is addressed by labeling signal components as "a" or "b", where the a-component is the one with the greater parameter value ($P_a > P_b$). At certain positions in the maps at certain times, there may be only one signal component apparent. In these cases, the signal is labeled "a" or "b" based on continuity with signal

components nearby. The calculation of the averages are as follows, where s is again the number of samples.

1. The component amplitudes are a straightforward average.

$$\begin{aligned} A_a &= \sum_{i=1}^{s} M_{a,i} \\ A_b &= \sum_{i=1}^{s} M_{b,i} \end{aligned}$$

2. The average of the parameter components is weighted by the associated amplitudes.

$$\begin{aligned} P_a &= \frac{\sum_{i=1}^{s} M_{a,i} P_{a,i}}{A_a} \\ P_b &= \frac{\sum_{i=1}^{s} M_{b,i} P_{b,i}}{A_b} \end{aligned}$$

3. The uncertainty in amplitude is just the standard deviation.

$$\begin{aligned} \delta A_a &= \sqrt{\frac{\sum_{i=1}^{s} (M_{a,i} - A_a)^2}{A_a}} \\ \delta A_b &= \sqrt{\frac{\sum_{i=1}^{s} (M_{b,i} - A_b)^2}{A_b}} \end{aligned}$$

4. The uncertainty in the parameters is the standard deviation weighted by the amplitudes.

$$\begin{aligned} \delta P_a &= \sqrt{\frac{\sum_{i=1}^{s} A_{a,i} (P_{a,i} - P_a)^2}{A_a}} \\ \delta P_b &= \sqrt{\frac{\sum_{i=1}^{s} A_{b,i} (P_{b,i} - P_b)^2}{A_b}} \end{aligned}$$

In the limit of slow exchange, the amplitude maps can be interpreted as the fluid distribution for each component (a/b) separately. When exchange is *not* slow, the amplitude maps correspond less closely to the true fluid components, and the amplitudes must be interpreted with care.

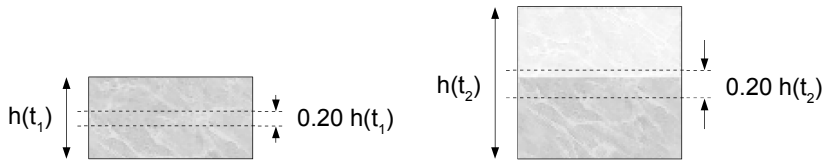

Figure 3.7: Schematic of an ROI in a swelling CPP disk, shown at two times ($t_2 > t_1$). The region is always defined as the middle 20% of the disk height, so it shifts upwards *and* becomes larger as the disk swells.

Averages in a Region-of-Interest

Each set of MRI data contains spatial information (the 1-D profiles) at several time points. For the purpose of visualizing average behaviour within the disk, it can be useful to examine the parameters internal to the disks as a function of time.

One approach that has been used previously is to display the time-evolution of parameters at a single point (i.e. voxel) in the 1-D profiles [23]. This has the advantage of simplicity, but there are two major disadvantages. One is that the disks swell a great deal, so the material included in the voxel will generally be different at every time point. The other is that the MRI parameters are never uniform across the extent of the disk, and the data at a single point cannot account for this variation.

An alternative approach is to define a region-of-interest (ROI) within the disk and to average the parameters over this region. This ROI analysis was performed on G1 and G2 disks using a region defined as a fraction of the disk height, determined from the optical data. The analysis was done by using the average disk height at each time point, and selecting the middle 20% of this range (see Fig. 3.7). Selecting the range in this way helps to account for the effects of swelling, because the ROI volume adjusts with the disk volume. Additionally, the spatial variation over the range can be accounted for by computing the standard deviation. In this context, the standard deviation represents the inter-sample variation in the parameter in the chosen ROI.

3.4 Ultraviolet/Visible Spectrophotometry

Ultraviolet/visible (UV/Vis) spectrophotometry is used in the quantitative analysis of solutions containing transition metals and highly-conjugated organic compounds. It makes use of the familiar Beer-Lambert Law, which says that absorbance of light at a given wavelength through a substance of pathlength L is proportional to the solution concentration (c) [80].

$$A = -\log_{10}(I/I_0) = \epsilon c L \tag{3.11}$$

Here, I/I_0 is the ratio of transmitted/incident light and ϵ is the extinction coefficient (characteristic of a given solute). In general terms, a measurement is made of the transmitted light intensity at constant L and compared with a reference beam. The solution concentration is then obtained via comparison with a calibration curve or from the extinction coefficient (if it is known).

Absorbance readings of the elution medium were used to measure vancomycin release from CPP disks, and this section describes the apparatus and calibration for these measurements, as well as the calculation of cumulative mass released.

3.4.1 Apparatus

Absorbance readings were acquired using a SpectraMax^{384} Plus Microplate Reader (Molecular Devices) with a scanning range between $\lambda = 190$ to 1000 nm. A quartz 96-well microplate was used for transparency in the UV range [81], and all readings were made in triplicate using 200 µl in each well.

3.4.2 Vancomycin Concentration Measurements

Actual solution concentrations were obtained using a calibration, which was based on a serial dilution of a 512 µg/ml solution of vancomycin prepared in the same 0.14 M phosphate buffer as used in the experiments involving CPP.

Wavelength Selection

Spectra from the serial dilution are shown in Fig. 3.8 (along with the spectrum from the buffer alone). Each spectrum was sampled in 10 nm intervals from 180 to 500 nm.

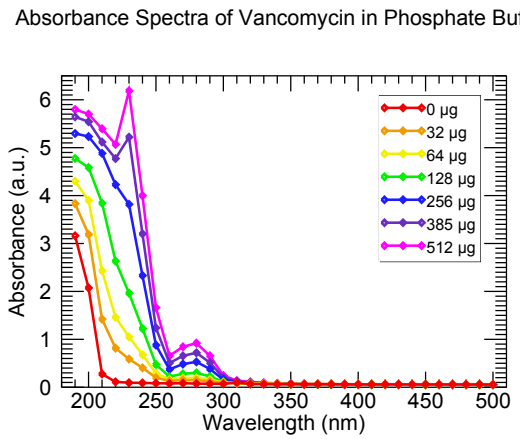

Figure 3.8: Absorbance spectra for a serial dilution of a vancomycin solution in phosphate buffer. The concentration is indicated by the line colour according to the legend, and the the phosphate buffer alone (0 µg/ml) is shown in red. The vancomycin peak is located at 280 nm.

The spectra of the vancomycin solutions reveal absorbance peaks at 230 nm and 280 nm, both in the ultraviolet region. While the 230 nm peak is more intense, there is interference with a feature in the buffer spectrum at low λ, so the 280 nm peak was chosen for the absorbance measurements.

Concentration Calibration

The peak absorbance of the series of vancomycin solutions was used to obtain a calibration for the UV/Vis readings. The calibration curve is shown in Fig. 3.9. The absorbance measurements showed non-linear effects at the concentrations above 256 µg/ml, so the calibration curve was fit using only the lower concentrations. The errors could be due to non-linear optical effects, but may also be due to pathlength errors from the meniscus in the higher-concentrated (higher-viscosity) solutions. The error in the absorbance at higher concentrations is of no consequence however, because the highest concentration reached in any of the samples was 150 µg/ml, which is well within the linear range.

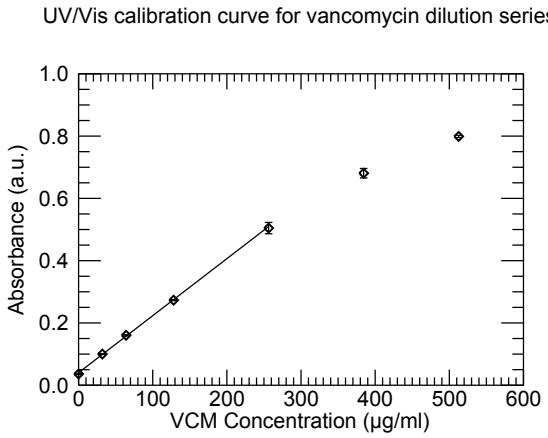

Figure 3.9: The VCM concentration calibration for UV/Vis measurements. The curve is linear only for the concentrations up to 256 µg/ml.

Pathlength Correction

The UV/Vis spectrophotometer offers an option for pathlength correction. This feature uses a secondary absorbance measurement at $\lambda = 900\,\text{nm}$ (near-infrared) to correct for systematic error in height of fluid in the well. These errors can arise due to surface tension or errors in dispensing fluid with the pipette.

This automated pathlength correction feature was tested using both pure H_2O and pure D_2O, and it was found that D_2O had a significantly greater absorbance in the near-infrared wavelength range. Because of this difference in absorbance, this feature was not employed in the absorbance measurements.

Uncertainty

The triplicate concentration readings were used to calculate the average and standard deviation. The standard deviation accounts for instrumental uncertainty, as well as random uncertainty in pathlength (such as those associated with error in pipetting technique).

The uncertainties calculated in this fashion do not account for systematic error, such as that from surface tension in solutions having different VCM concentrations. However, recalling that the calibrations were linear in the $\lambda < 256\,\mu\text{g/ml}$ range, and that the concentrations measured in the samples remained well within this range,

surface tension effects are unlikely to be an important contribution to error under these conditions.

3.4.3 Drug Elution Measurement

In overview, the procedure for measuring the mass of drug eluted from the CPP samples involved drawing an aliquot of elution medium, measuring the absorbance to get the VCM concentration, and calculating the mass from the fluid volume.

Conceptually, the basic procedure involves drawing a 1000 µl aliquot from the 1.8 ml of elution medium in the sample at each time point, then replacing the sampled medium with 1000 µl of fresh buffer to maintain the total volume.

The actual procedure is slightly more complicated than this. The micropipette tips used for drawing the aliquot would not fit in the long, narrow NMR tubes. Because of this, the entire volume of elution medium was removed from the NMR tube using a long-tipped glass pipette and transferred to an 18 ml polypropylene Falcon tube (BD Biosciences). The fluid in the tube was first agitated to ensure a homogeneous drug concentration, then the 1000 µl was drawn from the Falcon tube and stored in a sealable 1.5 ml centrifuge tube (Eppendorf AG). The 1000 µl of buffer was replenished with fresh stock in the Falcon tube, and the entire volume transferred back to the NMR tube using a long-tipped glass pipette.

The 1000 µl aliquot in the Eppendorf tubes were centrifuged for 10 s to separate out any particulate matter, and 900 µl were drawn by micropipette and stored in new Eppendorf tubes until the absorbance could be read.

When acquiring the absorbance measurements, 600 µl from each aliquot were divided evenly between 3 wells in a 96-well quartz microplate (200 µl each). The absorbance reading at $\lambda = 280$ nm was recorded, and converted to a VCM concentration using the calibration curve.

3.4.4 Drug Mass Calculation

This section describes how the absorbance readings and the volumes of elution medium were used to calculate the amount of drug eluted. The basic calculation (used in previous work) is described first, followed by a modification that was developed to account for fluid losses that accumulated during the transfer process.

Basic Calculation

The basic calculation for the mass of eluted drug accounts for the concentration in the sampled medium and the drug mass in the remaining elution medium. At the n^{th} measurement time point:

- V_n is the volume of elution medium in the test tube ($V_0 = 1.8\,\text{ml}$);
- R_n is the concentration reading (in µg/ml);
- ΔV is the volume of the aliquot (1.000 ml);
- m_n^* is the drug mass remaining in the tube after the aliquot has been taken, where

  $$m_n^* = (V_n - \Delta V)\, R_n; \tag{3.12}$$

  (the elution medium contains no drug to start with: $m_0^* = 0\,\mu\text{g}$.);
- m_n is the mass of drug released between the $(n-1)$ and n^{th} time points, where

  $$m_n = V_n R_n - m_{n-1}^*. \tag{3.13}$$

With these definitions, the cumulative mass released by the n^{th} time point is

$$m(t_n) = \sum_0^n m_n \tag{3.14}$$

Correction for Fluid Losses

Compared to the 15 ml of elution medium used in the previous experiment, 1.8 ml is a relatively small volume. Because of this, small losses incurred during the transfer of fluid can accumulate and result in a significant drop in the volume of elution medium.

Because the inner diameter of the NMR tubes is known to high precision, the losses can be accounted for by measuring the change in the height of the the buffer column before and after the aliquot is acquired. The volume at the n^{th} time point is related to the volume at the previous time point and the change in height by the following equation.

$$V_n = V_{n-1} - \pi r^2 (h_n - h_{n-1}) \tag{3.15}$$

Disk ID	Mass (mg)	Disk ID	Mass (mg)
G1-BAK-6.1	32.6	G2-MRI-6.8	53.4
G1-MRI-6.2	33.4	G2-BAK-6.9	54.4
G2-MRI-6.4	52.7	G1-MRI-6.10	32.5
G2-BAK-6.5	51.4	G1-BAK-6.11	32.4
G1-MRI-6.6	32.7	G2-MRI-6.12	54.9
G1-BAK-6.7	32.7	G2-BAK-6.13	54.6

Table 3.1: The six G1 and six G2 samples used in the experiment

The volume loss at each measurement time point was approximately 50 µl ($\approx 3\%$ of V_0). While the losses can be accounted for using equation 3.15, without being replenished, the cumulative volume losses could potentially lead to a violation of sink conditions. To prevent this from happening, the buffer was replenished to 1.8 ml at three times in each series, with the volume of added buffer included in calculations.

3.5 Experiment: Samples and Protocol

In overview, the experiment to analyze degradation and drug release in CPP disks involved MRI scans, photography, and elution measurements conducted on 3× G1 and 3× G2 disks. Each disk was observed over a two-week period following its immersion in a buffered fluid. An extra 3× G1 and 3× G2 samples were prepared as "backup" samples. Photography and elution measurements *only* were conducted on these samples, which could be substituted in case any of the primary (MRI) samples were compromised during the time-course experiment. The primary and backup samples were treated in the same way, with the exception that the primary samples spent 2 hours per day in the MRI system while the backup samples remained on the orbital lab shaker during that time.

Prior to fixation in the sample tubes, the disks were weighed and given an identification label, which indicates the disk type, whether it was an MRI or backup (BAK) disk, and a unique serial number. For example, the label

G1-BAK-6.1

denotes a G1 backup disk with serial number 6.1. Table 3.5 gives a list of all the disks and their dry, starting masses.

The experimental protocol involved MRI measurements at 15 time points. After immersion in the buffer at time $t = 0$, the samples were scanned at times $t = 1$ hour, 12 hours, 24 hours, then every 24 hours thereafter up to 13 days post-immersion. At each measurement time point, the following procedure was followed:

1. The sample was removed from the orbital lab shaker, and an aliquot of the elution medium was acquired
2. A photograph of the sample was acquired
3. The sample tube was placed in a gauge to ensure centering of the disk in the RF probe
4. The probe was tuned and the field was shimmed with the sample in the magnet
5. A spin-density map was acquired (1 min)
6. T_1 data were acquired (39 min)
7. T_2 data were acquired (33 min)
8. ADC data were acquired (32 min)
9. The sample was replaced on the orbital lab shaker

The times indicated in parentheses represent the duration of the MRI scans.

The time that consecutive samples were immersed in buffer was staggered by two hours to account for the time of the MRI scans. As such, MRI scans for each sample occurred at approximately the same time points (relative to the immersion time of that particular sample).

Due to limitations on scheduling magnet time, only two MRI samples could be scanned per day. As such, this experiment was conducted on groups of 2× MRI and 2× BAK samples at a time. To study all the samples, this required three blocks of 14 days each, for a total experiment duration of 36 days. No samples were compromised, so MRI data is available at every timepoint for all of the primary disks.

A note on data averaging: because optical and elution data were acquired for both the MRI and BAK samples, it is possible to include the backup-sample data to obtain better averages for these measurement. Averages may be computed based on

just the MRI samples ($n = 3$), *just* the BAK samples ($n = 3$), or the combined set of all MRI and BAK samples ($n = 6$). When referring to this last grouping, the label "ALL" is used.

3.6 Summary

This chapter described the steps involved in the fabrication of vancomycin-loaded G1 and G2 disks. An experimental protocol was devised that allows for characterization of the disk morphology and microstructure concurrent with drug elution measurements. The structural analysis uses techniques of optical photography and MRI data acquisition. The latter, in particular, was extensively optimized for imaging CPP bioceramics, and the results of this characterization will be described next in Chapter 4. The drug elution measurements are done using UV/Vis spectrophotometry, and these results will be discussed in Chapter 5, which also presents an analysis of the correlation with the structural characterization.

Chapter 4

MRI-Based Characterization of CPP Morphology and Microstructure

Drug release from biomaterial implants is the product of various mechanisms working at both the macroscopic and microscopic levels. Particularly where controlled release is an aim, interplay between multiple mechanisms can lead to highly dynamic, complicated systems. In some cases, models have been developed with the aim of relating measurable, physical characteristics of a system to release rates. While a comprehensive model of CPP drug release is beyond the scope of this work, an important step is to assess the effect that morphology and microstructure have on the drug release, and to thereby determine the dominant mechanisms at work.

Together MRI and optical imaging provide complementary means of probing the physical characteristics of CPP. The main focus of this chapter is a description of measurements using optical photography and MRI techniques (spin-density, T_1, T_2, and ADC mapping) that were performed longitudinally on G1 and G2 disks as a function of exposure to a buffered fluid. These data are analyzed together to obtain a description of disk morphology and microstructure.

Prior to discussion of the experiment and the results, this chapter begins with an overview of parameters that have been included in various models for drug delivery systems. While none of them are specific to CPP, together they provide a kind of inventory of the variables that are generally considered important for drug release. In this context, the physical characterization put forth in this chapter provides a framework for the following chapter, in which the physical changes are compared with drug elution to elucidate the transport mechanisms at work in CPP bioceramics.

4.1 Background: Morphology, Microstructure and Drug Release

All models for drug release have in common the fact that they relate physical characteristics of the drug/material system to rates of drug release. Frequently, models are

rudimentary, semi-empirical, and based around extremely simplified systems. These may account for geometry of the delivery matrix, but describe release through generalized diffusive or structural relaxation mechanisms (without taking into account their physical basis). Other models attempt to incorporate more realistic mechanisms, but since real drug release systems can be quite complex, models that attempt to more accurately predict behaviour can quickly become unwieldy [82]. Sometimes, the only feasible approach is to identify the two or three variables that have the greatest impact and use those to approximate the system.

In a review of models describing controlled-release devices, Siepmann and Peppas [82] discuss the following as common parameters included in the models: 1) diffusivity; 2) swelling; 3) erosion; 4) geometry; 5) drug characteristics; and 6) drug/matrix interactions. The following is a summary of these parameters, how they interact with drug release systems, and their expected effect on release rates. They are framed here with the purpose of accounting for how each may influence optical/MRI data, and therefore give insight into the mechanisms at work in CPP.

1. **Diffusivity:**

   The diffusivity (ADC) of drug in CPP matrices is closely tied to the presence and transport characteristics of absorbed water. Water is responsible for both the initial dissolution of the drug and subsequent transport through the CPP matrix, but it also interacts with the CPP itself, leading to changes in the microstructure that vary both spatially and temporally. In turn, the local microstructure determines the diffusivity of the drug, and ultimately the net rate of drug release.

   Since both G1 and G2 disks have some degree of initial porosity, diffusion of drug at the *earliest* times is likely through pores in the material. However, the material gels over time, and the transport mechanism likely shifts toward diffusion through a cross-linked matrix of CPP chains. The following is a list of factors that may affect drug diffusivity in gelled CPP, along with their expected effect on drug transport rate.

   - The local concentration of absorbed water [increases rate]

- The degree of swelling that has occurred (i.e. chains grow further apart) [increases rate]
- The degree of chain scission [increases rate]
- The effect of dissolution products on local viscosity [decreases rate]

Under some conditions, partial crystallization of CPP has been found occur in aqueous environments; however, the work of Djogbenou *et al.* [49] has shown that G2 disks in a TRIS physiological buffer remained amorphous, so for the disks used in the present work, it is highly possible that no crystalline material is formed (CPP or CPMM*), at least at early times (up to 10 days).

While the diffusivity of the drug and of the absorbed water are *not* equivalent, they are related because water is the medium through which transport occurs. Using the MRI techniques, characteristics of water diffusion in CPP can be seen in various ways. Firstly, a series of spin density maps can show the gradual infiltration of buffer into the disk, which is a result of diffusion of the buffer over a long timescale (hours and days). In contrast, the ADC maps depict local diffusion on a shorter timescale (milliseconds) and give a direct, quantitative measure of diffusivity. While the T_1 and T_2 maps are not direct probes of diffusive motion, they are indicative of molecular tumbling mobility, which can reveal other aspects of the confining microstructure.

2. **Swelling:**

   Swelling has various effects:

   - It increases the distance between the surface and points internal to the matrix [decreases rate]
   - It reduces the concentration (and thus the driving force) of drug remaining in the disk [decreases rate]
   - It increases the separation between chains, promoting diffusion [increases rate]

*calcium phosphate, monobasic, monohydrate

Evidence for swelling can be seen in spin density maps, which show motion of the disk/buffer interface; however, the transition in spin density between disk and buffer is a smooth one, and optical photographs tend to show the interface more clearly.

3. **Bulk erosion:**

   Bulk erosion refers to degradation of the disk structure, with the material fragmenting due to agitation from the buffer medium or internal stresses. When a material erodes in this fashion, the effect is to create a greater surface area, which should tend to cause the rate to increase.

   The best evidence for bulk erosion comes from the optical photographs. Although the phenomenon is difficult to characterize, the rupture of a disk may represent a discontinuous change in the kinetics of drug release, so it may be possible to look for correlation between disk rupture and sudden changes in drug release.

4. **Geometry:**

   Geometry of a controlled-release material governs both fluid penetration and drug transport from the material. Geometrical changes can be associated with device swelling. In some cases this is simply a change in the original dimensions, but in other cases this may be a major alteration of the form of the device. As for CPP disks, the initial form is cylindrical, with the top and sides of the disk in contact with the buffer, and the three-dimensional (3-D) character of the disks is prominent. Swelling quickly puts the disk in contact with the walls of the NMR tube, and thereafter the geometry becomes very simple, with fluid/drug transport being effectively 1-D. Later still, uneven swelling may cause the top face of the disk to become slanted, which may also expose sections of the side surface. Along with rupture of the disk, this can create a more complex geometry in which the 3-D character of the sample once again factors in to the drug release.

   At early times in the elution period, the approximation of 1-D transport is reasonable. When swelling alters the cylindrical geometry, the optical photographs

give the best picture of what is taking place. Although it is difficult to quantify geometrical changes or to describe their effect on release, it may be possible to observe correlation between major changes in geometry and drug elution.

5. **Drug characteristics:**

   Drug solubility is known to play a part in determining release rates. However, vancomycin in CPP is initially loaded via solution so it is known that no solubility limits are being exceeded. As such, this parameter is considered to be of lesser importance in the CPP/vancomycin systems.

6. **Drug-matrix interactions:**

   Chemical bonding or matrix entrapment of an incorporated drug may be a very important mechanism of release in drug delivery materials. Raman scattering has previously shown no interaction between vancomycin & CPP [6], but solid-state ^{31}P NMR reveals some inhibition/enhancement of bond rotation at certain sites. However, this is not thought to be a major contributor to release characteristics [49].

   The physical entanglement of drug by the CPP chains is a potentially important rate-controlling mechanism. Somewhat counter-intuitively, larger drugs such as vancomycin have been found to elute more rapidly because the degree of entanglement is less than with smaller drugs. In CPP, this is thought to be because the molecular chains tend to be much shorter ($\approx 20 - 40$ units) than in most common polymers (thousands to millions of units). Because of this, a drug molecule with a size similar to/larger than the chains may become less ensnared than a smaller drug. Nonetheless, rupture of chains and swelling still create an environment with less hindrance to mobility, and should therefore result in increased release rates. The "opening up" of the CPP microstructure due to swelling and chain scission may be apparent in the MRI relaxation/diffusion maps, and this might be correlated with changes in drug release rate.

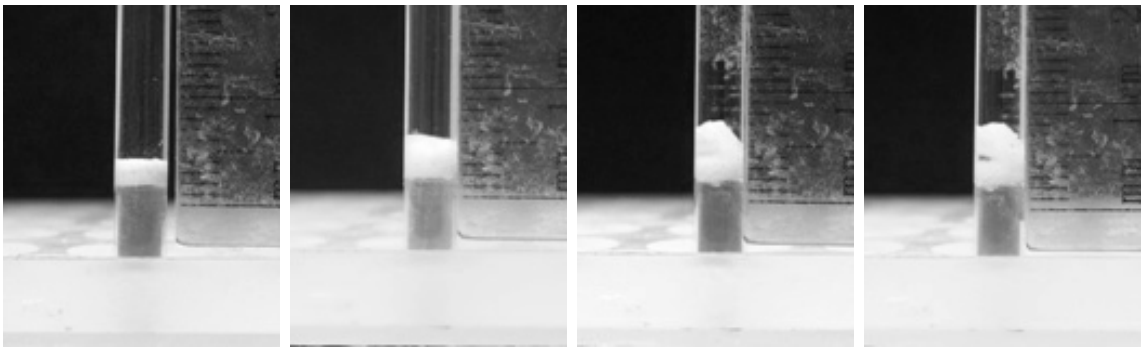

(a) $t = 1\,\mathrm{h}$ (b) $t = 12\,\mathrm{h}$ (c) $t = 2\,\mathrm{d}$ (d) $t = 4\,\mathrm{d}$

Figure 4.1: Types of morphological changes observed in a CPP disk. The disk is (a) initially cylindrical, then (b) begins to swell. At later times, (c) the swollen region may topple, and (d) in some cases bulk erosion is apparent near the disk center.

4.2 Results: Optical Photographs

This section presents the analysis of macroscopic changes that occur in CPP disks observed via the optical photographs. These changes include both bulk erosion and disk swelling, and Fig. 4.1 presents a series of photographs showing some important features of the disk morphology.

Immediately following immersion ($t \approx 0$), the disk is essentially a solid cylinder, and there is a small gap between the disk sides and the tube walls. The gelling disk begins to swell, and by $t = 1\,\mathrm{h}$ the disk sides generally form close contact with the tube wall. For a period following this, the disk continues swelling vertically, and mostly retains its cylindrical form. Eventually the form of the disk may change, with the top surface inclined due to uneven swelling.

After about 3 to 5 days, the disks appear to have two strata: one in approximately the original disk form, and a swollen layer on top. In some samples, bulk erosion may become apparent at certain times, seen as a "rupture" between the top and bottom layer (the layers actually separate). This rupture in the disk does not always persist; it may later collapse, bringing the two halves into contact once more. Even then, however, the photographs reveal that the layers remain distinct, and this may be due to a "shell" of non-swelling (possibly crystalline) material in the form of the original disk.

Disk ID	Rupture
G1-BAK-6.1	7 – 8, 13 days
G1-MRI-6.2	4 – 6 days
G1-MRI-6.6	-
G1-BAK-6.7	-
G1-MRI-6.10	6 – 9 days
G1-BAK-6.11	-

Disk ID	Rupture
G2-MRI-6.4	3 – 4, 6 days
G2-BAK-6.5	-
G2-MRI-6.8	3, 13 days
G2-BAK-6.9	3, 5, 11 – 13 days
G2-MRI-6.12	-
G2-BAK-6.13	-

Table 4.1: Timing of apparent bulk erosion in G1 (left) and G2 (right) samples

4.2.1 Bulk Erosion

Bulk erosion can occur in both G1- and G2-type disks alike, yet it does not appear to occur for every disk. Whether or not a disk shows evidence of rupture at a given time point was identified using the photographs and recorded in Table 4.1. Due to the 1-day sampling interval, these values are uncertain by ± 1 day. Additionally, it is possible that rupture events were not detected if they occurred entirely between experimental time points.

Although rupture is not observed for every disk, it seems to occur as frequently for G2 disks as for G1. The timing appears to be highly variable, although it seems to be more reproducible for G2 disks than for G1 disks (i.e. first occurrence is at approximately 3 days).

4.2.2 Swelling

Volume Estimation

One unique aspect of the NMR sample-tube geometry is that it allows for easier estimation of disk volume than in the elution apparatus used previously. Volumes of the disk were estimated at each time point by digital analysis of the photographs, and used to analyze swelling. The estimation was done using the following steps (illustrated in Fig. 4.2):

1. The disk region-of-interest (ROI) in the image was defined using an automated threshold-detection algorithm

2. The height profile was calculated using the ruler for scale

3. The volume was estimated based on the cylindrical geometry of the disks

(a) (b) (c)

Figure 4.2: Volume estimation: (a) starting from a photograph, (b) a profile of the disk is calculated, which is then (c) used to approximate the 3D shape of the disk.

The last step was done by assuming that the disk height is the same across the depth dimension (i.e. "into the page"). Because the samples were positioned specifically to depict the profile most clearly, this is likely to be a good assumption.

Volume plots for the individual samples are shown in Fig. 4.3(a). For the purpose of comparison, these have each been normalized by the initial disk volume. The average and standard deviation were also computed for the MRI and BAK samples separately (b) and for all samples together (c).

The plots of the n = 3 averages in Fig. 4.3(b) show that the G1 MRI and BAK curves essentially agree within the errorbars, but the G2 MRI and BAK curves mostly *do not* agree within uncertainty.

The apparent difference in swelling could be due to the difference in time spent on the orbital lab shaker, which might have affected the kinetics of the system. Agitation of the buffer would be expected to increase the amount of water available to the CPP, which would then be expected to promote more rapid swelling. Also, samples that spend time away from the shaker may have a chance to settle slightly. Both of these factors may explain why the G2-BAK samples seems to swell more rapidly than the G2-MRI samples. The effect may also occur in the G1 disks, but may be obscured by the larger inter-sample variation of this disk type.

Swelling Transition

From the plots of disk volumes (particularly the average volume), swelling appears to be most rapid in the first few days post-immersion, and then slows to a more

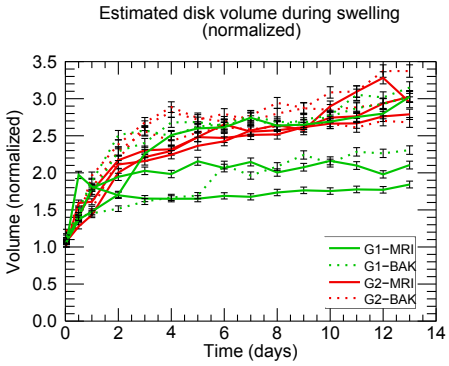

(a) Individual samples

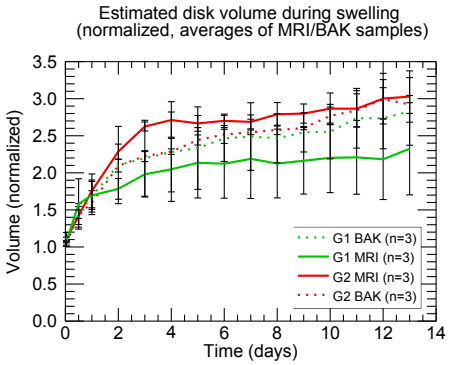

(b) The n=3 averages

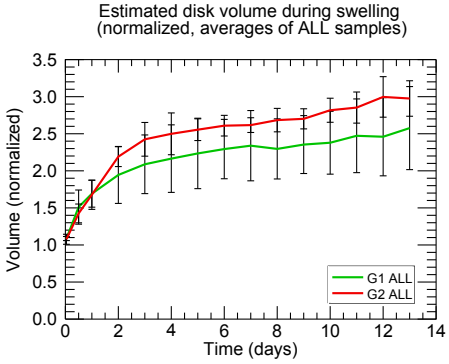

(c) The n=6 averages

Figure 4.3: Plots of the volume of the swelling disks, for (a) the individual samples and for (b) the $n = 3$ and (c) the $n = 6$ averages. Solid lines represent data from MRI samples and dotted lines represent data from BAK samples, except in (c) , where the solid line represents ALL samples. The line colour represents the disk type, either G1 (green) or G2 (red).

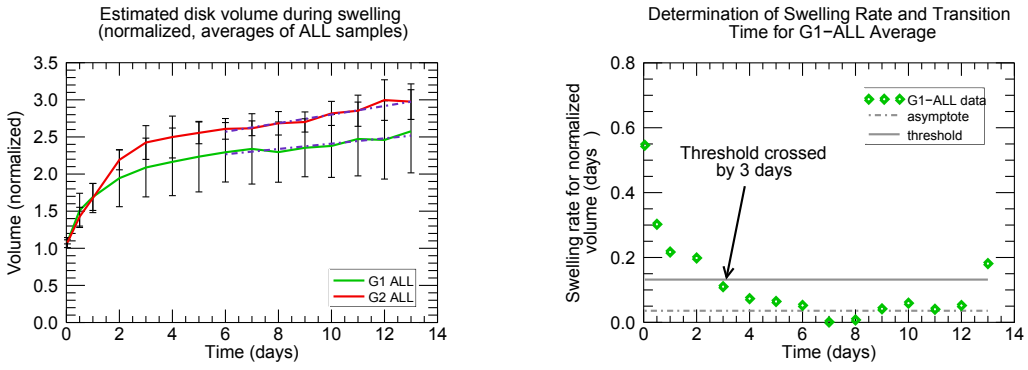

(a) (b)

Figure 4.4: (a) The normalized G1-ALL (green) and G2-ALL (red) swelling data were fit to a linear model over the period from 7 – 13 days to determine the late-time swelling rates. (b) An example of determining the swelling transition time using the derivative of the G1-ALL volume curve (green diamonds). The transition time is selected as the first point that crosses the threshold level (solid gray line) on its approach to the asymptotic swelling rate (dashed gray line).

moderate rate for the remainder of the experiment. Since swelling is a common controlling mechanism for drug release rates, this suggests looking at physical changes and release rates in stages, where different mechanisms may dominate at the various stages.

To define stages, it is necessary to determine the transition point between early and later-time swelling. The transition is not an abrupt one, and was therefore identified using a threshold method to determine when the swelling rate approached sufficiently close to its asymptotic value. The swelling curves for the $n = 6$ average were used to estimate the average late-time swelling rates (see Fig. 4.4(a)). Then, a threshold rate value was defined using the G2-ALL volume curve, chosen because it shows a distinct transition point at $t = 3\,\mathrm{d}$. The volume curves for all of the samples were differentiated using a 3-point Lagrangian interpolation method and compared to the threshold value to estimate the swelling transition time. Figure 4.4(b) shows the G1-ALL swelling rate curve as an example for determining the transition time.

The approximate swelling transition times are given in Table 4.2.2, which includes both the averages and the individual samples.

Disk ID	Transition (days)
G1-ALL	3
G1-MRI	3
G1-BAK	3
G1-BAK-6.1	1
G1-MRI-6.2	5
G2-MRI-6.4	1
G2-BAK-6.5	3
G1-MRI-6.6	2
G1-BAK-6.7	5

Disk ID	Transition (days)
G2-ALL	3
G2-MRI	3
G2-BAK	4
G2-MRI-6.8	3
G2-BAK-6.9	3
G1-MRI-6.10	3
G1-BAK-6.11	4
G2-MRI-6.12	3
G2-BAK-6.13	4

Table 4.2: Transition times for the G1 and G2 swelling data, including both the averages and the individual samples.

Comparison of Swelling in G1/G2 Disks

With regards to the swelling transition, on *average* it tends to occur at about 3 days for both G1 and G2 disks. This shows that, despite differences in initial volume and material processing, the two kinds of CPP materials tend to cease their initial swelling period at roughly the same time. Notable exceptions are samples 6.6 (G1-MRI) and 6.1 (G1-BAK). The swelling curve for sample 6.6 is anomalous, rising rapidly in the first 12 hours, then undergoing no further swelling. The curve for sample 6.1 more closely resembles the other curves, but simply undergoes very little swelling over the first few days.

Referring back to the normalized G1-ALL and G2-ALL volume curves in Fig. 4.3(c), the average swelling in G2 disks is greater than in G1 disks, although the uncertainties are large, and it would appear that the difference is not significant.

The G2 disks tend to swell slightly more than G1 disks in the initial time period (although the difference is not significant within uncertainty). The greater fractional volume increase may be attributable to the fact that, initially, the G2 disks are denser. Alternatively, it may be that the shorter CPP chains (in G2 disks) slide past one another with greater ease, offering less resistance to disk expansion.

4.3 Results: Fluid Distribution Using Spin-Density Maps

The averages of the spin-density maps were calculated separately for the G1 and G2 samples at every time point. The entire set of these maps is presented in Fig. 4.5, and

while this data set is relatively large and complicated, the remainder of this section will focus on and clarify specific aspects.

4.3.1 Spin-Density Maps

In the series of spin-density maps, the position along the axis of the disk (z) is shown on the horizontal axis, with the disk bottom located at $z = 0.0\,\text{mm}$. The intensity of the MRI signal is shown on the vertical axis, which represents the relative saturation of water. The term "relative saturation" means the fractional concentration of buffer relative to the bulk, where 0% represents the absence of water and 100% represents pure buffer. In other words, it shows the distribution of the buffer fluid in the disk. The maps are colour-coded according to the legend on the right, which identifies the measurement time point. Also, the average initial height of the disks is indicated by the gray, dashed line, and the horizontal axis has been cropped at 4 mm to highlight the region occupied by the disks.

The maps show, as expected, that the relative saturation in the buffer region above the disk is nearly 100%, and that it is lower within the disk.

At the first time point ($t = 1\,\text{h}$), water can be seen to be distributed everywhere throughout the disk. In both G1 and G2 disks, there is a relatively low, uniform distribution of fluid near the disk center, with greater relative saturation toward the disk bottom and toward the disk top. The higher saturation near $z = 0$ is due to water that enters the disk through the bottom shortly after immersion. Although the disks are cemented to the spacers, water can penetrate into spaces left by irregularities on the disk surface. Shortly following immersion, the disks swell rapidly and effectively seal-off the sides of the test tube. It is most likely, then, that water is absorbed through the disk bottom at early times, before this has happened.

At later times, fluid continues to penetrate into the disks. Over the first few days, there appears to be a "front" of fluid that propagates from the top of the disk towards the bottom.

At $t = 1\,\text{h}$, the fluid density maps show slight differences in the relative saturation near the centers of the disks (i.e. at half the original height). The values of the curves at these positions are about 9% for G1 disks and 6% for G2 disks. This is likely because the G2 disks are more dense, due to the compaction step in the G2 process,

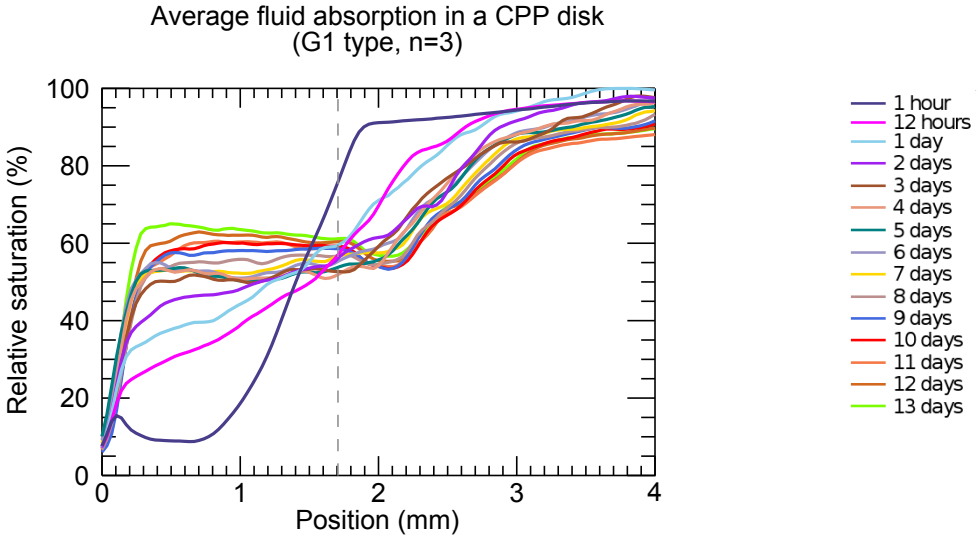

(a)

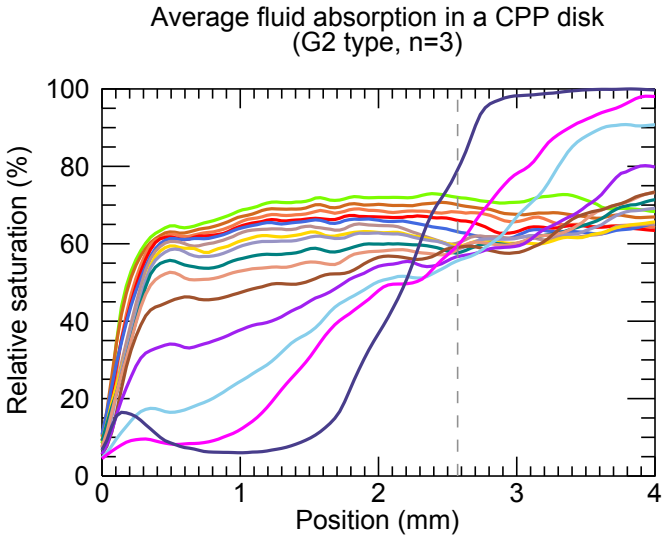

(b)

Figure 4.5: The average spin-density maps for (a) G1 and (b) G2 disks. The time point is indicated by the line colour according to the legend (top right). The dashed, vertical lines indicate the average initial height of the disks.

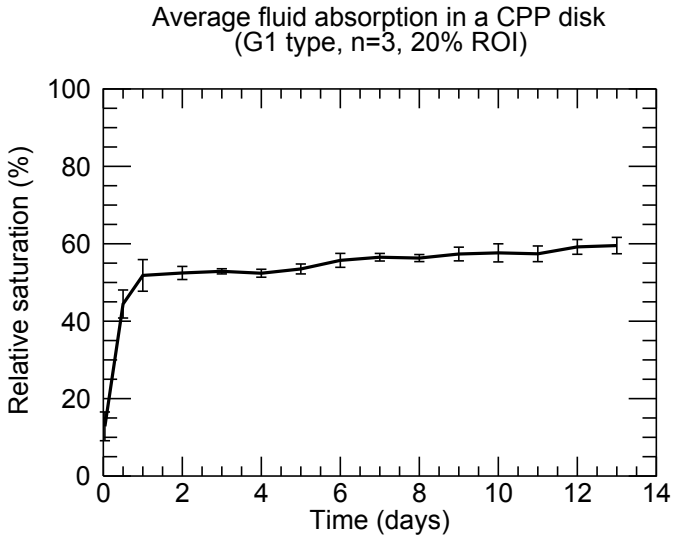

(a)

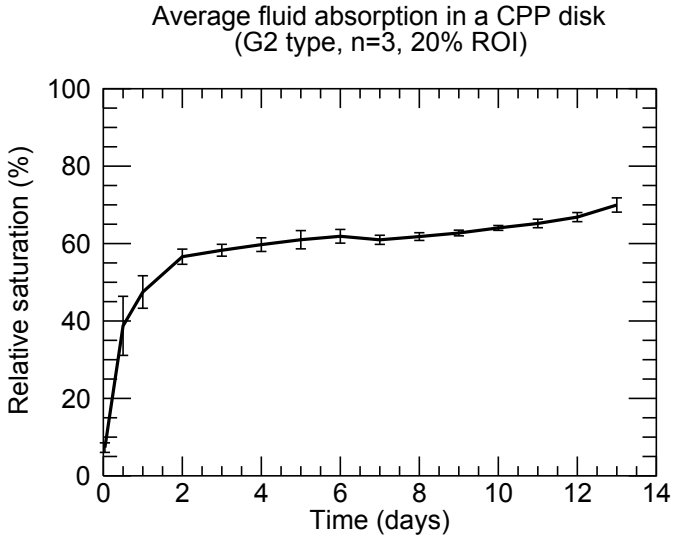

(b)

Figure 4.6: The spin-density in the ROI for (a) G1 and (b) G2 disks. The error-bars represent the standard deviation in the relative saturation across the ROI (not uncertainties)

which greatly reduces the porosity.

Another difference is apparent by considering the *time series* of the spin density profiles. In the G1 disks, the fluid front propagates rapidly from the top of the disk, reaching the bottom by 12 h. In G2 disks, this mode of fluid absorption takes longer, with the front seeming to reach the disk bottom only by 1 – 2 d.

After a certain time, the spin density profiles appear to be nearly level throughout the disks, and the further increases in spin density occur essentially uniformly.

4.3.2 Region-of-Interest Analysis

The results of the ROI analysis for spin-density are shown in Fig. 4.6. Recall that the curves here represent an average across the middle 20% of the disk height, and the errorbars represent the standard deviation in the relative saturation across the ROI.

The time course plots of the ROI show that there is slightly more water in the G1 disks at $t = 1$ h, but that the relative saturation of both G1 and G2 disks increases at similar initial rates. In the G1 disks, this rapid initial absorption continues until $t = 1$ d, and slows appreciably thereafter. The G2 disks are different in that the rapid initial rate appears to continue until $t = 2$ d. In both disk types, the relative saturation has an increasing trend throughout the remaining time in the experiment. The final saturation level on average is about 60% for G1 disks and 70% for G2 disks.

4.4 Results: Molecular Tumbling Mobility Using the T_1 Maps

4.4.1 T_1 Maps

The series of averaged T_1 maps are shown in Fig. 4.7. These (and all other parameter maps) are similar in some ways to the spin density maps. Again, the position along the axis of the disk (z) is shown on the horizontal axis, the dashed line indicates the original disk height, and the colour code indicates the time point. The differences arise mainly from depicting the biexponential signal behaviour. Firstly, the T_1 plots contain two components: the T_{1a} component (solid lines) and the T_{1b} component (dotted lines), where $T_{1a} > T_{1b}$. In addition, a second plot below each T_1 map shows the amplitude of each component, which is the signal weighting of that

component. If the physical free- and bound-water components were non-exchanging (or in the slow exchange regime), the amplitudes would show both the distribution of water *and* accurate, relative proportions of the free and bound water components. In general, it cannot be assumed that exchange is slow; nonetheless, *changes* in the signal amplitudes still reflect changes in the proportion of free/bound water.

Evidently, the biexponential plots are visually complex. They are shown here for completeness and to discuss some qualitative features, but additional analysis will be done using reduced subsets of these data (i.e. single time points or ROI analysis). Before further analysis, however, we first discuss general characteristics in the interpretation of the T_{1a} and T_{1b} components in the context of exchange.

Consider, for example, the T_1 map for G1 disks at $t = 1\,\mathrm{h}$ (Fig. 4.7(a), dark blue line). The region above the disk (to the right of the black dashed line in the plot) has a single T_1 component, and both the T_1 ($\approx 3200\,\mathrm{ms}$) and its amplitude are essentially uniform. This region contains only buffer, so this T_1 component represents *truly* free water.

In the region within the disk (left of the black dashed line), there is an additional T_1 component: the signal is biexponential here. The fact that T_{1b} ($\approx 300\,\mathrm{ms}$) is lower than the T_1 of free water reveals a difference in the molecular tumbling correlation times. Since water is known to hydrate CPP chains, we infer that the T_{1b} component appears to be the contribution of the "bound" hydrate water to the signal.

In interpreting these observations, it is not correct to draw an equality between bound water and the T_{1b} component, because there may be exchange between the different water components present. Nonetheless, the T_{1a} is similar to the T_1 of free buffer, which suggests that there also exists a relatively free water component within the disk (possibly located in pore spaces or diffusing freely amongst the CPP chains). Moreover, the fact that (on average) the T_{1a} component in the disk is lower than the T_1 of the free buffer suggests strongly that there is exchange between "free" and "bound" water within CPP that is not slow compared to T_1.

Considering now the T_1 map for G2 disks at the same 1 hour timepoint (Fig. 4.7(b), dark blue line), a major difference is apparent. Like the G1 disks, there are both T_{1a} and T_{1b} components, but they coexist only in a narrow region near the top of the G2 disks. Deeper within the disk ($z < 2\,\mathrm{mm}$), only the T_{1b} component is

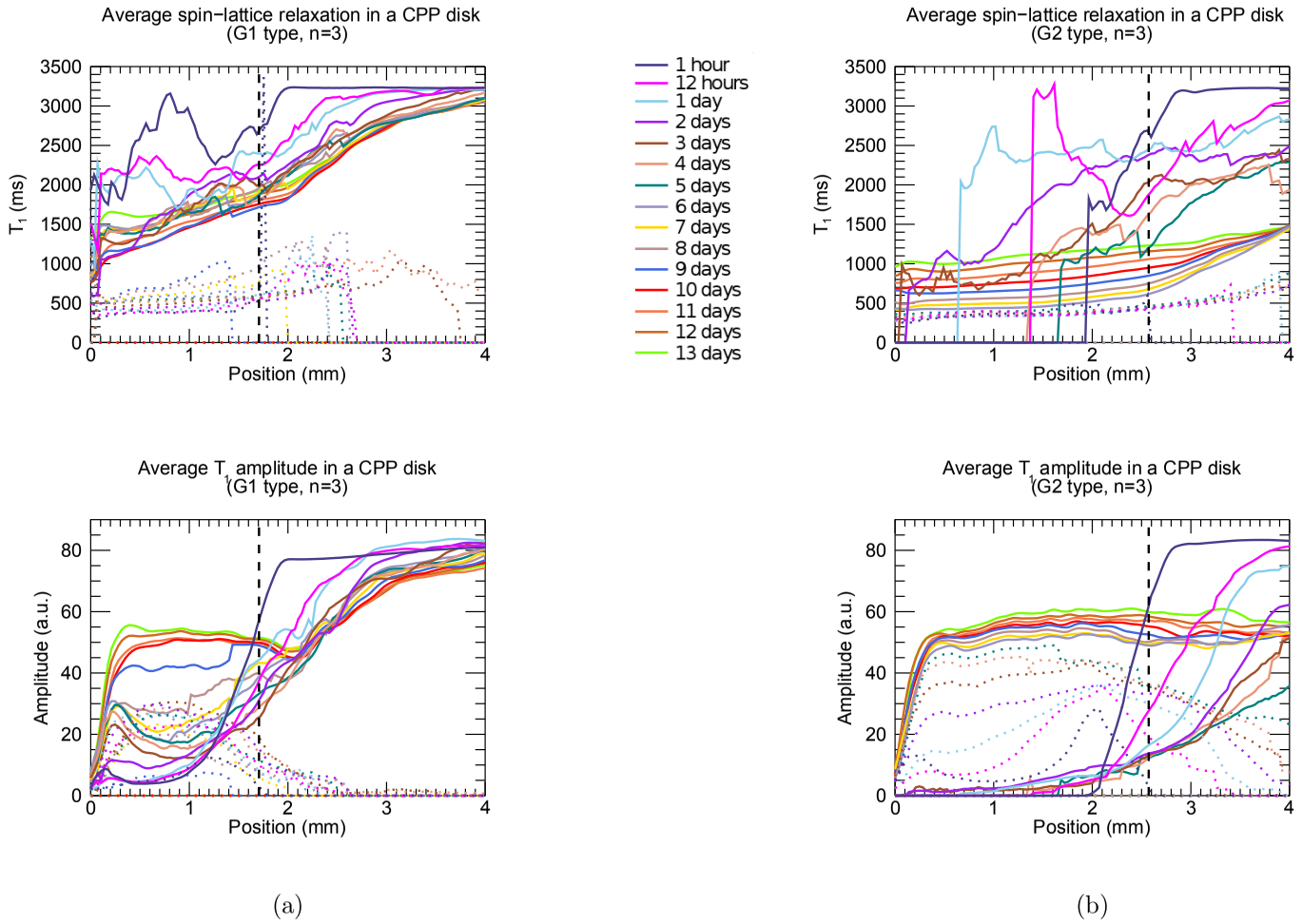

(a) (b)

Figure 4.7: The average T_1 maps (parameters and amplitudes) for (a) G1 and (b) G2 disks. The time point is indicated by the line colour according to the legend (top center), and the components most closely associated with "free"/"bound" water are indicated with solid/dotted lines, respectively. The dashed, vertical lines indicate the average initial height of the disks.

apparent. This could be interpreted in two ways: one is that there may be no "free" water component present in this region. Alternatively (and more likely), there exists a free water component, but it is in fast exchange with the bound water. The reason why this scenario is more likely will be discussed in the following section concerning the time evolution in the ROI.

4.4.2 Region-of-Interest Analysis

To describe trends in the time evolution of T_1, we now consider an ROI analysis of the T_1 maps (see Fig. 4.8). Just like the maps in the previous section, these plots contain both T_{1a} and T_{1b} components, although here they are distinguished by colour (red and blue, respectively).

As seen previously in the T_1 maps, there are T_{1a} and T_{1b} components within the G1 disks at the $t = 1\,\mathrm{h}$ time point, but only a T_{1b} component in the G2 disks. On average, the T_{1a} component in G1 is very close to that of free water. As discussed in the section on spin-density maps, this could be the result of the initial porosity of the G1 disks, which would contain effectively free buffer. In G2 disks, which have undergone a compaction step and contain very little porosity, this component is not present at all.

Changes in the T_1 components are apparent beginning at the very next time point ($t = 12\,\mathrm{h}$). For G1 disks, there is a notable drop in T_{1a}. This could be due to gelling of the CPP, which may cause collapse of the pores. Nonetheless, the T_{1a} component remains, and grows in amplitude as the disk absorbs additional buffer. At this same time point, a T_{1a} component seems to emerge in the G2 ROI. This underscores the need to refer back to the maps for more elaborate interpretation: doing so reveals that the origin of this behaviour is a T_{1a} component that forms near the top of the disk and propagates downward, reaching the bottom by $t = 3\,\mathrm{d}$.

Subsequent to the initial two time points, the T_{1a} component in the G1 disks drops very gradually over the following days, while the amplitude of this component rises. Eventually, the T_{1a} profile appears to stabilize, although the amplitude continues rising. The growing amplitude is expected, due to the continued absorption of buffer. However, the T_{1b} amplitude decreases until it vanishes at $t = 9\,\mathrm{d}$, while at the same time, the T_{1b} increases (particularly between 5 to 9 days). Taken together, these

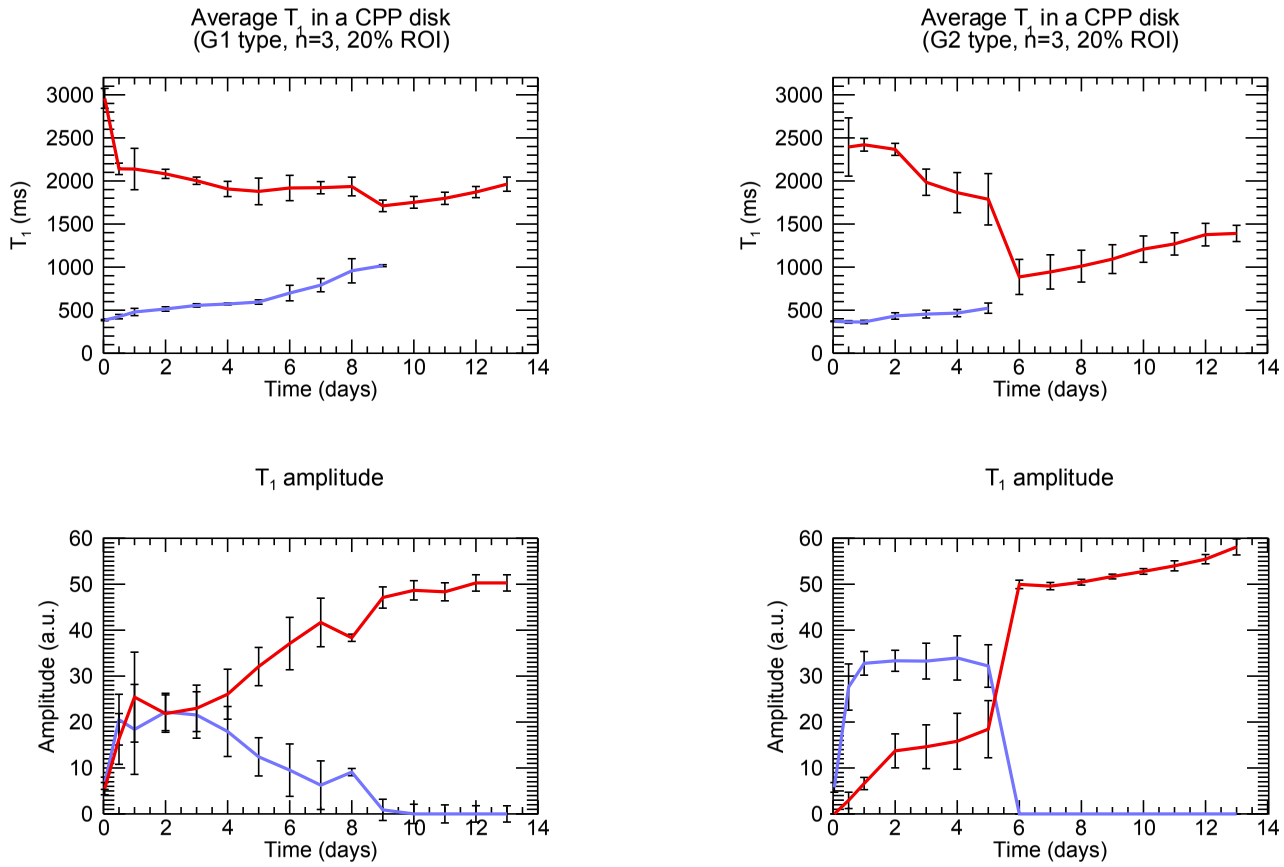

(a) (b)

Figure 4.8: The average T_1 in the ROI for (a) G1 and (b) G2 disks. The red and blue lines represent the components most closely associated with "free" and "bound" water, respectively.

two observations suggest the exchange characteristics are changing during this time period. As the disk swells and more space is made available for free water, the T_{1a} amplitude grows. Correspondingly, exchange with an increasing free-water pool causes T_{1b} to become weighted towards the free-water relaxation time (i.e. to increase).

From the ROI analysis, it would appear that the T_{1a} component that formed in the G2 disks grows in amplitude. However, from the maps it can be seen that the T_{1a} component vanishes at points below the original height of the disk, and the major contributor to the T_{1a} amplitude is free water in the layer *above* the original disks height. This reveals important differences between the CPP material in the top (swollen) and bottom layers. Specifically, the swollen gel layer appears to contain a much greater T_{1a} amplitude, possibly suggesting a greater amount of free water on average.

While the T_1 in the G2 base layer is essentially monoexponential, the effects of exchange can nonetheless be seen. As in the G1 disks, the T_{1b} component here rises between 1 hour to 5 days, which is a likely indicator that there is a second (free water) component present that is not detectable on its own due to rapid exchange with the bound water component. As more water is absorbed, the monoexponential T_1 becomes increasingly weighted toward the free-water component, and hence the T_1 increases.

There is a point in each of the G1 and G2 ROIs where the T_1 appears to become a single component (10 days for G1; 6 days for G2). This happens because the disks ultimately become so heterogeneous that, although relaxation in each voxel is not monoexponential, there is neither spatial continuity of components nor convergence on a biexponential solution. In this regime, the T_1 measurement is no longer able to resolve distinct T_{1a} and T_{1b} components.

A comparison of the T_1 and spin-density results is of interest. Recall that the relative saturation in the disks grows rapidly in the early time points ($0 - 1\,\mathrm{d}$ for G1; $0 - 2\,\mathrm{d}$ for G2). Afterwards, fluid continues to be absorbed, but at a much reduced rate. Conversely, appreciable changes in the T_1 data continue throughout the experimental period, even at later times. This implies microstructure changes that require just the presence of water, not the absorption of additional water, and may be due to scission reaction of chains or some other reorganization of the microstructure.

4.5 Results: Molecular Tumbling at Shorter Time Scales Using the T_2 Maps

Although T_1 and T_2 are both sensitive to molecular motion (albeit at different frequencies), T_2 can often provide better resolution of biexponential components in systems characterized by exchange. This quality arises due to the fact that T_2 is frequently much shorter than T_1, which allows components to be observed in a regime in which exchange is slower compared to the relaxation time constant.

4.5.1 T_2 Maps

The series of averaged T_2 maps are shown in Fig. 4.9. The format of these plots is exactly the same as the T_1 maps from the previous section. As expected, many of the features of these maps qualitatively resemble those of the T_1 maps. In the pure buffer, the T_2 is monoexponential, and has a value very close to that of T_1 ($\approx 3000\,\text{ms}$). Within the CPP, again the relaxation times are generally biexponential; however, their time constant values differ drastically from T_1. For comparison, in G1 disks at $t = 1\,\text{h}$, the T_1 components are approximately $[T_{1a}, T_{1b}] \approx [2000\,\text{ms}, 300\,\text{ms}]$, while the T_2 components are $[T_{2a},\ T_{2b}] \approx [400\,\text{ms},\ 6\,\text{ms}]$. Because of the wider dynamic range of the T_2 parameter, the T_{2b} component is too small to be easily seen in Fig. 4.9. To better depict this component, the T_2 maps are reproduced in Fig. 4.10 with a narrower range on the ordinate (T_2) axis.

Like the T_{1b} component, the T_{2b} component is highly uniform over the extent of the disk, and is present because of the signal contribution of the "bound" water component. Like the T_{1a} component, the T_{2a} component varies over the extent of the disk and indicates contribution from a "free" water pool in exchange with the bound water. Moreover, the variation of T_{2a} across the extent of the disk indicates a spatially-varying microstructure that affects the local exchange characteristics. In the G2 disks, the T_2 relaxation within the original disk height is monoexponential at first, but again, the amplitude plots (shown back in Fig. 4.9) show a T_{2a} component that forms near the surface of the disk (1 h) and propagates toward the bottom of the disk.

By the 2-day timepoint, there is a T_{2a} component throughout both G2 and G1

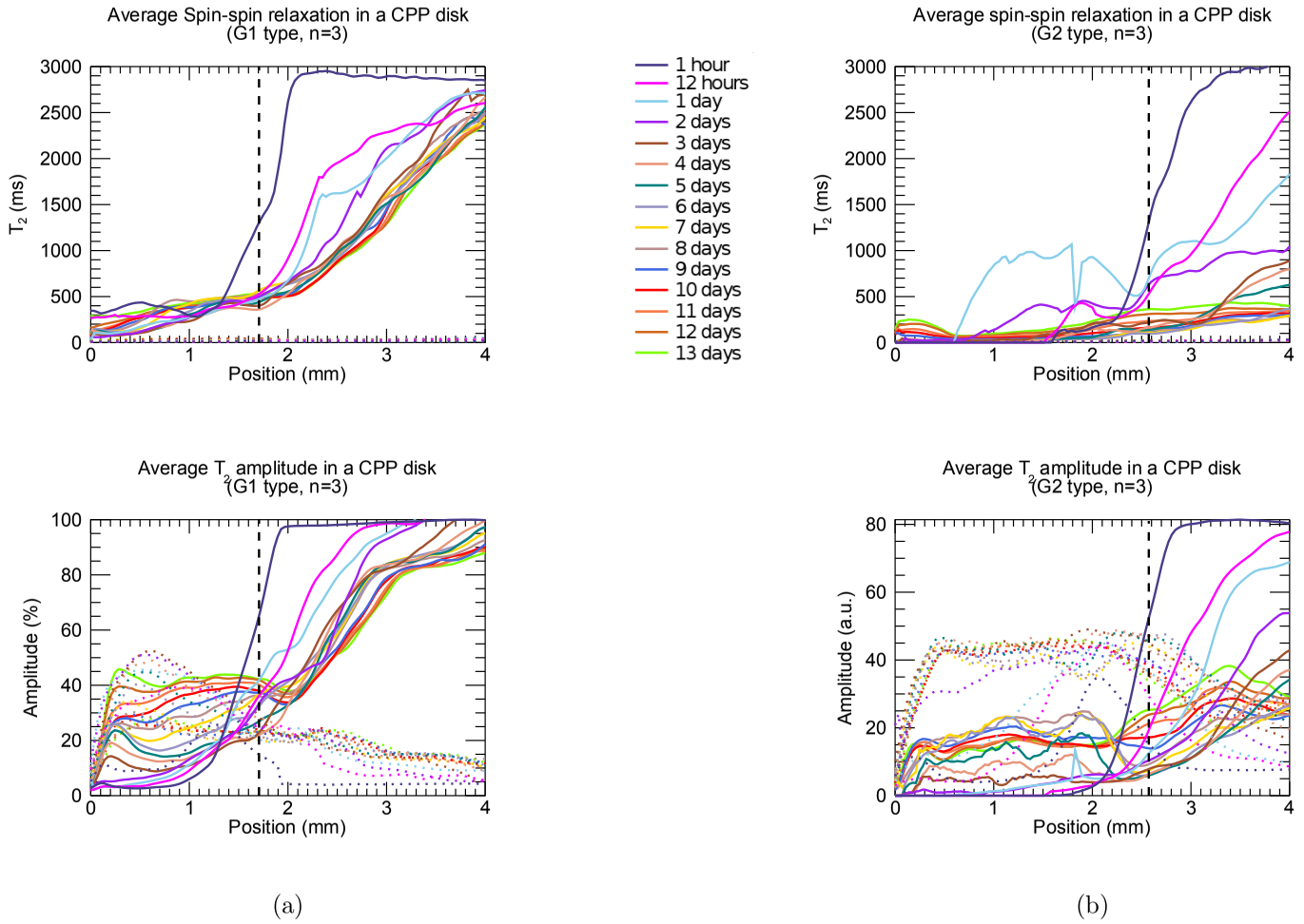

(a) (b)

Figure 4.9: The average T_2 maps (parameters and amplitudes) for (a) G1 and (b) G2 disks. The time point is indicated by the line colour according to the legend (top center), and the components most closely associated with "free"/"bound" water are indicated with solid/dotted lines, respectively. The dashed, vertical lines indicate the average initial height of the disks.

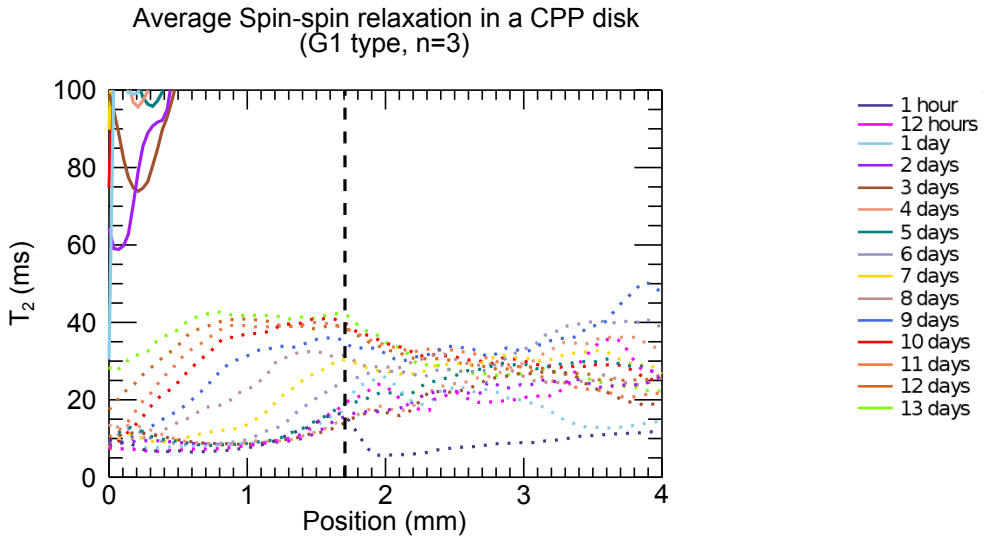

(a)

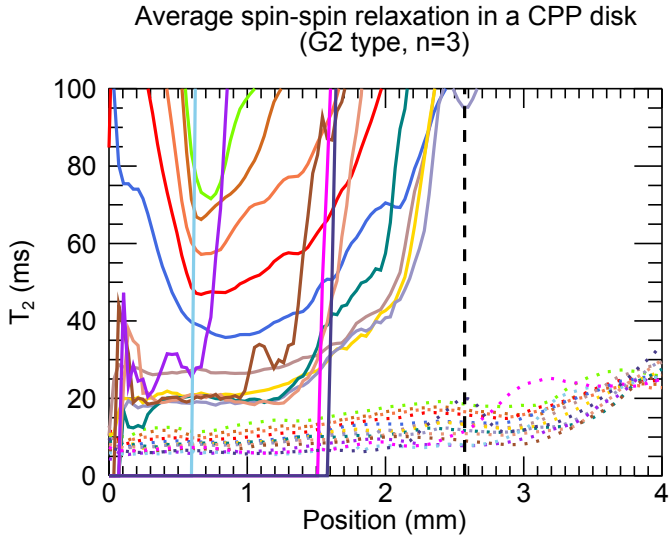

(b)

Figure 4.10: The average T_2 maps for (a) G1 and (a) G2 disks from Fig. 4.9, shown again here with an ordinate axis from 0 – 100 ms to better depict the short T_{2b} component. The amplitude maps from Fig. 4.9 adequately depict both components, and are therefore not reproduced here.

disks. At all time points after this one, the relaxation is characteristically biexponential, and there is never a point where the two components "collapse" again. As anticipated, this is due to the shorter time scale of the T_2 measurements, which allows better resolution of exchanging components and definitively shows that there exist two exchanging water components at later times.

4.5.2 Region-of-Interest Analysis

As before with the T_1 data, we now consider an ROI analysis of the T_2 maps, shown in Fig. 4.11.

To summarize the results in the T_2 ROI plots, it appears that there is a free-water component at every time point, with the exception of $t = 1\,\mathrm{h}$ in the G2 disks. Again, it can be seen from the maps that this G2-T_{2a} component actually starts near the disk top and propagates toward the bottom, only reaching there by 2 d. At early times in both disk types, both the T_{2a} and T_{2b} amplitudes rise, as expected due to water absorption. Afterwards, from $t = 4\,\mathrm{d}$, the T_{2a} amplitude increases. Correspondingly, the T_{2b} component increases as well. This result makes sense in the context of exchange, where the increasing T_{2a} amplitude weights the relaxation times more toward the free water component. The T_1 data hinted at this mechanism for the changing relaxation times later in the experiment, but the ability of the T_2 measurement to resolve the components makes this explicit.

A point of special interest is the appearance of the T_{2a} component throughout the G2 disks at $t = 2\,\mathrm{d}$ (see Fig. 4.10(b)). With the T_{2a} associated closely with the free water component, the appearance of this component is potentially important when considering drug transport. At the point it first appears and over the next few days, the T_{2a} is very close in magnitude to T_{2b} ($[T_{2a}, T_{2b}] \approx [20\,\mathrm{ms}, 10\,\mathrm{ms}]$). This implies that the free and bound water components are toward the rapid end of the intermediate exchange regime (because there are two distinct components, but they are very similar). Furthermore, it suggests that the free water component may actually be physically present at *all* times in the G2 disks, even at earlier times. The T_2 measurement can discriminate the two components only when the increased amount of absorbed water and microstructural degradation is such that the system is no longer in fast exchange.

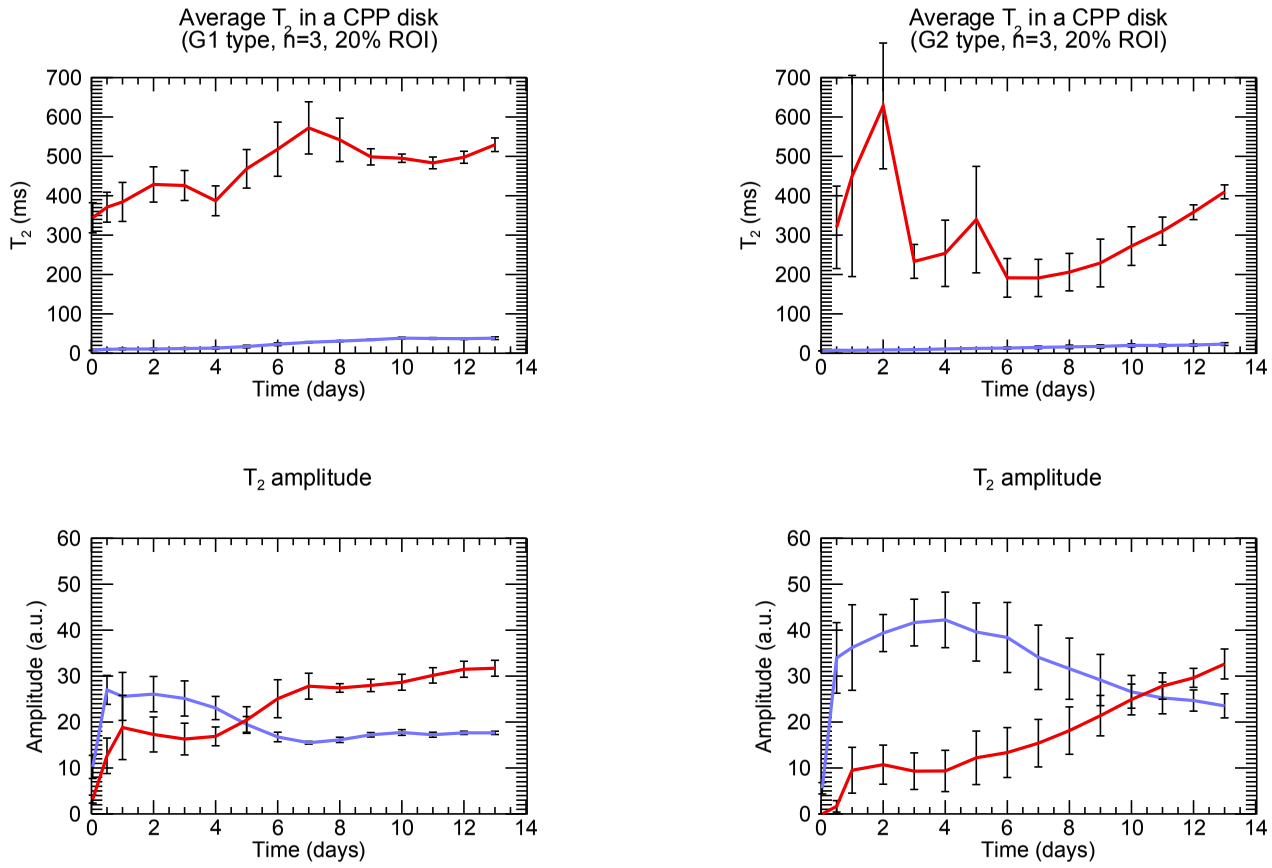

(a) (b)

Figure 4.11: The average T_2 in the ROI for (a) G1 and (b) G2 disks. The red and blue lines represent the components most closely associated with "free" and "bound" water, respectively.

This aspect of the degradation is not apparent in the G1 disks. Because they have not been subject to a compaction step, the microstructure incorporates sufficient free water at all stages to produce a distinct T_{2a} signal component from the very start. The G2 disks show that a distinct free water component can emerge at later stages, due to the swelling/degradation caused by the interaction with water.

4.6 Results: Molecular Translation at Micron Length Scales Using the ADC Maps

The discussion now turns to the measurements of the apparent diffusion coefficient of water in CPP. In some ways, this is a departure from the T_2 and T_1 results presented in the previous two sections. One reason is that the relaxation times are both *indirect* probes of molecular mobility in different frequency regimes. They are sensitive to the rate of molecular tumbling, but do not provide a quantitative physical description of that motion. The measurement of the apparent diffusion coefficient is different in that it provides a direct and quantitative measure of the random translational motions of molecules, and any microstructure-induced restrictions to such motion.

Another way that the diffusion measurement differs is in the interpretation of the exchange regime. The T_1 and T_2 parameters *inherently* define the time characteristics of the signal, and therefore provide the timescale that determines the exchange regime. For pulsed-gradient diffusion measurements, the evolution time of the signal is a combination of Δ and δ, and so it is these parameters that determine the time scale over which exchange is important in the system. Furthermore, the diffusion exponent (see equation 2.84) depends on different powers of Δ and δ, and thus the timescale depends on the specific choice of measurement parameters in a way that the relaxation times do not.

For the PGSTE sequence, the time $\Delta + 2\delta$ could be called the "effective signal evolution time". Since δ is relatively small, and $\Delta = 250\,\text{ms}$, this is the approximate timescale for exchange. Because $T_1 > 400\,\text{ms}$ and $T_2 > 6\,\text{ms}$, the diffusion exchange timescale can be said to lie between these two, and is roughly the same order as the T_1 timescale. It is expected, then, that the diffusion measurement should be similar to T_1 in its ability to resolve biexponential components (if not slightly better).

4.6.1 ADC Maps

The series of averaged ADC maps are shown in Fig. 4.12, and are formatted in the same way as the T_1 and T_2 maps previously. Because the diffusion coefficient of water is a known quantity, it is expected that the pure buffer region should contain a single component with $D = 2.0 \times 10^{-5}\,\mathrm{cm}^2/\mathrm{s}$. This is basically what is observed in the region just above the disk, although there appears to be a region of unexpectedly high D in some of the early time points (to be discussed below). Within the disk itself, the diffusion signal is generally biexponential, although interpretation of this set of maps requires particular attention to the component amplitudes. There are times/regions in which the ADC maps may show two components, but the amplitude of one may be so small as to be nearly negligible. Additionally, there are many times when only a single component appears within the disk. At these time, whether the component is classified as D_a or D_b depends on the continuity with adjacent regions.

Because the ADC is a quantitative measure of average molecular displacements, it is possible to estimate the distance scale of molecular motions, given the components observed in the system. The expression for the one-dimensional[†] root-mean-squared displacement, given a diffusion coefficient D is

$$\ell_{\mathrm{rms}} = \sqrt{2\,D\,t}, \tag{4.1}$$

where t is the diffusion time ($\approx \Delta = 250\,\mathrm{ms}$). The two diffusion coefficients differ, but have approximate values

$$D_a = 2.0 \times 10^{-5}\,\mathrm{cm}^2/\mathrm{s}\ \text{(long component)} \quad \text{and} \quad D_b = 2.0 \times 10^{-6}\,\mathrm{cm}^2/\mathrm{s}\ \text{(short component)}.$$

The associated diffusion length scales in 1-D are thus

$$\ell_a = 32\,\mu\mathrm{m} \quad \text{and} \quad \ell_b = 10\,\mu\mathrm{m}.$$

An important observation from the ADC maps is that, in regions of the disk where the D_a component exists, its value is close to the self-diffusion coefficient of free water. This lends support to the interpretation that the corresponding relaxation

[†]The expression is given for one-dimensional diffusion, because the MRI techniques measure only in one direction

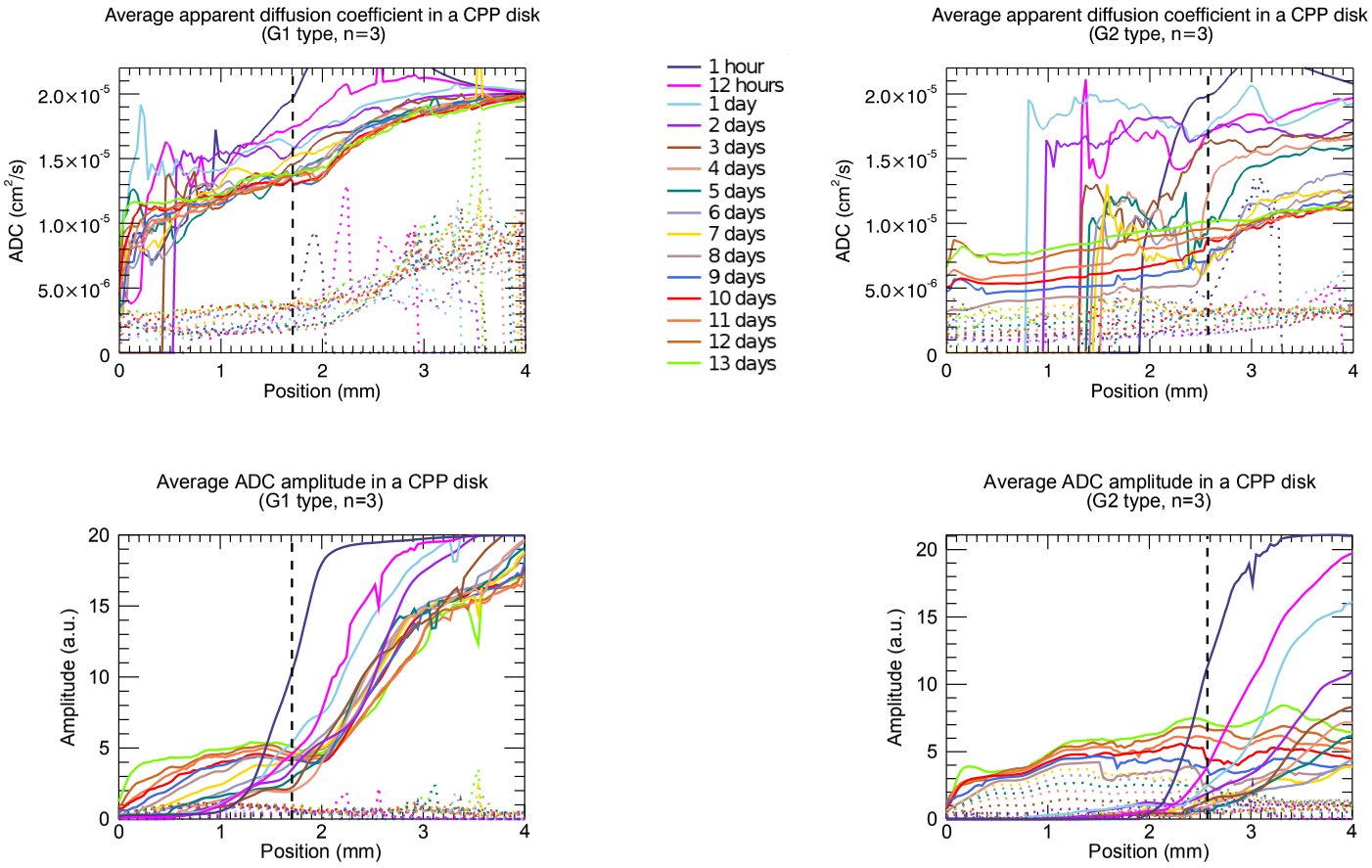

(a) (b)

Figure 4.12: The average ADC maps (parameters and amplitudes) for (a) G1 and (b) G2 disks. The time point is indicated by the line colour according to the legend (top middle), and the components most closely associated with "free"/"bound" water are indicated with solid/dotted lines, respectively. The dashed, vertical lines indicate the average initial height of the disks.

time components (T_{1a} and T_{2a}) are closely associated with free water (in exchange with bound water), because it shows that both the molecular tumbling mobility *and* the rate of translational diffusion are comparable to free water.

4.6.2 Region-of-Interest Analysis

The ROI analysis of the ADC maps is shown in Fig. 4.13.

The G1 disks are characterized by a D_a component that is largely invariant with time. The D_b component also changes very little until $t = 4\,\mathrm{d}$ when it begins increasing, and ends at a value nearly $2\times$ its starting value (with very little change after 7 days). The amplitude plots show that the overall D_a and D_b signal amplitude start out very low. Over time, both amplitudes increase—the D_b amplitude reaches its maximum by day 2, while the D_a amplitude exhibits an increasing trend throughout the remainder of the experiment.

On average, the G2 disks show very similar characteristics to G1 disks in terms of D. The D_a in G2 disks appears to decrease over time, but reaches a lower value than in G1 disks. The D_b increases, and at later times it reaches the same value in both G1 and G2 disks. The D amplitudes show roughly the same trends in both disk types as well. Despite a period during which the D_b amplitude in G2 disks becomes appreciably larger than in G1 disks, at 13 days it has nearly the same value in both disk types.

While there are similarities between G1 and G2 disks averaged over the ROI, some aspects of the time-evolved behaviour are only apparent in the maps (Fig. 4.12). For example, at times $t > 4\,\mathrm{d}$, the region below the original disk height is generally biexponential for G1 disks and monoexponential for G2 disks. For G1 disks at times after 4 days, the D_a component in this region ($z < 1.7\,\mathrm{mm}$) changes very little, although its amplitude increases. This suggests that degradation of the disk leads to an increasing fraction of free water, but with no increase in the apparent RMS diffusion length (as measured at this diffusion time).

In the G2 disks, the monoexponential D in this region ($z < 2.6\,\mathrm{mm}$) increases with time; however, the fact that the T_2 maps resolve two water components in this same region over these time points suggests that there are two water components present, but that exchange between them is fast on the time scale of the ADC measurement.

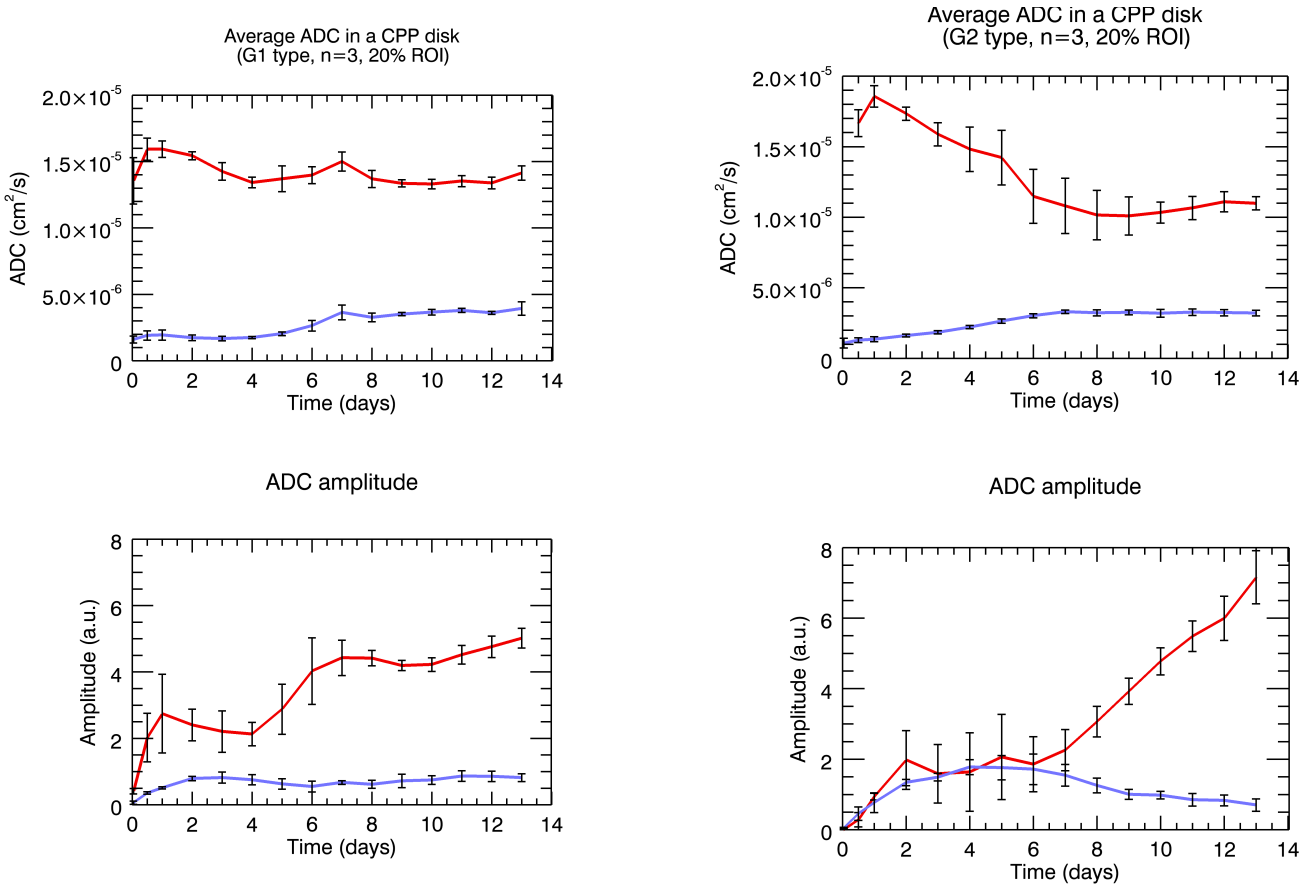

(a) (b)

Figure 4.13: The average ADC in the ROI for (a) G1 and (b) G2 disks. The red and blue lines represent the components most closely associated with "free" and "bound" water, respectively.

In this context, the increasing D in this region could be due to one (or more) of the following physical mechanisms:

- The microstructure changes in a way that increases the RMS diffusion distance of the free water component (e.g. a greater mean-free-path between interactions with chains);
- The RMS diffusion length of the bound water increases as well (this could happen because of increased mobility of chains as they become shorter through scission);
- The fraction of free water increases, weighting the exchange toward the faster-diffusing component.

The lack of distinct D_a/D_b components makes it impossible to determine which of these mechanisms produce the observed diffusion behaviour. However, the overall increase in D supports the idea that degradation leads to an increase in the local self-diffusion rate throughout this region in the G2 disks.

4.6.3 Relaxation Weighting

The echo time (TE) of a pulse sequence relative to the T_2 relaxation time is what determines the extent of T_2 weighting of the signal. A short TE is generally favourable, because it ensures that the measured parameter amplitudes are nearly proportional to the actual parameter amplitudes. Put another way, only in the limit

$$\frac{\mathrm{TE}}{T_2} \ll 1$$

do the measured amplitudes reflect the actual signal amplitudes[‡]. The exception is the T_2 measurement itself, where the nature of the CPMG measurement assures that the amplitudes are free from relaxation weighting.

In the PGSTE sequence, there is an additional weighting due to T_1 that occurs in the z-storage period between the pulsed-gradient lobes. As discussed in chapter 2 (MRI theory), this is intentional, because T_1 (longitudinal) relaxation is much slower

[‡]In general, this does not assure the actual amplitudes reflect the true populations of spins in the different microenvironments—for this, it is necessary to account for exchange.

than T_2 (transverse) relaxation, and this affords an increase in the Δ delay with less overall relaxation weighting. Nonetheless, only when

$$\frac{\Delta}{T_1} \ll 1$$

can the signal amplitudes be considered free of T_1 weighting as well.

Given the parameters used in the acquisition, the TE is 6.99 ms, and Δ is 250 ms. The b component has the shorter relaxation times, and will therefore be most strongly affected by relaxation weighting. The corresponding T_{1b} and T_{2b} are 6 ms and 250 ms, respectively. Because the delays and corresponding relaxation times are similar, this shows that the δ and Δ parameters also create delays that introduce appreciable relaxation weighting in the signal. The result is that the measured ADC amplitudes do not accurately reflect the signal amplitudes.

This effect can be seen clearly in the D_b amplitude in Fig. 4.13. In both disk types, the D_b amplitude is much less than that of the D_a amplitude. Compare this with the T_2 amplitudes in Fig. 4.11, where the T_{2b} component is the dominant signal component.

4.7 Physical Characterization: Summary of Results

An experiment was performed using MRI techniques and optical photography to characterize temporal and spatial changes in the physical structure of G1 and G2 disks. Generally speaking, the photographic results showed characteristics related to the size and shape of the disk, and the MRI showed the local fluid distribution and parameters related to microstructure and fluid mobility (T_1, T_2, and ADC).

At the beginning of the chapter, six factors were listed that are generally considered important for drug release materials. These include 1) diffusion, 2) swelling, 3) erosion, 4) geometry, as well as 5) drug characteristics and 6) drug/matrix interactions. The techniques used were not directly sensitive to the drug itself, but the MRI and photography provide information about the first four factors, and we return to those now in light of results from this chapter.

As a technique depicting the form of the disks, the factors of swelling, erosion, and geometry could all be described using the photographs. In particular, a technique for estimating the volume from photographs of the disks in profile was used to derive

swelling curves. These curves seemed to suggest that there are stages of rapid initial swelling and slower later swelling. The transition point between the two has potential significance for the drug release, possibly signaling a shift in the dominant mechanism of release.

Interior to the disk, processes of fluid absorption and microstructural degradation take place within CPP, which are detectable because of the non-destructive nature of MRI and its sensitivity to the diffusion and fluid transport characteristics of the sorbed water. While the spin-density maps reveal the fluid distribution, the biexponential relaxation and diffusion maps reveal an added level of detail: the existence (in general) of two signal components arising from "free" and "bound" water components in exchange. The T_2 is especially sensitive to the distinct components, and results suggest that the relative proportions of the free and bound water pools shift over the course of time. Comparing G1 and G2 disks, the T_2 signal components suggest that the proportion of free water is very small in G2 disks at first, but that this component increases with time. This difference may hold significance for the interpretation of dominant drug release mechanisms in each type.

Using the MRI technique that we developed, we were successful in characterizing structural changes internal to CPP materials over an extended swelling and degradation period. Because the method is able to resolve spatial and temporal changes in the microstructure, we can now use these results to analyze drug elution from CPP and interpret how the structure relates to release.

Chapter 5

Correlating Drug Elution with Physical Characteristics of CPP

The bulk drug release characteristics of gelled G1 disks and compacted-regelled G2 disks have previously been investigated in conventional bulk elution studies [7]. This approach is useful for evaluating the effects of different processing steps and optimizing the parameters used in fabrication. Furthermore, analysis of the elution curves can provide some measure of insight into the basic mechanisms that govern the drug release. However, significant limitations of this approach are that it can only describe mechanisms in general terms (e.g. diffusional or structural relaxation-controlled release) and that it falls short when dealing with more complex systems in which the dominant mechanism may be different in various stages of release.

To understand drug release on a more fundamental level requires analysis of the structural and morphological characteristics of the material and how they relate to the elution curves. By correlating the drug elution curves with temporal changes in the disk morphology and microstructure, it is possible to gauge how various possible mechanisms affect drug transport. The unique contribution of the MRI protocol developed here represents the first time that the spatially-resolved internal structure of CPP materials has been studied using a non-destructive method that allows repeated measurement over time.

Because no model currently exists to describe drug release from CPP bioceramics, an approach to data analysis has been developed that accounts for the shifting importance of mechanisms at different stages of the release. This approach is described and used in a discussion of the drug elution results. These results are then correlated with the evolving physical characteristics at both the "group" level (using averages of the data) and at the individual disk level as well.

5.1 Model-Free Correlation of Drug Elution with Physical Characteristics

When a drug-delivery system is described by a model, physical characteristics of the system are used to parameterize the rate of elution of the drug. Where the parameters are known, the model can be used for prediction; conversely, where the parameters are not known, measurement of drug release curves can be interpreted within a model framework to yield insight into the controlling mechanisms.

In the case of CPP bioceramics, the drug elution is a complex process that does not generally conform well to existing models, with time-dependence in the mechanisms that leads to apparent stages in the release. While development of a model for release from CPP disks is beyond the scope of the present work, we seek here to correlate the elution behaviour with the characteristics of the morphology and microstructure observed via MRI and optical data. By doing so, we aim to understand what mechanisms are most important to drug release rates and to understand how these mechanisms evolve over time.

After presenting the elution results, the apparent stages in the material are defined, which provide a framework for subsequent analysis of the results.

5.1.1 Vancomycin Elution Results

Like the swelling data from the previous chapter, elution data exist for both the MRI samples and the BAK samples, and these two may be averaged across the MRI samples ($n = 3$), the BAK samples ($n = 3$), or ALL the samples (MRI + BAK) together ($n = 6$). In the figures contained in this section, the MRI samples are indicated using solid lines, the BAK samples are indicated using dotted lines, and plots of ALL data are made using solid lines.

The cumulative drug release plots are shown for each of the G1 and G2 disks in Fig. 5.1. For these data, the error bars represent the cumulative uncertainty from the drug mass measurements. The averages of the MRI and BAK samples are shown in Fig. 5.2, while the averages of ALL samples are shown in Fig. 5.3. In these two plots, the uncertainties come from the standard deviation across the samples included in the average.

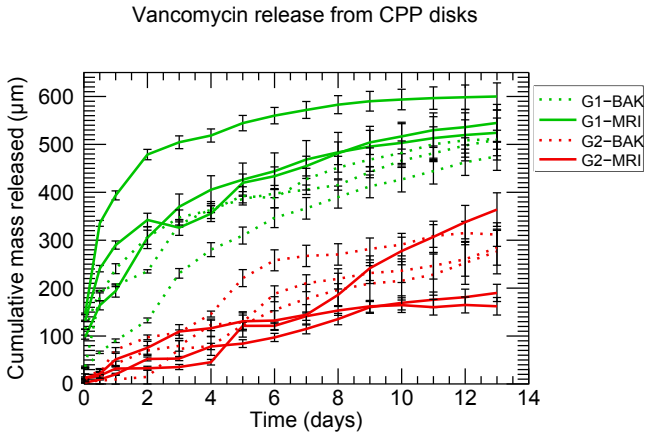

Figure 5.1: Vancomycin elution from the individual samples. Solid lines represent data from MRI samples and dotted lines represent data from BAK samples.

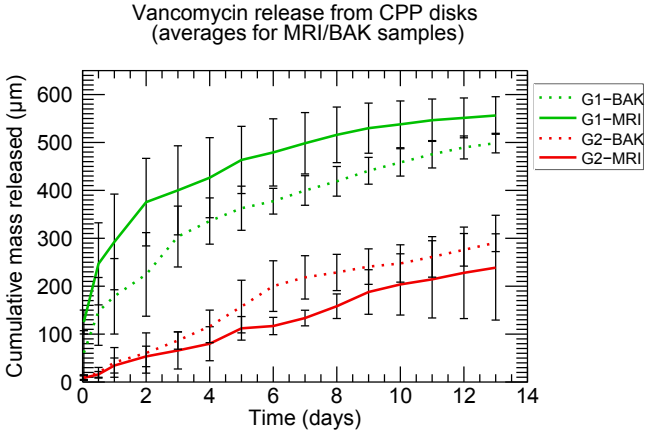

Figure 5.2: Vancomycin elution from the $n = 3$ averages. Solid lines represent data from MRI samples and dotted lines represent data from BAK samples.

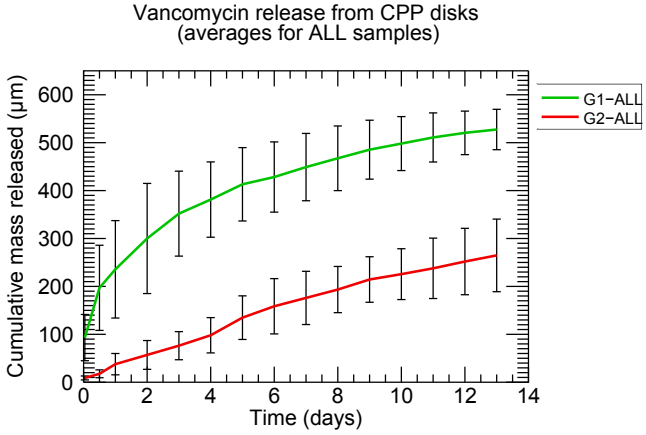

Figure 5.3: Vancomycin elution from the $n = 6$ (ALL) averages.

	Sample(s)	n	VCM burst release, b
Individual samples	G1-BAK-6.1	1	-17.80 μg *
	G1-MRI-6.2	1	90.96 μg
	G1-MRI-6.6	1	78.83 μg
	G1-BAK-6.7	1	84.73 μg
	G1-MRI-6.10	1	73.02 μg
	G1-BAK-6.11	1	19.55 μg
Average	G1-ALL	6	62.30 μg
	G1-MRI	3	88.16 μg
	G1-BAK	3	31.04 μg

Table 5.1: Burst release of drug for G1 disks, obtained through Higuchi plots

A characteristic of drug release from G1 disks is the burst effect when the disk is immersed in the buffer, and this is defined by b, the projected y-intercept. Since the release curve is non-linear, the estimate of this parameter must be made by a linearization of the curve. One approach to this problem is to create a "Higuchi plot", where the drug release is plotted versus the square root of time, $t^{1/2}$ [7]. The Higuchi plot is based on systems where release is controlled by Fickian diffusion, which has a $t^{1/2}$ time-dependence. This was done for the individual G1 samples in Fig. 5.4(a), then for the $n = 3$ and $n = 6$ averages in Figs. 5.4(b) and 5.4(c). The burst release was examined in the G2 data also, but these disks consistently showed no burst effect (i.e. $b = 0.0$, within uncertainty). Table 5.1 summarizes the G1 results.

Looking at the average drug release profiles (Fig. 5.3), general trends in the

*Take this as $b = 0.0$ μg on grounds that negative b is non-physical.

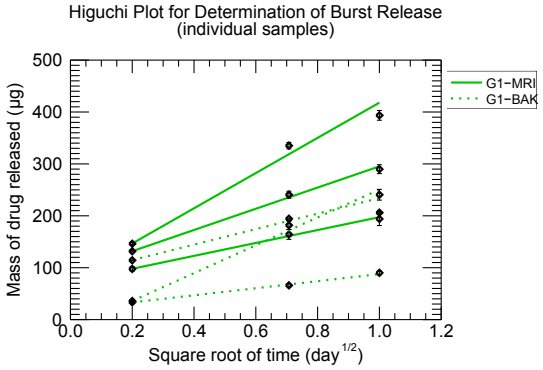

(a) Individual samples

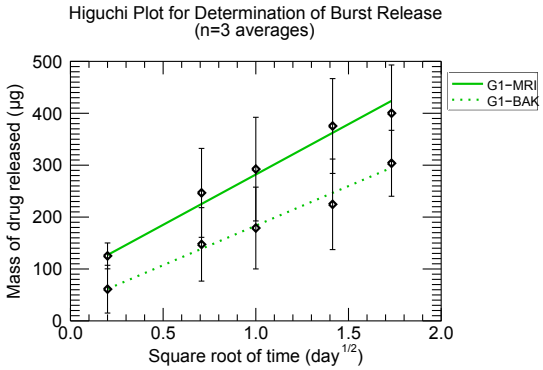

(b) The n=3 averages

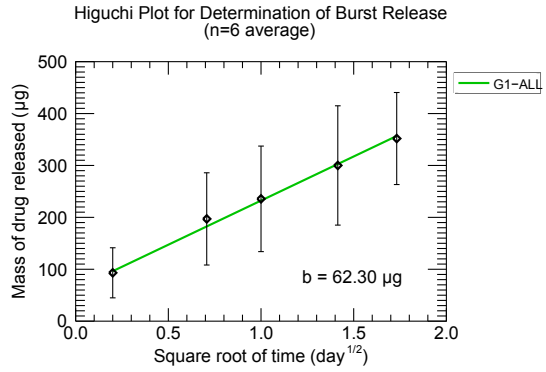

(c) The n=6 averages

Figure 5.4: Higuchi plots of G1 release data at early times to obtain the burst release parameter, b. Plots are for (a) individual samples, and for (b) the $n = 3$ and (c) the $n = 6$ averages. Solid lines represent data from MRI samples and dotted lines represent data from BAK samples, except in (c), where the solid line represents ALL samples.

release from G1 and G2 disks can be seen. The initial release from G1 disks is more rapid than from G2 disks and the function appears to asymptotically approach the theoretical loading. The release from G2 disks, on the other hand, appears to be nearly linear (the rate is nearly constant). From the uncertainties in the average data, it can be seen that the variation between samples is large. Furthermore, the individual release curves (Fig. 5.1) show that the variation is not just in the amount of drug released, but also in the *shape* of the elution curves.

5.1.2 Stages of Release

As seen in the previous chapter, CPP disks may contain initial porosity, they swell over time, they may undergo morphological changes (such as rupture), and they exhibit changes in the internal microstructure that appear to affect the distribution and proportions of free versus bound water. These characteristics have potential to influence the drug release rates.

With several release mechanisms working in conjunction, the dominant mechanism may actually shift over time. A simplifying approach, therefore, is to divide the elution period for each disk (15 measurement time points over 14 days) into stages and analyze the release characteristics in each one separately.

To refer to the stages we label and define them as follows:

Stage 1: Initial Burst	The rapid release of drug immediately upon introduction of the buffer, and characterized using the first measurement time point (at $t = 1$ hour)
Stage 2: Initial Swelling	A period of rapid volume increase over the first couple of days, between $t = 0$ and the swelling transition time.
Stage 3: Later Times	A period of less rapid swelling, separated from stage 2 by the swelling transition time

Stage 4: Disk Rupture	A period beginning with breakage along the center of the disk (apparent in the photographs) and ending with the re-joining of the two parts

While the first three stages occur sequentially, stage 4 is unique in that it may occur any time during stages 2 or 3. The swelling transition times and the times when bulk erosion is apparent are given in Tables 4.2.2 and 4.1, respectively.

5.2 Group-Level Analysis

What follows is an investigation of the drug release behaviour in relation to the CPP microstructure/morphology. The data are analyzed in two main ways: at the group level and at the individual level. The group-level analysis (§5.2, this section) is an investigation of general trends in the averages of the two sample groups (G1 and G2). The individual-level analysis (§5.3) concerns systematic variation between the samples within each group. At each level (group/individual), stages 1 – 4 will be analyzed one-by-one with an approach specific to each.

In addition to the group-level and individual-level analyses, a more detailed study of the data from certain "special" samples is made (§5.4). These samples were identified based on either a) close agreement with the average drug release, or b) extremes of drug release (very rapid/very slow). The distinctive characteristics in the swelling or MRI data from these samples are then investigated for correlation with the drug release.

5.2.1 Stage 1: Initial Burst

"How Does the Amount and State of the Sorbed Water Relate to Extent of Burst?"

The two disk types are different in that G1 disks exhibit a burst release, while G2 do not. In part, the mechanism for initial burst is thought to be due to drug adsorbed on surfaces, including pores walls, which dissolves and is released quickly after immersion in buffer.

Although this simple mechanism is essentially understood, the MRI allows comparison of certain aspects of the microstructure around the time of initial burst. Specifically, it can detect the amount of fluid absorbed in the disk (from the spin-density maps), as well as the proportion of "free" versus "bound" water (from the relaxation time amplitudes). It is known that G1 disks contain a greater amount of free water and release a greater amount of drug than G2 disks, so here we explicitly compare estimates of the free water content and amount of drug released.

The spin-density maps (Fig. 4.5) show the distribution of water within the disks. To give an estimate for the relative amount of water absorbed, the density profiles can be averaged over the entire height of the disk in the following way:

1. The average disk heights (h_{avg}) were calculated for G1-MRI and G2-MRI samples.

2. The mean fluid density ($\langle\rho\rangle$) was calculated in the range $z = (0, h_{avg})$.

3. The uncertainty in $\langle\rho\rangle$ was the standard deviation of the fluid density profiles used in the average.

In general, the relaxation times and ADC comprise biexponential components. In each case, the longer of these (the a-component) is thought to be most closely-related to "free" water, while the shorter one (the b-component) is thought to be more closely-related to "bound" water. An estimate of the fraction of free water (F_a) can be made by dividing the "free" component amplitude by the total amplitude.

$$F_a = \frac{M_a}{M_a + M_b} \tag{5.1}$$

This gives the free water fraction in the disk. For comparison between disks, however, F_a must be scaled by the mean fluid density, $\langle\rho\rangle$. We call this quantity F'_a, which is calculated using the following equation.

$$F'_a = F_a\langle\rho\rangle \tag{5.2}$$

The F_a and F'_a numbers were calculated using both the T_2 and T_1 data. The two data types are included for comparison, but since T_2 is less sensitive to exchange weighting, and is also free from relaxation weighting, it is expected to produce the more reliable

Disk Type:	G1	G2
h_{avg}	1.707 mm	2.572 mm
$\langle\rho\rangle$	$25.9\% \pm 2.5\%$	$22.2\% \pm 5.93\%$
T_2**:** F_a	44.9%	24.1%
T_2**:** F'_a	11.6%	5.35%
T_1**:** F_a	66.0%	34.4%
T_1**:** F'_a	17.1%	7.64%
VCM release	$14.69\% \pm 7.58\%$	$1.35\% \pm 0.81\%$

Table 5.3: Free water fractions and vancomycin released during the "Initial Burst" (stage 1)

F_a/F'_a values. The ADC data were not analyzed here because the long TE results in significant relaxation weighting of the D_a and D_b amplitudes.

To compare the amount of drug release, the fraction of VCM released between $t = 0$ and $t = 1$ hour was calculated. This was done by dividing the value of each VCM curve at $t = 1$ hour by the total theoretical mass of VCM loaded in the disk.

The results are summarized in Table 5.3.

Averaged over the whole disk, there is actually not much difference in the total amounts of water ($\langle\rho\rangle$) at 1 hour. The free water fraction (F'_a) differs for G1 and G2 disks as expected, which indicates a greater amount of free water in G1 disks than in G2. The F'_a values calculated using T_1 data appear to be greater than those calculated using T_2 data. Despite this difference, the effect seems to scale F'_a *evenly* for G1 and G2 disks... in both cases, the G1 free water fraction is about 2.2 times greater than for G2.

The discrepancy between the F'_a obtained from T_1 and T_2 likely arises in part from differences in relaxation weighting. While the CPMG measurement ($T_{2)}$ is free from relaxation weighting, the IR measurement contains an echo delay (TE) of 1.550 ms, during which time the signal is subject to T_2 relaxation. Because the T_{2b} relaxation time is very short (≈ 5 ms), this component will tend to be under-weighted, which would result in an apparently higher free-water fraction (F'_a). The effects of exchange may also contribute to the difference as well.

In actuality, the burst release is related not just to the porosity, but also to the fact that drug tends to be distributed more toward the top face of G1 disks [7]. What this analysis demonstrates is that the free- and bound-water components interpreted

through the MRI signal amplitudes are qualitatively consistent with known characteristics of the CPP microstructure (e.g. degree of porosity) that relate to the difference in the drug release from G1 and G2 disks.

5.2.2 Stage 2: Initial Swelling

"Can Drug Release Be Described Using a Coupled Diffusion/Relaxation Model?"

Previously, drug release from CPP disks has been analyzed using a semi-empirical equation formulated by Peppas [83] and modified by Dürig [84] to describe elution from polymeric drug delivery devices [85].

$$\frac{m_t}{m_\infty} = k\,t^n + b \tag{5.3}$$

Here, m_t/m_∞ is the fractional drug release at time t, k is a geometrical/structural factor, n is the release exponent (which can be used to infer the release mechanisms), and b is an added term to account for the "burst" effect.

A subsequent article by Peppas [86] introduced a modified equation intended for cases of coupled diffusion/structural relaxation release mechanisms. It expresses drug release via explicit terms for Fickian diffusional release (ordinary concentration gradient-driven drug transport) and for structural relaxation (release controlled by stresses in hydrophilic, glassy polymers).

$$\frac{m_t}{m_\infty} = k_d t^n + k_r t^{2n} + b \tag{5.4}$$

Here, t is normalized time, the k_d/k_r factors are constants that represent the weighting of the diffusional/relaxational mechanisms, and the release exponent n is determined *a priori* from the aspect ratio of the device. Because only the top face is exposed for the samples in this study, the aspect ratio is effectively ∞, and $n = 0.5$. The equation that appears in the article does not include the b parameter, but has been added here to account for burst effect.

The G1-ALL and G1-MRI averages were fit to equation 5.4 as a way of assessing the relative importance of diffusional and structural-relaxation mechanisms. The b parameter was constrained using the values recorded in Table 5.1, and the fitting range was selected first to be the "initial swelling" period (up to the swelling transition

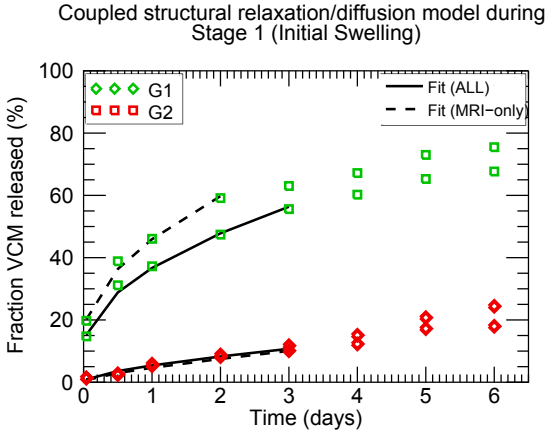

Figure 5.5: Fits to a coupled relaxation/diffusion drug release model for G1 (green squares) and G2 (red diamonds) disks. Solid lines are fits to the ALL averages and dashed lines are for the MRI averages.

time given in Table 4.2.2). These ranges were then reduced as necessary to contain fractional drug released of no more than 60% of the total, as required for application of the theory.

The fits are shown in Fig. 5.5 and the fit results are shown in Table 5.4. The quantity reported in the last column compares the percent weighting of the relaxational contribution (k_r) across the fits, and is calculated according to the following formula.

$$\frac{k_r}{k_d + k_r} \times 100\% \tag{5.5}$$

This equation has no direct, physical interpretation, but serves only as a metric for the contribution of relaxational processes to the drug release. The limits are 0% – 100%, where 0% represents purely diffusion-controlled release and 100% represents purely structural relaxation-controlled release.

The question posed in this section is, "Can drug release be described using a coupled diffusion/structural relaxation model?" The answer is "Yes," because the fits generally have both a k_d and k_r contribution, which indicates combined diffusional/structural relaxation release mechanisms. The fractional contribution from the relaxational component is much smaller in G1 disks than in G2 disks, however, indicating that release from these materials is almost entirely diffusion-controlled.

Disk Type	Averaging	Time range	k_d	k_r	Percent relaxational contribution
G1	ALL	0 – 3 days	0.2686	0.0000	0.00%
	MRI	0 – 2 days	0.3102	0.0099	3.08%
G2	ALL	0 – 3 days	0.04299	0.01097	20.3%
	MRI	0 – 3 days	0.03040	0.01596	23.4%

Table 5.4: Diffusional and structural relaxation contributions to the average drug release from CPP disks.

"How Does Microstructure Relate to Mode of Release?"

The drug release in the initial swelling period appears to be a combination of diffusion and structural relaxation mechanisms, with G1 release being predominantly diffusion-controlled, and G2 release having a strong relaxational contribution. Related to this, the MRI parameter amplitudes can provide an indication of the relative fractions of free or bound water. The availability of free water is expected to be important for diffusive transport of the drug.

The timecourse plots of the average ($n = 3$) MRI parameters (T_1, T_2, and ADC) from an integrated ROI were shown in Figs. 4.8, 4.11, and 4.13. These plots presented the average parameter values over a floating 20% range at the center of the disk.

The T_2 data are of particular interest in this set of figures, because these are the least-affected by exchange, and therefore the T_{2a}/T_{2b} amplitudes most closely-represent the proportion of free/bound water. For ease of reference, these are reproduced in Fig. 5.6, with two modifications: firstly, a plot of the average drug release curves from the corresponding MRI samples has been overlaid on the data for comparison; secondly, the amplitudes have been normalized on a per-timepoint basis (i.e. their sum equals 1). By doing so, the amplitudes are shown relative to the total signal intensity.

From Fig. 5.6, it can be seen that the T_{2a} amplitude for G2 disks ranges from 0% to 21% over the initial swelling stage (0 – 3 days). For the G1 disks, the amplitude of this same component is much greater (24% – 42%) over the corresponding stage (0 – 2 days). Overall, this indicates that the fraction of free water is much higher in G1 disks than in G2 disks.

An important distinction between G1 and G2 disks can be seen by looking at

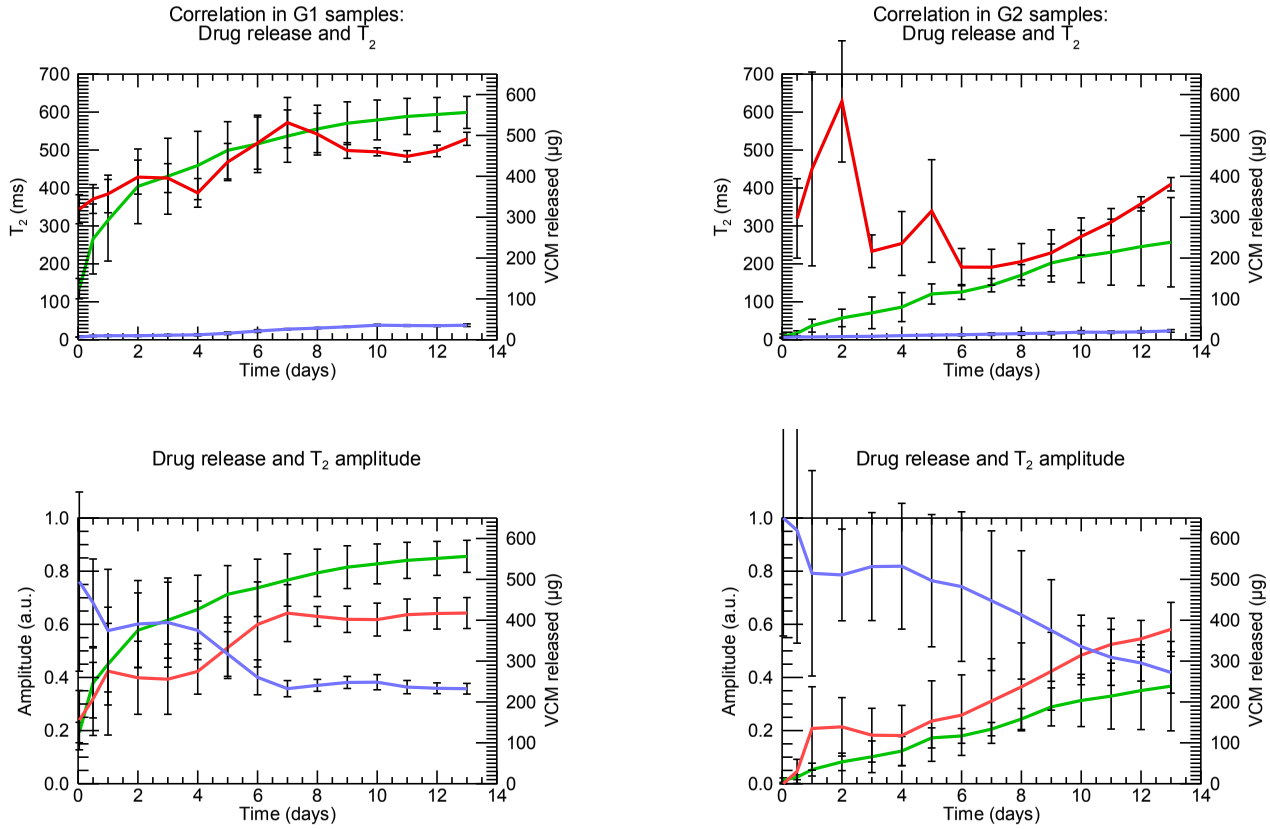

(a) (b)

Figure 5.6: The average T_2 in the ROI for (a) G1 and (b) G2 disks. The red and blue lines represent the "free" and "bound" water components, respectively, and the *relative* amplitudes are shown, which represent each amplitude as a fraction of the total signal. Also, the eluted mass of vancomycin (green) is shown with the drug mass measured on the vertical axis to the right.

the spatial characteristics of the T_2 amplitudes. These are shown in Fig. 5.7 for the initial swelling periods of each disk type. These indicate that G1 disks contain a detectable free water component at the very first time point and at all points afterward. In contrast, there is initially no detectable free water component inside the G2 disks; however, one gradually becomes apparent, progressing deeper within the disk (lower z) over time. Evidence for a distinct free water component can only be seen everywhere in the disk by 2 days, and even then it represents a much lower fraction of the total water than in G1 disks.

These observations may account for differences in the apparent drug release mechanism. The G1 disks, which contain a proportionately large free-water component at all times, exhibit a drug release mechanism dominated by Fickian diffusion. The G2 disks, which show the gradual infiltration of a detectable free-water component, exhibit a structural relaxation-controlled mechanism. In the context of exchange, the eventual appearance of a T_{2a} component at a given position is most likely due to an increasing fraction of available free water. In turn, the increasing availability of free water is likely due to swelling/degradation processes that contribute to a structural-relaxation drug release component.

5.2.3 Stage 3: Later Times

"What Mode of Drug Release is Dominant During This Stage?"

While the mode of drug release in the initial swelling stage was examined by fitting the release curve to equation 5.4 for combined diffusion/relaxation, that equation is only intended to describe the first 60% of drug release, and this precludes using it to describe the G1 data at times past the swelling transition. In addition, the uncertainties for the G2-MRI samples become quite large at later times, making interpretation of fits to the equation relatively unreliable.

The limitations of the equation leave only qualitative interpretation. From this perspective, it would appear that release from both disk types continue in their original trends (see Fig. 5.2). For G1 disks, the release continues to curve in the manner of a diffusion-dominated mechanism, asymptotically approaching theoretical drug load limit. For G2 disks, the average release maintains its nearly linear trend, suggesting that structural relaxation remains an important contributer of the release mechanism.

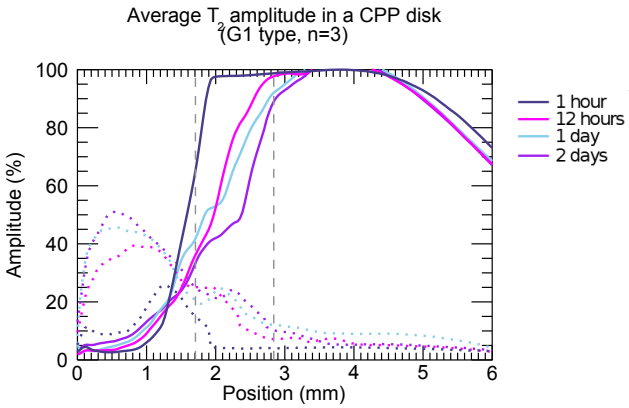

(a) G1 disks, 1 hour to 2 days

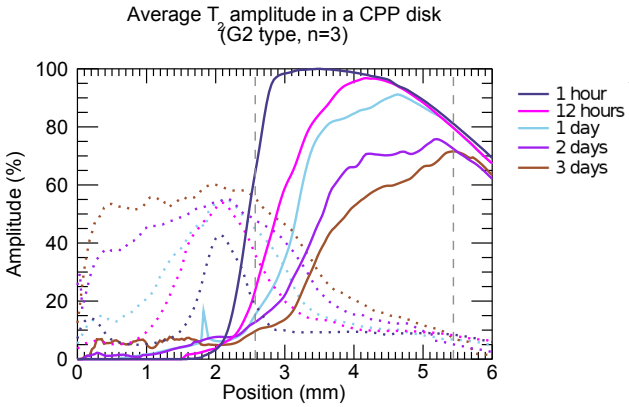

(b) G2 disks, 1 hour to 3 days

Figure 5.7: Spatial maps of the T_2 amplitudes over the initial swelling period. Time points are represented by the colours in the legend, and the vertical, gray dashed lines represent minimum height of the disk at the beginning and end of the initial swelling period.

"How Does the Microstructure Change After the Swelling Transition?"

Once again, we focus mainly here on the T_2 data because they are relatively free from exchange weighting.

Just prior to the swelling transition, the T_{2a} amplitude in G1 disks reaches a level of about 40% and remains steady there for a while. At the transition point, the amplitude starts increasing, then ultimately reaches a plateau around 60 – 65% by about 7 days.

The G2 disks only reach a level of about 20% just before the swelling transition, but like the G1 disks, they remain at this level for a time. Shortly thereafter (like the G1 disks), the T_{2a} amplitude starts increasing, but it continues increasing for the remainder of the experimental period. This amplitude comes just short of 60% by the last measurement time point.

Comparing the two sample types, the T_{2a} amplitudes show that the microstructure of G1 disks already contains significant free water prior to the swelling transition. In the period thereafter, the balance simply shifts such that the fraction of free water increases. The situation with G2 disks is different because the T_{2a} amplitudes suggest a very low initial fraction of free water that increases non-uniformly throughout the disk over time. In other words, at certain positions the free water fraction was so small as to be undetectable, but with the increase in the amount of free water comes the appearance of a distinct T_{2a} component at positions where it did not previously exist due to the fast exchange with the bound water.

While the MRI data do yield evidence for the formation/growth of a free water component, it is not immediately apparent what the nature of that component is, nor what specific mode of degradation is causing it. One possibility is continued swelling. A characteristic of CPP is that it can incorporate water via hydration to the chains. It is possible that during the initial stage, when swelling is most rapid, water is taken up primarily by hydration. When effectively all hydration sites are occupied, further swelling may be associated with an increase in free water that occupies the space between the chains.

Another possibility is that effect is due to chain scission. The progressive break-up of the matrix of CPP chains could lead to an increase in the mobility of water within the system, and thus a shift toward a larger fraction of free water.

"How Does Microstructure Relate to Mode of Release?"

Insomuch as the mode of release can be qualitatively assessed from the drug release plots in the period following the swelling transition, it would appear that G1 disks continue to exhibit diffusion-dominated release, while G2 disks continue to exhibit diffusion with a considerable structural relaxation contribution.

As discussed in the previous section, the G1 microstructure in this stage is characterized by an increase in the fraction of free water from about 40% to 60%. All the same, the release mechanism does not seem to change dramatically. Perhaps what this signifies is that it is less the specific fraction of free water that matters and more the existence of a free water component beyond a certain threshold that leads to diffusion-dominated release.

The changes in the G2 microstructure during this stage are more pronounced, characterized by a rise in the free water fraction from about 20% to 60%. It is perhaps important that this increase is not due solely to an increase in the *existing* free water fraction, but also to the formation of this component where it was previously so small as to be undetectable. Because of this, it is possible that the formation of free water occurring *gradually* throughout the extent of the disk is in part responsible for the greater structural-relaxation contribution to the drug elution.

5.2.4 Stage 4: Disk Rupture

The disk rupture occurs only for some of the samples, and there is no apparent consistency in the timing. It is very much an effect that occurs on the individual level, and as such, it is dealt with only in the following section on the individual-level analysis.

5.3 Individual-Level Analysis

Moving now from the group-level analysis of the data, we now consider data from individual variation across samples in the group.

In the previous chapter, due to the large amount and complexity of the MRI data, only the averages were presented. In this section and in the following section on the "special samples", some MRI data from individual disks are presented where

necessary.

5.3.1 Stage 1: Initial Burst

"How Does the Amount and State of the Sorbed Water Relate to Extent of Burst?"

The individual samples were analyzed using the same approach as for the group data, where the data were integrated over the entire height of the disk to get the total amount of water absorbed and the fraction of free water (using both T_1 and T_2 data). However, the number of samples is very small, and the samples are so similar that this approach yields no better insight than the group analysis.

5.3.2 Stage 2: Initial Swelling

"Does Swelling Rate Correlate with Rate of Drug Release?"

Since swelling is frequently an important mechanism used for controlled drug release, it is expected that the release rate should depend on the rate of swelling.

To determine the rates, the release and volume data were each fit to a linear model over a period in the initial swelling stage. Although the data are not strictly linear, they are approximately so for a subset of the early times, and this allows us to investigate trends during a period where the swelling behaviour is simplest. The fitting range for G2 disks was chosen to be from $t = 1$ hour to 2 days, and for G1 disks it was chosen to be 1 hour to 1 day, except for samples 6.6 (G1-MRI), which was fit only over the first two points (1 hour and 12 hours) because of its anomalous swelling behaviour.

Prior to performing the fit, the volumes were first normalized by initial volume, and the drug release data were normalized to the the theoretical loading value (m_∞), giving the fraction of drug released.

To examine correlation between swelling and drug release, the rates were plotted one against the other and fitted using least-squares regression. For the fit to the G1 data, sample 6.6 (G1-MRI) was omitted as an outlier, with far greater swelling and release rates than the other samples (datum not shown in the plot window). The uncertainties in the rates come from the fitting errors from the individual volume and

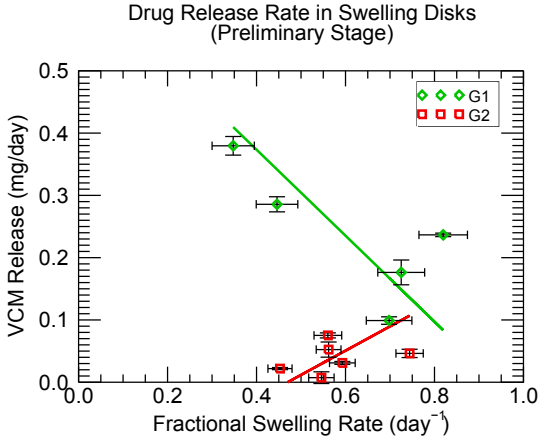

Figure 5.8: Plot for the correlation of drug release and initial swelling rates for G1 disks (green diamonds) and G2 disks (red squares). A least-squares fit to each data set (solid lines) shows little correlation between the rates: $\chi^2 = 23.8$ for the G1 disks and $\chi^2 = 42.0$ for the G2 disks.

drug release fits. The correlation plot is shown in Fig. 5.8.

The rates of swelling and drug release from G2 disks appear to show relatively little variation, and the data show no immediately-evident trend ($\chi^2 = 42.0$). The range of rates from the G1 disks show slightly more variation, and there may be a trend to the data, but it does not appear to be strong ($\chi^2 = 23.8$). Overall, it would appear that the rate of drug release does not depend on swelling rate.

"Can Individual Drug Release Be Described Using a Coupled Diffusion/Relaxation Model?"

As with the averages, the drug release curves from the individual samples (Fig. 5.1) were fit using the equation 5.4 for coupled diffusion/structural relaxation. For samples with a very short initial swelling time, the fitting range was increased to be that of the average to avoid statistical problems with fitting only 2 or 3 points.

While the model tended to fit the *averaged* data well, the individual drug release generally could not be fit to equation 5.4. This is because the model accounts for generalized diffusion or structural-relaxation mechanisms, but not individual characteristics, such as variations in the disk geometry or microstructure. The sections on "Disk Rupture" (§5.3.4) and "Special Samples" (§5.4) address some of the potential

sources for the individual variation.

5.3.3 Stage 3: Later Times

"What Mode of Release is Dominant During This Stage?"

The release during the initial swelling stage for the individual samples could not be fit using equation 5.4, and likewise, the variation between samples in the later stages is so great that no trends are readily apparent. At times, the release from individual disks is characterized by "stops and starts", where the release rate may slow for a period of a day or so, then resume a higher rate. At other times, some samples may spontaneously release a relatively large amount of drug, then resume a more moderate rate. Overall, the release from the individual samples is erratic and difficult to classify.

5.3.4 Stage 4: Disk Rupture

"How Does Disk Rupture Affect Drug Release?"

The rupture of a disk is an abrupt change in the morphology. There is an increase in the surface area, which on its own would be expected to result in either a sudden release of drug or an increase in the drug release rate. As such, a logical first approach to studying disk rupture events is to analyze coinciding features of the drug release curves.

The series of plots in Figs. 5.9 and 5.10 are the individual drug release curves for G1 and G2 disks, respectively, with markings that indicate times when the photographs reveal disk rupture. The grayed-out time periods reveal when rupture occurs, although this period is uncertain due to the 24 hour interval between photographs. For example, the photographs for sample G2-6.4 showed rupture at days 3, 4, and 6. In the corresponding plot in Fig. 5.10, this is represented as a thick gray band between 3 and 4 days, and a narrow band at 6 days, although technically the rupture could be present up to 24 hours before/after either of these ranges.

With reference to the plots of all the samples, we consider first the possibility that disk rupture has no effect on the observed drug release. Frequently, the rupture does *not* seem to coincide with increases in the release rate (G2-6.4, G2-6.8, G2-6.9), so this could indeed be the case.

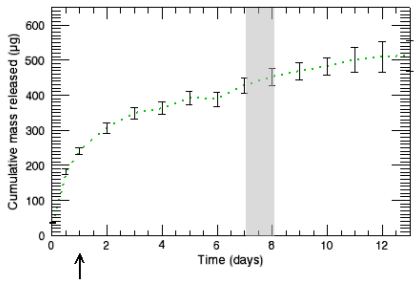

(a) G1-BAK-6.1

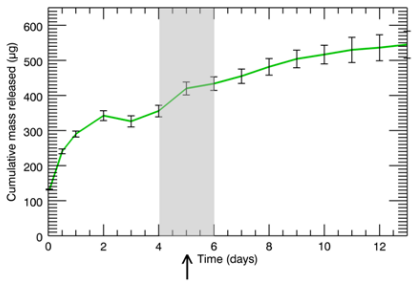

(b) G1-MRI-6.2

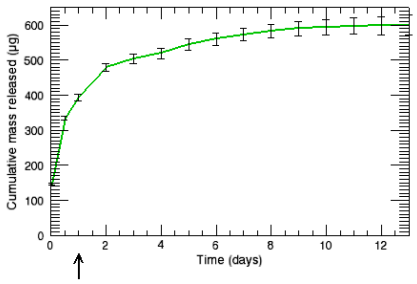

(c) G1-MRI-6.6

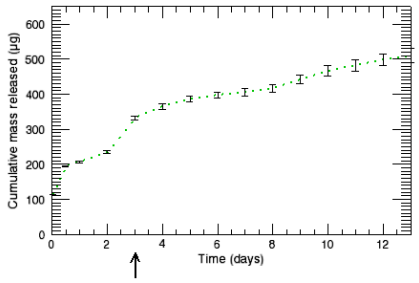

(d) G1-BAK-6.7

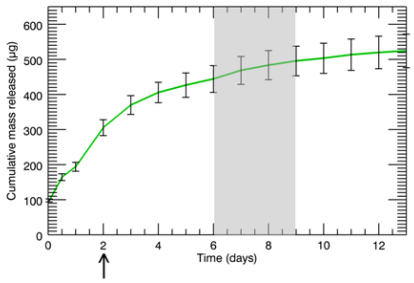

(e) G1-MRI-6.10

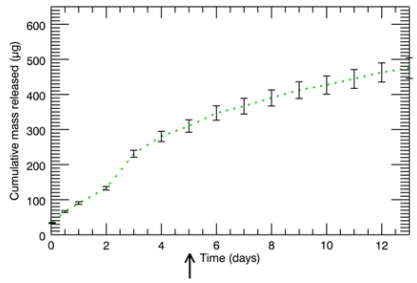

(f) G1-BAK-6.11

Figure 5.9: Drug release and rupture events for G1 samples. Times when rupture is apparent are shown as grayed ranges, and for reference the approximate swelling transition times are shown with an arrow.

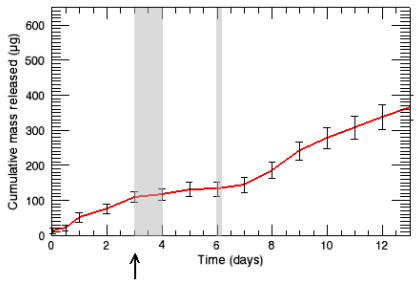

(a) G2-MRI-6.4

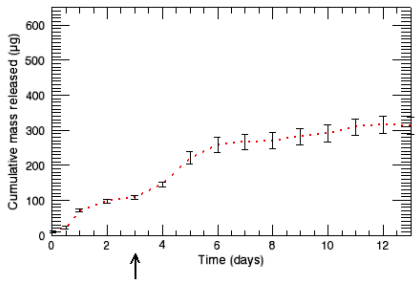

(b) G2-BAK-6.5

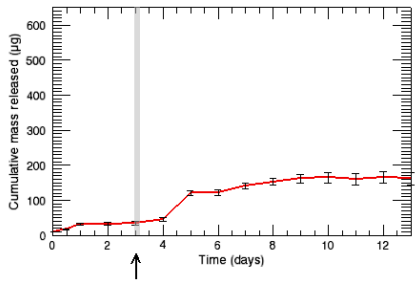

(c) G2-MRI-6.8

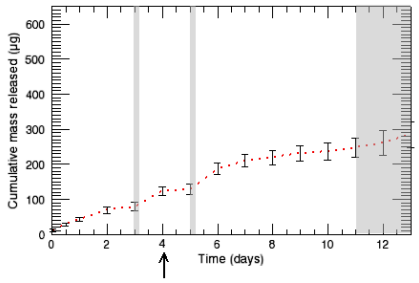

(d) G2-BAK-6.9

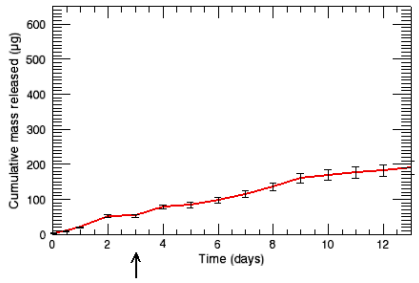

(e) G2-MRI-6.12

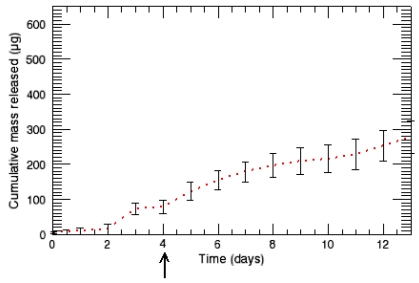

(f) G2-BAK-6.13

Figure 5.10: Drug release and rupture events for G2 samples. Times when rupture is apparent are shown as grayed ranges, and for reference the approximate swelling transition times are shown with an arrow.

In a few cases, when changes in release rate *do* coincide with rupture, the changes tend to be small relative to the error bars (e.g. G1-6.1, G1-6.10). In only one case is there a dramatic change in the release rate that coincides with the onset of rupture (G1-6.2). Together, these observations permit the possibility that rupture *does* have an effect on release rates, but that effect may be attenuated to varying degrees by some other mechanism.

Conversely, there are several times when major changes in the release rate occur even when there is no apparent rupture event (G1-6.7, G1-6.11, G2-6.5, G2-6.8). The simplest explanation is that there is a different mechanism (not rupture) that is responsible for the changes in release rate. However, it remains possible that the low sampling rate (24 hours) might allow some rupture events to go undetected if they occur entirely between time points (although there is no *post hoc* way to tell if this happens at all).

For certain samples, it would appear that a change in the release follows shortly after a rupture period (G2-6.4 and G2-6.8).

The analysis of the effects of disk rupture has not yielded any strong conclusions. What can be said is that, if rupture has any effect at all, that effect is generally small or is moderated by the action of some other mechanism(s).

In light of these observations, the photos were examined again, and it was found that in the disks that did not overtly rupture there was often a period around the swelling transition time where the material seemed to have separated into two phases, even if no open space formed between them. It could be that the rupture itself is less important, and the actual mechanism is something that engages around the same time. This mechanism could be related to the geometry of the samples (which tends to change radically near the swelling transition) or to the microstructure. More likely, it is governed by some combination of these factors.

Analysis of the effects of sample geometry is challenging, especially given only the 1-D MRI data and the 2-D optical photographs. It is somewhat more straightforward to look at microstructure of the individual samples, so the next section will focus on this.

Sample	Special characteristic
G1-MRI-6.10	Release profile close to G1 average
G2-MRI-6.12	Release profile close to G2 average
G1-MRI-6.6	Most rapid initial swelling Most rapid release
G2-MRI-6.8	Slowest initial release rate

Table 5.5: "Special Samples": list of samples, analyzed for their unique characteristics in the following subsections.

5.4 "Special" Samples

Part of the challenge of studying these CPP samples is the large variability in their behaviour once immersed in the buffer. In terms of the drug release, the swelling behaviour, and especially the morphological changes, each disk has its own unique character.

Although this large variability presents a challenge for examining the average behaviour, samples that exhibit extremes of individual behaviour may shed light on certain aspects of degradation or drug release. We classify these "special samples" according to unique swelling, geometry, or release profiles, as outlined in Table 5.5. Where more than one sample shows a similar special characteristic, priority is given to analyzing the MRI samples.

5.4.1 Sample G1-MRI-6.10: Release Profile Close to G1 Average

The analysis of the "special samples" begins with two sections describing disks that exhibit close-to-normal drug release behaviour, first for G1 disks (in this section), and then for G2 disks (in the following one). Here, "normal" is defined as general characteristics that closely resemble the average, given the geometry and setup used in the current experiment. Because of the large variation between individual samples, important details may get "blurred out" in the average. Having data from a single sample that is close to the average allows a more direct comparison between physical parameters and observed drug release.

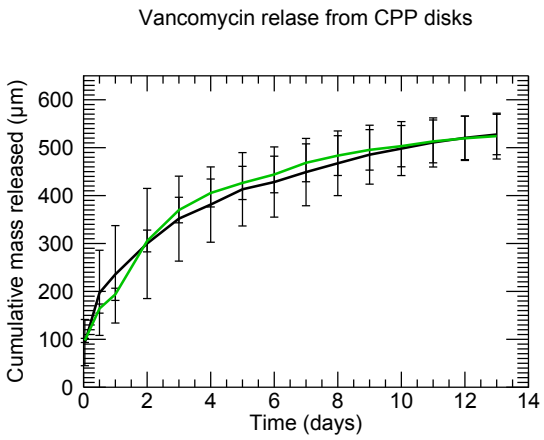

Figure 5.11: Comparison of sample 6.10-G1 (green) and the G1-ALL average (black), showing that elution from this sample is close to the average.

Elution Data

For the elution data, "normal" can be defined by a drug release curve that is close to the average in both rate and in curve shape. Figure 5.11 shows a comparison of the elution data for sample G1-6.10 and the G1-ALL average. The agreement is the closest of all the samples, and the overall shape is very similar.

MRI Data

Normal behaviour can also be defined for the MRI parameters, except that (unlike the elution data) the MRI data comprise both temporal *and* spatial information, and contain two components. Because of these added layers of complexity, "normal" MRI behaviour is characterized by a qualitative description of these components over space and time. Largely, this description is similar across the different data types (T_1, T_2, and the ADC), although the following description gives special focus to the T_2 data because the biexponential components are resolved most clearly.

The MRI data in sample G1-6.10 will be described in a series of figures starting with Fig. 5.12. These figures show the T_2 data (relaxation times and amplitudes) at several time points, and serve to illustrate important features that are evident at those times. For comparison, the data for the G1-MRI average at the corresponding time points are shown as well. The color-coding of the data for sample 6.10 follows

the convention used in previous figures, and serves to identify the time point, and the plots of the averaged data are shown in gray to distinguish them from the single-sample plots. Note that the T_{2b} component is too small to see in the relaxation time plots... this is because the scaling was intentionally chosen to highlight T_{2a}, which exhibits greater spatial variation than T_{2b}.

Figure 5.12 shows the T_2 at 1 hour post-immersion. The amplitudes show that water has been absorbed by the disk, predominantly through the top face, but also through the disk bottom. Within the disk, the biexponential components reveal that both 'free' and 'bound' water are present, but there is a greater fraction of bound water overall.

Characteristically, the T_{2b} profile is relatively simple: it is nearly constant throughout the disk. The T_{2a} varies over the height of the disk, indicating spatial variation in the exchange between free and bound water. This component increases toward the top of the disk, suggesting that free/bound water exchange is slower closer to the disk/buffer interface.

As time goes on, more and more water is absorbed into the disk, and the microstructure changes. Fig. 5.13 shows the T_2 data at $t = 2$ days which happens to be the swelling transition time for sample G1-MRI-6.10. Between 1 hour and 2 days, water has continually been absorbed, resulting in an increase in both free and bound component amplitudes. Despite the increasing *amount* of absorbed water, the T_{2b} component remains unchanged from before and is still nearly uniform throughout the disk. The T_{2a} component has dropped so that it is close to the bound component near the disk bottom, and now rises steadily toward the top of the disk. The top face of the disk itself has moved to higher z due to swelling.

For several days beyond the swelling transition time (at the 2-day timepoint), there is very little change in the T_2 maps themselves. Up until 9 days (see Fig. 5.14), both the T_{2a} and T_{2b} components remain essentially unchanged. During this interval, however, the associated amplitudes shift so that the overall amount of free water increases and the amount of bound water decreases.

While the T_2 changes very little between 2 and 9 days, the 9-day timepoint is the beginning of a period in which the free water component near the bottom of the disk increases gradually. Fig. 5.15 shows the T_2 data at 13 days, with the increased free

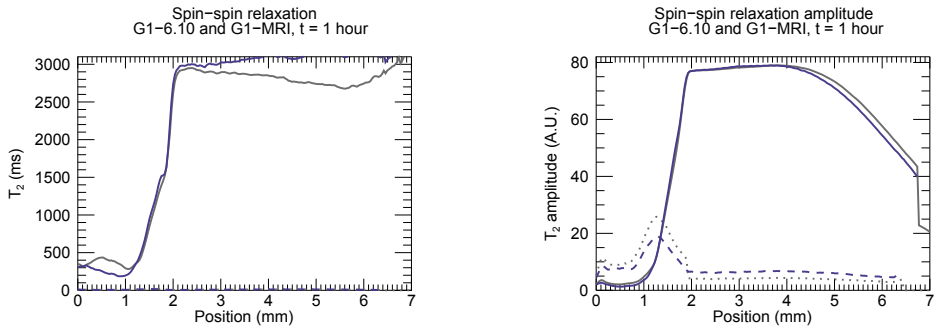

(a) (b)

Figure 5.12: The T_2 (a) and the T_2 amplitude (b) of sample G1-MRI-6.10 (dark blue) compared with the G1-MRI average (gray) at $t = 1$ hour. Solid lines represent the T_{2a} component and dashed/dotted lines represent the T_{2b} component.

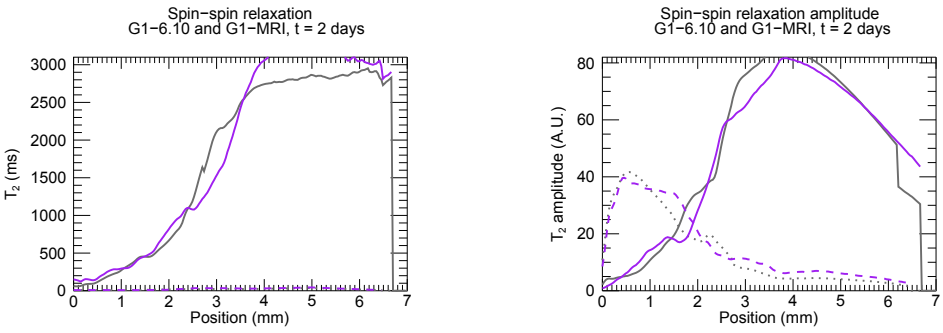

(a) (b)

Figure 5.13: The T_2 (a) and the T_2 amplitude (b) of sample G1-MRI-6.10 (purple) compared with the G1-MRI average (gray) at $t = 2$ days. Solid lines represent the T_{2a} component and dashed/dotted lines represent the T_{2b} component.

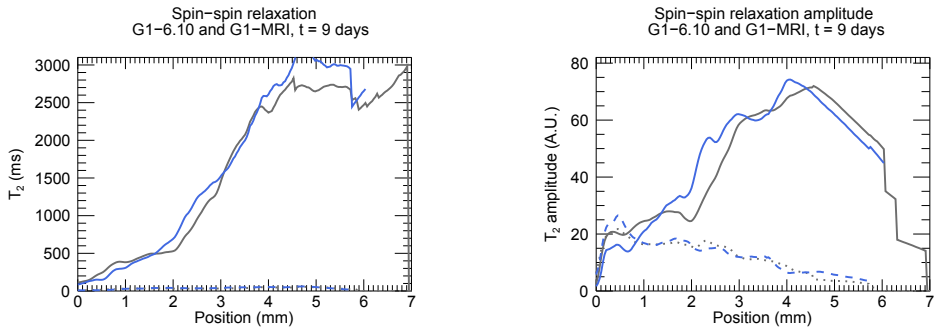

(a) (b)

Figure 5.14: The T_2 (a) and the T_2 amplitude (b) of sample G1-MRI-6.10 (blue) compared with the G1-MRI average (gray) at $t = 9$ days. Solid lines represent the T_{2a} component and dashed/dotted lines represent the T_{2b} component.

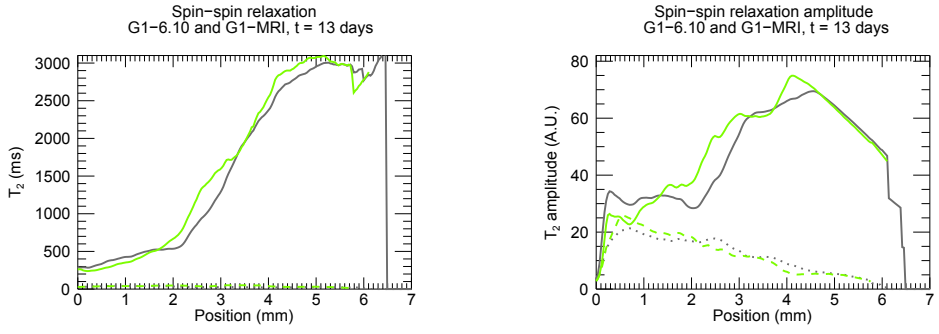

(a) (b)

Figure 5.15: The T_2 (a) and the T_2 amplitude (b) of sample G1-MRI-6.10 (green) compared with the G1-MRI average (gray) at $t = 13$ days. Solid lines represent the T_{2a} component and dashed/dotted lines represent the T_{2b} component.

water component between $z \approx 0.0$ mm – 1.8 mm.

With regards to the MRI data presented in this section, two things are apparent. Firstly, the averaged G1 data show a definite, qualitative progression (with respect to the relaxation times and their amplitudes). Secondly, the data from sample G1-6.10 possesses the same qualitative evolution, and closely resemble the average.

Although at present there is not enough information to predict specific drug release rates, the similarity between the sample G1-6.10 and the average in both the elution and MRI data lends support to the idea that the overall microstructural qualities observed in the two data sets are (at least in part) responsible for the mode of drug release observed. Moreover, knowing the essential drug release and microstructural characteristics of a typical disk allows one to detect potential causes of anomalous release that some disks exhibit by looking at major differences in the microstructure.

In section 5.4.3, this very approach is used to analyze the unusually rapid release from sample G1-6.6. First, however, an analysis similar to the one in this section is performed on sample G2-6.12, which typifies release from G2 samples.

5.4.2 Sample G2-MRI-6.12: Release Profile Close to G2 Average

Elution Data

While the average elution from G1 disks is distinctly curved and predominantly diffusion-controlled, the average elution from G2 disks is nearly linear, having strong relaxational *and* diffusional components. While sample G2-BAK-6.13 has the elution curve that most closely agrees with the average, no MRI data is available for that sample. Although the elution rate for sample G2-MRI-6.12 is slightly less than average, the overall shape agrees quite well, so this sample is analyzed presently as one that typifies the G2 release (see Fig. 5.16).

MRI Data

As in the previous section, the MRI data for sample G2-MRI-6.12 will be described in a series of figures starting with Fig. 5.12. Again, the color coding for sample G2-MRI-6.12 serves to identify the time point, and the averaged data are shown in gray.

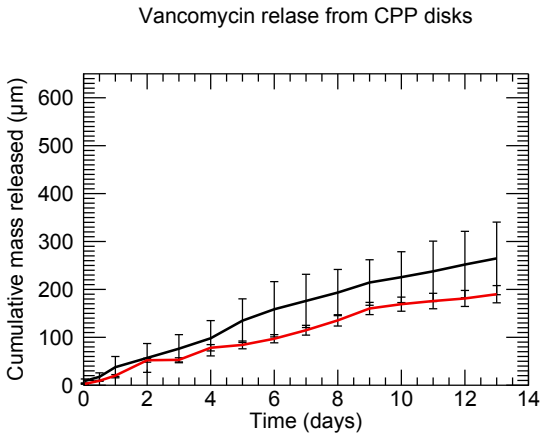

Figure 5.16: Comparison of sample G2-MRI-6.12 (red) and the G2-ALL average (black). Although the elution from this sample is not the closest to the average, the overall shape is very similar, and 6.12-G2 is the best choice from among the MRI samples.

Figure 5.17 shows the T_2 at 1 hour post-immersion. There are similarities between these data and the G1 data at the same time point. Namely, they both show that water has been absorbed in the disk, mostly from the top surface, but also in part through the bottom surface. The most striking difference between the two is there is no detectable free water component apparent throughout most of the G2 disk, only bound water component (possibly in fast exchange with free water).

Following $t = 1$ hour, the disk continues absorbing water, which appears in the bound component. Eventually, a free component forms, occurring first near the top of the disk, and then gradually deeper down. Fig. 5.18 shows the disk at the swelling transition time ($t = 3$ days), at which point the free component has formed everywhere throughout the disk. Actually, this is already the case at $t = 2$ days, but the data are shown at the transition time for consistency. Even though two components are apparent, the relaxation times near the disk bottom ($z = 0.0$ mm – 1.0 mm) are very close to each other.

Following $t = 3$ days, water continues to be absorbed, most of it into the free component, although this does not result in much change to the relaxation time itself until 8 days (Fig. 5.19). At 8 days, the T_{2a} begins rising, becoming more distinct from the T_{2b} component. This continues, and by 10 days (Fig. 5.20), the difference

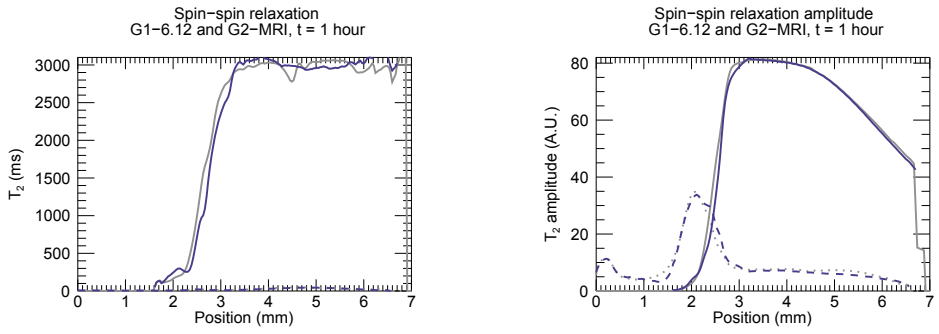

(a) (b)

Figure 5.17: The T_2 (a) and the T_2 amplitude (b) of sample G2-MRI-6.12 (dark blue) compared with the G2-MRI average (gray) at $t = 1$ hour. Solid lines represent the T_{2a} component and dashed/dotted lines represent the T_{2b} component.

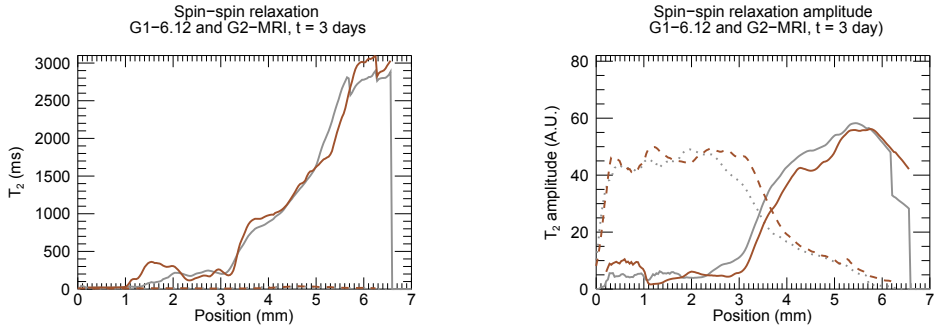

(a) (b)

Figure 5.18: The T_2 (a) and the T_2 amplitude (b) of sample G2-MRI-6.12 (brown) compared with the G2-MRI average (gray) at $t = 3$ days. Solid lines represent the T_{2a} component and dashed/dotted lines represent the T_{2b} component.

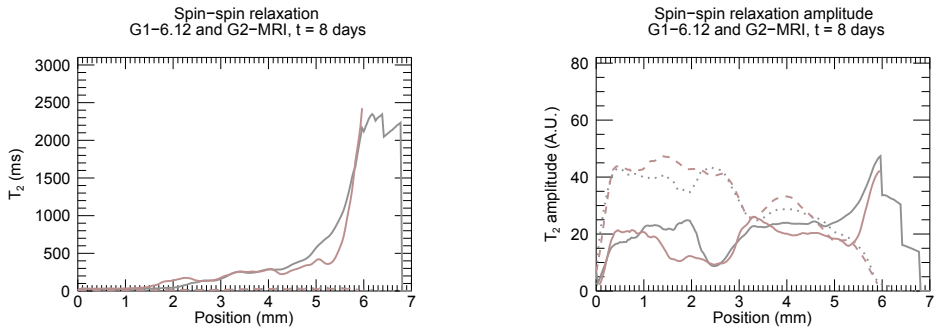

(a) (b)

Figure 5.19: The T_2 (a) and the T_2 amplitude (b) of sample G2-MRI-6.12 (light brown) compared with the G2-MRI average (gray) at $t = 8$ days. Solid lines represent the T_{2a} component and dashed/dotted lines represent the T_{2b} component.

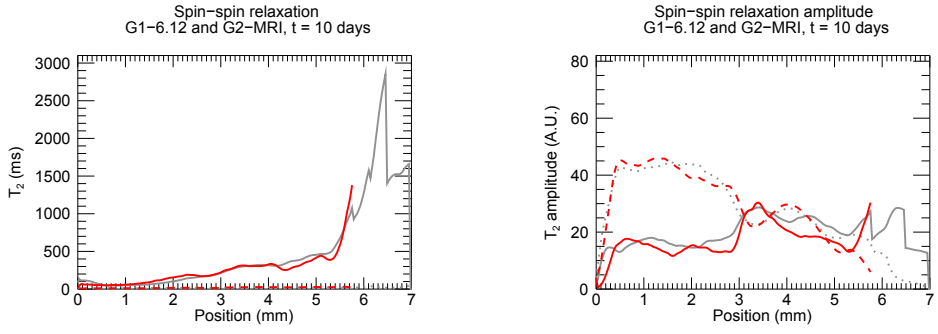

(a) (b)

Figure 5.20: The T_2 (a) and the T_2 amplitude (b) of sample G2-MRI-6.12 (red) compared with the G2-MRI average (gray) at $t = 10$ days. Solid lines represent the T_{2a} component and dashed/dotted lines represent the T_{2b} component.

has become quite large.

5.4.3 Sample G1-MRI-6.6: Most Rapid Initial Swelling; Most Rapid Release

We now turn to two samples that deviate from the average behaviour. Sample G1-MRI-6.6 is unusual in several ways. Firstly, it exhibits explosive swelling during the first 12 hours (faster than any other sample). Afterwards, the disk actually seems to shrink, then swell very little over the remainder of the experimental period. The final swelling fraction is the lowest of all the samples ($1.74 \pm 2.49\%$ times the original size).

Elution Data

With regards to the drug release (see Fig. 5.21), it is the most rapid of any of the samples. By 5 days, the fractional release from sample G1-MRI-6.6 surpasses the final release fraction of any of the other samples (at 13 days). From fitting to the combined relaxation/diffusion drug release model, sample G1-6.6 appears to exhibit purely diffusion-controlled release. It would appear that drug diffusion from this sample is simply more rapid than from other samples.

The explanation for the extremely rapid swelling in the initial period is not known, but it would appear that there is something about this sample that causes the gelling reaction to proceed more quickly than in other samples. It is paradoxical that the drug release is also the most rapid, because swelling is typically seen as a mechanism for release control.

MRI Data

The spatially-resolved MRI data may provide clues to explain the swelling and the rapid release. The T_2 for sample G1-MRI-6.6 at $t = 2$ days is shown in Fig. 5.22, along with the average of *the other two G1 samples* (6.2 and 6.10). The average here was computed *without* sample 6.6 because, with only three samples to work with, doing so helps to highlight contrasting features.

It can be seen that the T_2 for sample G1-MRI-6.6 is characteristically different from the average. While the free component in the averaged data drops continuously between the pure buffer toward the disk bottom, sample G1-MRI-6.6 has a region

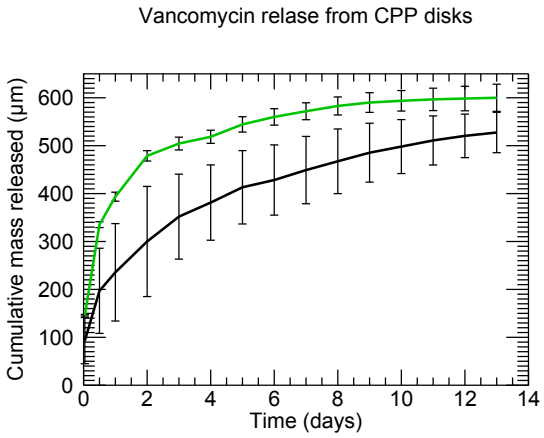

Figure 5.21: Comparison of sample 6.6-G1 (green) and the G1-ALL average (black). The elution from this sample is more rapid than other G1 samples, and appears to be nearly entirely diffusion-controlled.

near the center of the disk where the T_{2a} and the associated amplitude are higher than expected. This suggests that this sample contains an anomalously high fraction of free water in this region. The data are shown at $t = 2$ days because the volumes of all the samples are nearly the same at this timepoint, which makes for the clearest comparison. Nonetheless, this special feature is present from the very first time point ($t = 1$ hour) and persists for all times.

There is no definite explanation for this feature, but it is consistent with the elution data: there exists a distinctive region of elevated water mobility, and correspondingly elution from this sample appears to be entirely diffusion-controlled. One possibility is that there was a large void in the sample that allowed water to enter more rapidly. With regards to swelling, the greater availability of water within the disk could explain the rapid early swelling, and the later reduction in volume could have been a result of the void collapsing. As for elution, the predominantly diffusive release mechanism could have also been because of the greater availability of free water. The only evidence against this theory is that the fluid density maps do not have a corresponding feature that should occur if there were a water-filled void inside the disk.

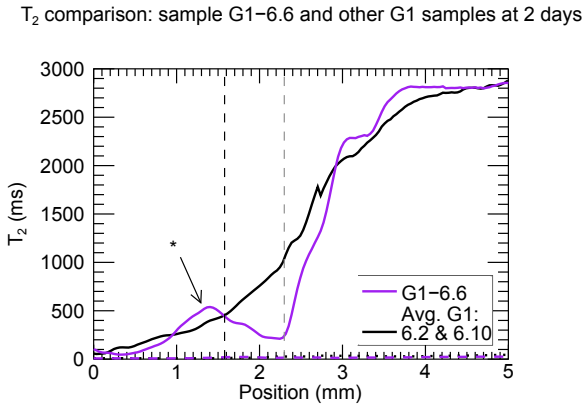

(a)

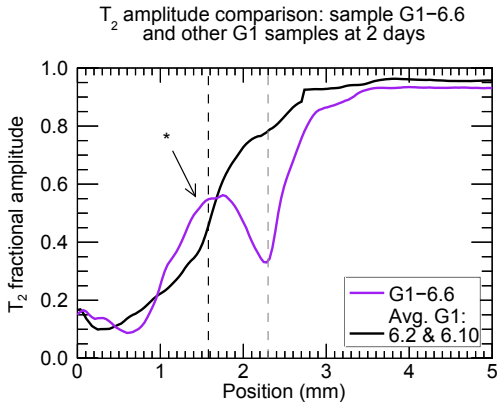

(b)

Figure 5.22: The T_2 (a) and the T_2 amplitude (b) of sample G1-MRI-6.6 (purple) compared with the average of G1 samples G1-MRI-6.2 and G1-MRI-6.10 *only* (black) at $t = 2$ days. Solid lines represent the free water component and dashed lines represent the bound component, although the bound component is omitted from the relative amplitude plots for clarity (it is just calculated as $M_b = 1 - M_a$). The vertical lines represent the minimum disk height at $t = 0$ (black) and at $t = 2$ days (gray). The feature near the disk center with unusually high T_2 (and associated amplitude) is indicated with an asterisk ($*$).

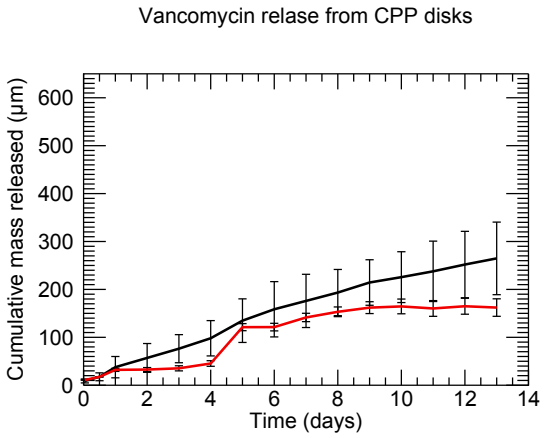

Figure 5.23: Comparison of sample G2-MRI-6.8 (red) and the G2-ALL average (black). The elution from this sample is the slowest of all samples over the first 4 days. Between 4 and 5 days there is a rapid release of drug, after which the release continues again at a moderate rate.

5.4.4 Sample G2-MRI-6.8: Slowest Initial Release Rate

Sample G2-MRI-6.8 is of interest because it releases the least amount of drug of any sample over the first 4 days (in this way, it is the opposite of sample G1-MRI-6.6, which releases drug at the most rapid rate).

Elution Data

Elution from sample G2-MRI-6.8 is shown in Fig. 5.23 with the G2-ALL average included for comparison. The release rate over the first 4 days is the slowest out of all the samples. It is unlikely that swelling would be the controlling factor for this, because the volume curve of this sample is very close to the average for G2 disks.

MRI Data

The MRI data show some interesting features that may help explain the slower initial drug release. While the water entering the disk does so primarily through the top face of the disk, most samples also contain a certain amount of water that enters through the bottom face. Out of all the G2 samples, G2-MRI-6.8 seems to have the least absorbed water in this region. This is demonstrated in Fig. 5.24, which compares the

T_2 amplitudes of all three G2-MRI samples at $t = 1$ hour.

As is the norm with G2 disks, there is only a T_{2b} component apparent within the material, except for near the disk surface. The elevated T_{2b} amplitude near $z = 2.0\,\text{mm}$ is water that has been absorbed through the top surface, while the same elevated amplitude near $z = 0.0\,\text{mm}$ is water absorbed through the bottom surface. From the amplitudes, it is evident that there is a some variation in how much water is absorbed by each sample. This is most likely due to the quality of the seal made by the cyanoacrylate when the disk is fixated to the spacer. Sample G2-MRI-6.8 is special in that there appears to be almost no water absorbed in the bottom.

The absorption (or lack thereof) of water though the disk bottom has a potentially important impact on the drug release, and Figs. 5.25 – 5.27 show why this might be the case. At $t = 1$ day (Fig. 5.25), although the other two samples contain water throughout the disk, the signal amplitude in the bottom of sample 6.8 (between 0.0 – 0.8 mm) is effectively nil, even though water *was* present there at earlier times (Fig. 5.24).

The disappearance of this water could be explained by the reaction of water with CPP chains. Buffer that had originally diffused into that area may eventually react chemically with the CPP chains (through hydration or scission) and diminish the signal strength through ultra-shortened T_2. With no additional water coming in to exchange with, that signal component simply disappears. The absence of any free water has important repercussions for release; without it, there is no mechanism for drug transport. In sample G2-MRI-6.8, it is possible that is the cause of the slower observed drug release.

If drug release is slow because the scarcity of water near the disk bottom, what occurs when water absorbed from the top of the disk ultimately propagates down to the bottom? Figures 5.26 and 5.27 show the T_2 amplitudes at $t = 4$ days and $t = 5$ days, respectively. At 4 days, water has finally propagated all throughout sample 6.8, and appears predominantly in the bound form (although there is some free water near the surface). By 5 days, a free water component has formed everywhere in the disk. The other samples, having had water available in these lower regions at earlier times, respond less strongly when the free water component resolves. For sample 6.8, the fact that water had not been available at earlier times means that the drug

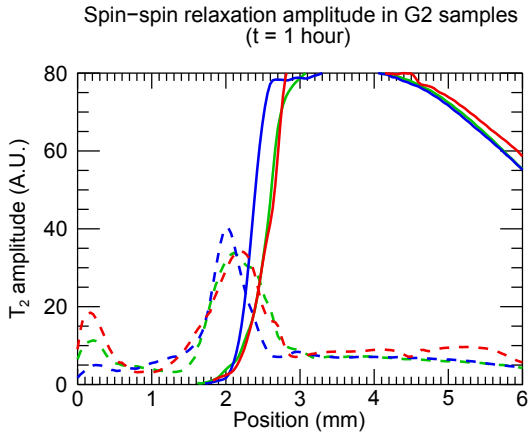

Figure 5.24: The T_2 amplitudes for samples G2-MRI-6.4 (red), G2-MRI-6.8 (blue), and G2-MRI-6.12 (green) at $t = 1$ hour. Solid lines represent the T_{2a} amplitude and dashed lines represent the T_{2b} amplitude. Relative to the other samples, G2-MRI-6.8 has absorbed almost no water through the bottom disk face.

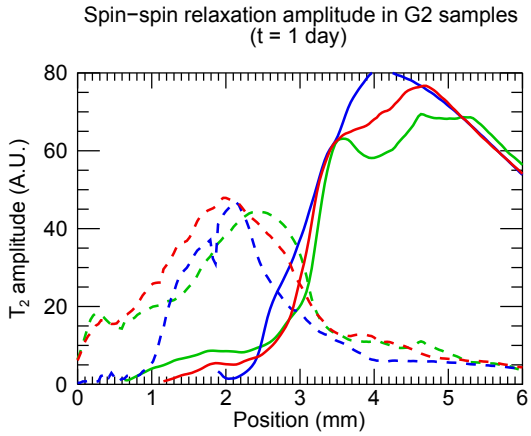

Figure 5.25: The T_2 amplitudes for samples G2-MRI-6.4 (red), G2-MRI-6.8 (blue), and G2-MRI-6.12 (green) at $t = 1$ day. Solid lines represent the T_{2a} amplitude and dashed lines represent the T_{2b} amplitude. After 1 day, the signal intensity near the bottom of G2-MRI-6.8 has dropped to nearly zero, possibly as a result of hydration to the CPP chains and the lack of additional water coming through the disk bottom.

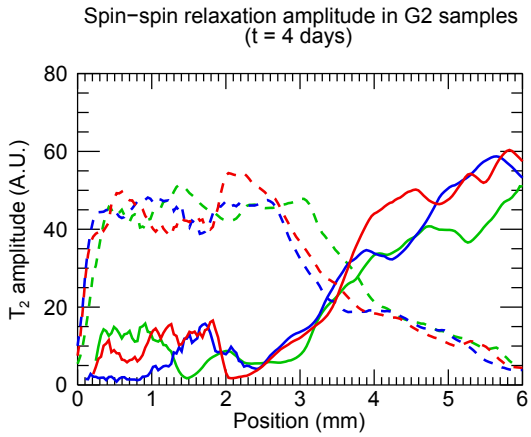

Figure 5.26: The T_2 amplitudes for samples G2-MRI-6.4 (red), G2-MRI-6.8 (blue), and G2-MRI-6.12 (green) at $t = 4$ days. Solid lines represent the T_{2a} component and dashed lines represent the T_{2b} component. At 4 days there is water all throughout the disk.

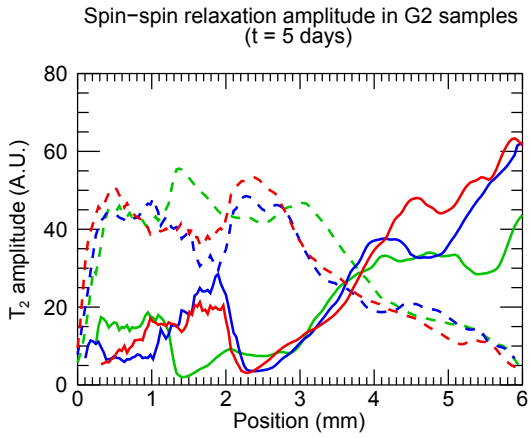

Figure 5.27: The T_2 amplitudes for samples G2-MRI-6.4 (red), G2-MRI-6.8 (blue), and G2-MRI-6.12 (green) at $t = 5$ days. Solid lines represent the T_{2a} component and dashed lines represent the T_{2b} component. At 5 days a free water component has formed everywhere throughout the disk.

concentration gradient must be greater, so that when free water becomes available, transport is rapid, resulting in the burst between 4 and 5 days (see Fig. 5.23).

5.5 Elution/Structure Correlation: Summary of Results

While the average drug release curves showed general trends in the elution from G1 or G2 disks, there was a great deal of variation between the individual samples and the averages. This was notably different from previous elution studies, and was potentially caused by the confining geometry of the NMR tubes, which enhanced the differences between samples.

Based on the observation that swelling occurs in stages, so too the correlation between elution and physical characteristics was conducted in stages. The value in this approach is that it takes into account the potential for the dominant mechanism to change over time. The stages were defined by characteristics of the drug release, the swelling transition, and asynchronous periods of apparent disk rupture. Also, the data during these stages were explored at both the group level (to examine trends in the average) and at the individual level (to examine systematic variation between samples).

During the initial swelling stage, the average elution curves from G1 disks showed a predominantly diffusion-controlled mode of release, while release from G2 curves had similarly-weighted contributions from both diffusional and structural relaxation mechanisms. When rate of drug release was compared with rate of swelling, surprisingly, there appeared to be very little correlation between the two. When compared with the T_2 relaxation data, however, it was observed that a mechanism for release may involve changes in the proportion of free water. While G1 disks exhibit a detectable free water component throughout the disk at all times, this same component in G2 disks first becomes apparent at the surface, then becomes apparent progressively lower in the disk over time. Since this represents the gradual shift in the exchange toward water in the pool with greater mobility, it may be that drug release is controlled by structural relaxation processes that vary spatially and temporally through the disk.

During later times, after the swelling transition, the characteristics of the average elution curves do not appear to change appreciably, although the individual behaviour

is much more varied. In general, the gradual growth of the free water component in G2 disks is thought to be related to progressive degradation of the matrix that leads to continued relaxation-controlled release. When disk rupture was correlated with drug elution, it was found that any effect is small, or is modulated by some other mechanism.

While the wide variation in the sample behaviour presented a challenge for interpretation of average results, the "special samples" provided unique insight into how the microstructure may be related to release. Specifically, the sample with the most rapid, diffusion-dominated release was also the one with an enhanced free-water component near the center of the disk. While the origin of this characteristic remains unknown, it lends support to the idea that free water observed via MRI is an influential factor in drug release. Other factors, like degradation initiated by water absorbed through the disk bottom may be related to some of the variation observed between samples.

Chapter 6

Summary and Conclusions

Magnetic resonance imaging is a powerful and versatile technique for characterizing drug-delivery biomaterials because it offers sensitivity to local microstructure and transport. Moreover, because it is a non-destructive technique, it is possible to observe structural changes in a biomaterial over an extended timecourse. This is important because biological implant materials may incorporate the aims of both controlled release and biodegradation, and are notoriously challenging to characterize due to the multiple, complex mechanisms that modulate drug release.

This thesis represents the first time that the spatially-resolved characteristics of the CPP microstructure have been analyzed in a way that allowed both repeated measurements on the samples as well as concurrent measurement of drug elution. The study involved stages of: 1) development and optimization of techniques for non-invasive characterization, 2) physical characterization of the morphology and microstructure, and 3) correlating drug elution with physical characteristics of the material. In the introductory chapter, a series of objectives and hypotheses for the research were presented, and these are addressed now to summarize the results.

Objective 1 Develop and optimize non-invasive techniques for characterizing CPP bioceramics.

Through the combination of appropriate magnetization preparation with a spin echo imaging sequence, techniques were developed for acquiring one-dimensional maps of T_1, T_2 and the ADC in CPP bioceramics. Performing MRI at 11.7 T allowed imaging of CPP bioceramics with high resolution. In turn, this required adapting samples for a 1-D imaging configuration and using disks with a smaller diameter (4 mm) than previously used, which required modifying the drug loading protocol.

A special characteristic of CPP is that the relaxation times and ADC are biexponential. Additionally, swelling and degradation are associated with large variation in both the NMR relaxation/diffusion parameters and the disk geometry. The MRI sequences were optimized with consideration for time-varying two-component relaxation and diffusion, as well as for changes in the disk geometry over time.

Hypothesis 1.1 MRI methods can spatially and temporally resolve microstructural and fluid transport properties in CPP bioceramics.

The measurements of relaxation times and ADC were able to resolve the generally-biexponential quality of these parameters, where the two components reflected the presence of high-mobility and low-mobility water. These components were interpreted in the context of exchange to originate from water having different transport characteristics: namely, freely-diffusing water and water bound to CPP chains.

The MRI method described in this thesis was used to acquire images with the required resolution while retaining the ability to image the full extent of the disks, even as they swell. The spatial resolution of the MRI maps was sufficient to show variation of the MRI parameters, as evidenced by the ability to resolve regions in the disk having different proportions of free and bound water. The temporal resolution of the imaging protocol was sufficient to detect the absorption of fluid, and changes in the free/bound water proportions that occurred over several measurement time points (i.e. several days).

Hypothesis 1.2 Previously-reported drug elution protocols can be adapted to the physical constraints associated with the MRI apparatus.

The MRI apparatus imposed restrictions on the geometry for disks and the volume of elution medium that could be used in an imaging study. A previous elution protocol [7] was adapted by 1) using a reduced disk size, 2) using a reduced volume of elution medium, and 3) scaling the drug loading according to the relative disk/elution medium volume. The feasibility of these changes was tested through a sink analysis, and the protocol for sampling the elution medium was modified to account for fluid

losses, thereby successfully demonstrating that the elution protocol can be modified to match the MRI setup.

Objective 2 Describe the physical characteristics of CPP bioceramics exposed to a buffer fluid.

Optical photographs and averaged MRI parameters were used to analyze characteristics of disk morphology and microstructure.

Hypothesis 2.1 Stages of morphological change can be identified using optical photography to define stages for MRI analysis of microstructural degradation.

By analysis of the optical photographs, it was observed that CPP disks undergo stages of rapid initial swelling and slower later swelling as quantified through a thresholded derivative analysis of the swelling curves. In addition to swelling, it was possible to identify periods of bulk erosion (in the form of disk rupture) from the optical photographs. Not all disks exhibited this characteristic, and that the timing varied greatly in the disks that did.

In addition to stages based on the disk morphology, a stage was added based on the "initial burst" stage of drug release. The MRI data were analyzed in the following stages separately: 1) the initial burst of drug, 2) an initial swelling period, 3) a later-time swelling period, and 4) (asynchronous) periods of bulk erosion. The measurements of average drug release were able to show that only two stages occurred in G1 disks (including the initial burst and all other times) and that average elution from G2 disk was characterized by a near-linear trend at all times.

Hypothesis 2.2 Measurements of T_2 will better resolve free- and bound-water contributions to the MRI signal than measurements of T_1.

The local proportions of free and bound water within CPP disks are of interest for drug transport, because they reveal changes in the microstructure that are expected

to affect the local diffusivity of drug. Concurrent measurements of T_1 and T_2 were acquired, which permitted a comparison of their respective ability to resolve the two signal components. These results showed that the T_2 parameter was able to resolve free/bound contributions at times when T_1 could not. From this result, I conclude that T_2 measurements are the preferred way to study the changing free and bound water components in CPP.

Hypothesis 2.3 The ADC (sensitive to material properties on the micron scale) can be used to infer information complementary to relaxation times (sensitive to material properties on the molecular scale) pertaining to local microstructural length scales in CPP.

Maps of the ADC of water within the CPP microstructure were obtained, which represented calibrated measurements of local diffusivity. Qualitative similarities between the ADC and T_1 maps were observed, as expected based on the exchange time scales for the two parameters. The diffusion maps complemented the relaxation maps because they showed a correspondence between molecular tumbling mobility and the translational diffusivity (via the biexponential components). The ADC measurements in G1 disks showed that degradation at later times causes an increase in the *amount* of free water, but not in the average diffusion distance through the local microstructure. In G2 disks, there was an overall increase in the average diffusion distance, but it could not be determined whether this was due to an actual increase in diffusion lengths or simply a shift in the exchange toward a free water component.

Objective 3 Perform concurrent drug elution, optical, and MRI measurements on CPP loaded with vancomycin.

Measurement of drug elution was performed concurrent with the non-destructive imaging techniques (optical and MRI) to observe drug release and structural features relevant to transport. This was made possible because the disks were adapted to the geometry imposed by the magnet and because the elution protocol was adapted to correct for fluid loss, which was no longer negligible in the physically scaled-down

measurement.

Hypothesis 3.1 Macroscopic changes due to swelling and bulk erosion, observed via optical photography, will correlate with differing rates of release.

Rates of drug release in the initial swelling stage did not appear to correlate with the actual rate of swelling. Bulk erosion did not tend to correlate with changes in the release rate, although it remains inconclusive whether erosion affects the release, due to the limitations of the 1-day sampling interval.

Hypothesis 3.2 Changes observed at a local microstructural level using MRI relaxation/ADC measurements will show temporal changes in the proportion of free/bound water.

The T_1, T_2, and ADC maps all showed evidence of free and bound water components in CPP, although the T_2 data were the best choice for interpreting the proportion of each type of water. By analyzing the T_2 maps, major differences were apparent in the amount of free- and bound-water in G1 and G2 disks.

Hypothesis 3.3 Changes in the proportion of free/bound water will correlate with a structural relaxation-dominated contribution to drug release.

The G1 disks showed evidence of a free-water component at all times and at all positions in the disk, and correlated with diffusion-dominated average release.

The G2 disks also show evidence of a free-water component, but it is initially undetectably small. Not only did the the free water fraction show evidence of increasing over time, but the spatially-resolved MRI measurements allowed us to observe that this increase begins near the top surface, and gradually propagates throughout the rest of the disk. These changes in the observed amount of free water correlate with a strong structural-relaxation contribution to the drug release, which I interpret as being due both to the increasing availability of free water for transport, and the spatially-dependent nature of the changes.

Future Directions

The value of this experiment is that it is the first time that spatially-resolved measurements of the microstructure have been made together with drug elution measurement in CPP. This work has established a protocol for applying MRI techniques to the analysis of drug release from degradable CPP structures, and future steps would be directed at using these techniques to gain increased knowledge geared toward optimization of the bioceramics.

From analysis of the CPP microstructure using the three different MRI parameters, this research has established the T_2 relaxation time as the best parameter to use for studying the free/bound water in the structure. With this knowledge, it is possible to shorten MRI acquisition times by concentrating on this parameter, which would permit use of a larger sample size. Alternatively, the use of a gradient coil capable of generating stronger pulsed field gradients would minimize the relaxation weighting effects in the ADC sequence. In this case, the ADC mapping sequence might be an attractive option for its ability to provide a measure of mobility with a direct, physical interpretation.

By using shorter MRI acquisition times, it would also be possible to sample more time points. Priority should be given to acquiring more data at early times (within 24 – 48 hours post-immersion). Doing so is necessary to resolve important characteristics of the drug release rates in this period, during which the CPP is undergoing the most rapid change.

The T_2 maps provide the best estimates of the proportions of free and bound water, but if actual exchange times were known, the size of the free/bound water pools could be accurately determined. Mixtures of water and CPP in varying ratios have previously been used to study CPP chemistry, and additional research performing MRI measurements on a series of these mixtures should be done to quantitatively determine the exchange times via the two-site exchange equations. Accurate knowledge of the relative size of the free/bound pools of water would lead to the ability to explore direct connections between local fluid diffusivity and transport processes related to drug release.

While the one-dimensional MRI approach lends itself well to the initial, cylindrical geometry of the CPP disks, it has limitations once the disks swell to a certain degree.

Specifically, in regions where the swollen disk and the free buffer exist side-by-side, it is not possible to distinguish between the contribution from each to the MRI parameters. One of the strengths of MRI is the ability to acquire data in three dimensions, and so the existing techniques should be expanded to include this capability. Doing so would allow not only for the characterization of the microstructure in the swollen layer, but it would also allow for more accurate 3-D volume measurements, eliminating the need for estimates based on the photographs.

Lastly, the true benefit to optimizing CPP biomaterials could be realized by using the methods developed here to understand effects of systematic changes in the material processing on drug release. One possibility would be to study "short-chain" materials that have undergone an extended G1 gelling time. This would allow study of the CPP disks minus the effect of further gelling during the measurement. Another possibility would be to image disks that had been subjected to varying levels of heat-treatment to study the effect of varying levels of amorphous/crystallized material.

Summary of Conclusions

The importance of CPP to medicine is that localized delivery has the potential to greatly improve treatment outcomes for osteomyelitis, a serious condition which frequently affects a younger population. Biodegradable implants also offer the potential to lessen inconvenience and discomfort for patients, and to reduce patient-care costs by reducing hospital stays.

What this thesis has achieved is to develop an MRI-based experiment protocol that can be used to study CPP bioceramics in a way that no other technique can. Using that protocol, I have performed the first non-invasive study of the CPP microstructure that correlates drug release and MRI parameters that are related to transport. The resulting data do not implicate a singular, governing scheme for drug release, but instead demonstrate that drug release is controlled by multiple mechanisms. Further analysis yielded an assessment of the relative importance of various mechanisms that contribute to release.

The MRI techniques that were developed and the knowledge that was gained about the signal characteristics in CPP paves the way for future MRI experiments on such materials. In turn, this offers ways to further advance understanding of drug

release mechanisms. Ultimately, the knowledge of these mechanisms has potential to improve rational development and optimization of biomaterial implants to ensure the best treatment care for patients.

Appendix A

Two-Site Exchange Example

The concept of chemical exchange is important in an NMR context, because exchange has an effect on the measurement of relaxation times. These effects are expressed by the "two-site exchange equations" (TSEE), which relate the true and measured parameters in a system via the exchange correlation time, τ. Because this system of equations is relatively complex, this section presents an example using simulated data to illustrate the effect of varying the exchange correlation time (τ). By using a large range for τ, the characteristics of slow, intermediate, and fast exchange regimes are demonstrated.

Consider a system that contains two exchanging pools of spins, labeled a and b, where the independent system variables are defined according to the diagram in Fig. 2.21. The pools are assigned "true" T_2 relaxation times $T_{2a} = 1000\,\text{ms}$ and $T_{2b} = 100\,\text{ms}$, and the "true" amplitudes are defined to be equal ($P_a = P_b = 0.5$). This has the simplifying result that the exchange correlation times are then equal as well ($\tau_a = \tau_b$). Using this model system, the two-site exchange equations were solved to calculate the measured (primed) parameters for $\tau_{a,b}$ ranging from 10^{-1} ms to 10^6 ms (i.e. 100 µs to 16 minutes).

The results of the calculation are shown in Fig. A.1. From these plots, it can be seen that there is limiting behaviour for very large/very small τ (relative to the "true" relaxation times). The regime of $\tau \gg T_{2a}$ is called "slow exchange", and $\tau \ll T_{2b}$ is called "fast exchange"; Between these two extremes lies the regime of "intermediate exchange".

Using the calculated parameter values, the appearance of the signal relaxation curve is simulated in Fig. A.2 for (a) the slow-exchange regime (giving the "true" relaxation times), and for (b) several values of τ in the intermediate or fast exchange regimes.

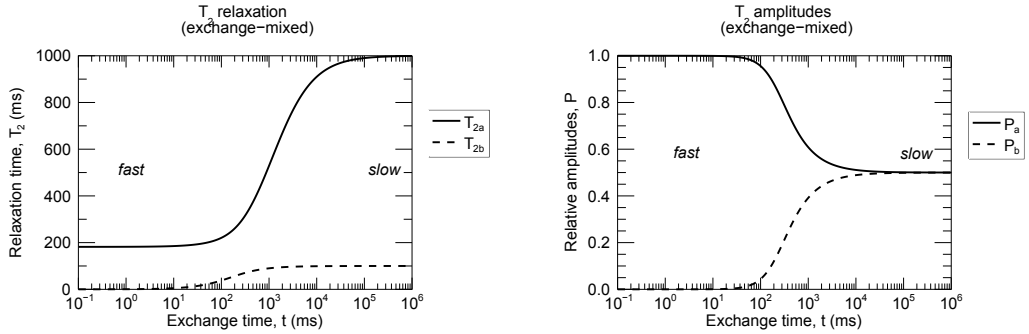

(a) Measured relaxation times

(b) Measured amplitudes

Figure A.1: Two-site exchange simulation for components with $T_2 = 100\,\text{ms}$ and $1000\,\text{ms}$ over a broad range of exchange correlation times (τ). The limits of short/long τ are called fast/slow exchange, respectively.

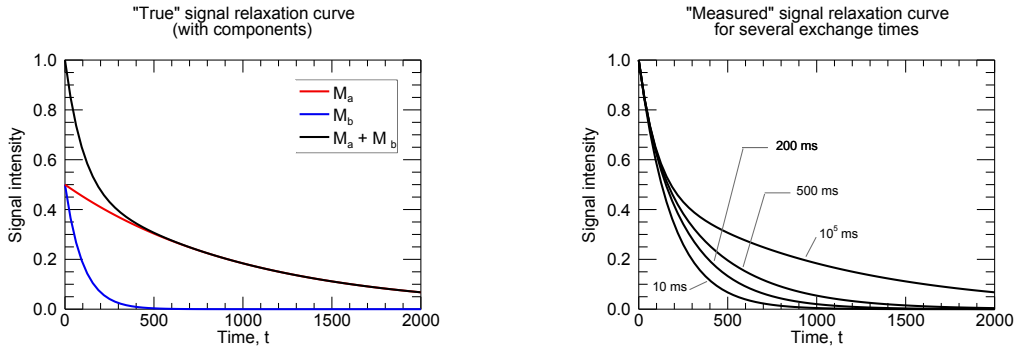

(a)

(b) Relaxation with exchange

Figure A.2: Relaxation with (a) slow or no exchange and (b) with exchange for several values of τ_a. When exchange is fast (short τ), the signal appears monoexponential; when exchange is slow (long τ), the components of the signal are close to the "true" values.

Appendix B

Drug Loading Protocol

The elution studies previously done on CPP disks employed a drug loading protocol designed around the specific size of the disks and the elution apparatus that were used. In the context of an MRI experiment, however, the size and shape of the magnet bore imposes limitations on the size of the disks and on the amount of elution medium that can be used, and the drug loading ratios were adjusted accordingly.

In the following sections, three topics related to the drug loading are explored:

1. the theoretical calculation used to adjust the drug loading for the small disks and elution volume;

2. the method for estimating the theoretical drug mass incorporated into the CPP disks;

3. the evaluation of this loading level via a sink analysis to determine if it is an acceptable one for elution measurements.

B.1 Calculation for Scaled Drug Loading

In previous elution experiments involving G1 and G2 disks, the disks were 2 mm in height and 8 mm in diameter. CPP powder, deionized water, and vancomycin hydrochloride ("VCM") were mixed in the ratio 150 mg : 60.2 µl : 7.5 mg, and the elution experiments were conducted in vessels containing 15 ml of buffered saline [7].

In the MRI experiments, the NMR test tubes were $7''$ long and 4.2 mm in diameter. To adapt the disks to the tube geometry, they were fabricated with half the previous diameter (i.e. 4 mm), and the volume of elution medium was reduced to 1.8 ml.

In practice, the mixing of the drug-loaded CPP paste involves first making a VCM solution of concentration 7.5 mg/60.2 µl = 0.124 mg/µl, then afterwards combining 60.2 µl of that solution with the 150 mg CPP. The amount of VCM used in the smaller

disks was thus scaled simply by adjustment the concentration of the VCM solution used in the mixture.

The principle guiding modification of the amount of VCM in the disks was based on the "worst-case scenario" of release rates. That is: "What would the concentration be if all the drug were released at once?" If this concentration is defined as $C_{\max}$, then the loading for the 4 mm disks in the 1.8 ml NMR tubes was scaled to give the same $C_{\max}$ of the 8 mm disks in the 15 ml elution vessels.

The total volume of the system is 15.10 ml (elution medium + disk). With a loading of 7.5 mg per disk, the "worst-case" concentration would be

$$C_{\max} = \frac{7.5\,\text{mg}}{15.10\,\text{ml}} = 0.4966\,\text{mg/ml}.$$

The smaller disks have 1/2 the diameter (1/4 the volume), and the volume of elution medium is 1.8 ml. If no adjustment were to be made to the VCM ratio in the mixture, the maximum concentration would be

$$C_{\max} = \frac{1.875\,\text{mg}}{1.825\,\text{ml}} = 1.027\,\text{mg/ml}.$$

This would be 2.066× greater than $C_{\max}$ for the large disks, so the amount of VCM used when making the smaller disks must be scaled by this factor, from 7.5 mg to 3.630 mg (giving a VCM solution of 60.29 mg/ml).

In summary, disks were fabricated using a vancomycin solution ($C = 60.39$ mg/ml) that was mixed with raw CPP powder in a ratio of 60.2 µl:150 mg.

B.2 Theoretical Drug Loading Mass

The actual mass of vancomycin in the G1 disks was calculated in the following way.

The theoretical vancomycin mass in the G1 disks was determined using a calculation that tracks the drug mass in three steps of disk fabrication: 1. mass fraction in the drug solution (VCM + H_2O), 2. mass fraction in the wet paste (CPP + VCM solution), then 3. the actual mass in the final, dry disk. Note that symbols are defined only for each step of the calculation (e.g. m_{vcm} in step 1 is not the same as in step 3).

1. Mass fraction in the drug solution (f_1):

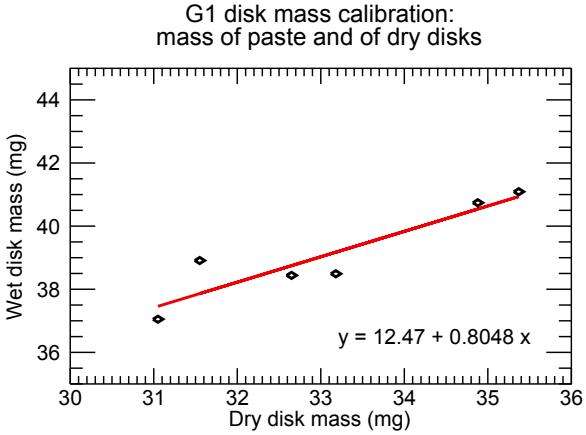

Figure B.1: Calibration for predicting wet disk mass from the dry disk mask for G1 disks.

Vancomycin mass	m_{vcm}		
Water mass	m_w		
Mass fraction	f_1	$=$	$\frac{m_{\mathrm{vcm}}}{m_{\mathrm{vcm}}+m_w}$

2. Mass fraction in the wet paste (f2).

CPP powder mass	m_p		
Mass of VCM solution	m_s		
Mass powder + solution	m_{tot}	$=$	$m_p + m_s$
Vancomycin mass	m_{vcm}	$=$	$f_1\, m_s$
Mass fraction	f_2	$=$	$\frac{f_1\, m_s}{m_{\mathrm{tot}}}$

3. Drug mass in the disk (m_{vcm}). Uses a calibration to estimate wet disk mass from the dry disk mass (see Fig. B.1)

Dry disk mass	x		
Wet disk mass	y		
Calibration equation	y	$=$	$12.47\,\mathrm{mg} + 0.8048\, x$
Vancomycin mass	m_{vcm}	$=$	$f_2\, y$

B.3 Sink Analysis for Reduced Volume of Elution Medium

Models derived for the approximation of drug release behaviour from polymeric devices generally treat the elution medium as a "perfect sink", meaning that drug that

has escaped the device cannot diffuse back into the device. In practice this ideal is never perfectly achieved, but if it can be shown that drug release rates are not affected by changes in the volume of elution medium, then the conditions approximate a perfect sink.

An experiment was performed to assess whether conditions in the NMR elution setup approximated a perfect sink. The primary objective of this experiment to measure the amount of vancomycin released from CPP in three different volumes of phosphate buffer over a 48 hour period. By comparing the drug release profiles from disks in each volume of buffer, it could then be determined whether there is any volume-dependence on the drug elution. Testing was performed over just the first 48 hours of elution, because this is the time period when the drug release is most rapid (and hence there is the greatest risk of violating the perfect sink approximation).

A secondary objective of this experiment was to determine the influence of the calcium and phosphate dissolution products on the VCM absorbance readings at $\lambda = 280\,\text{nm}$. For this reason, blank samples (containing no VCM) were tested as well.

B.3.1 Materials and Methods

Elution Apparatus

Elution and sink analysis have previously been done using cornea viewing chambers to contain the disks and the elution medium, which has the advantage that the buffer volume can easily be adjusted when necessary. However, this form factor leaves all surfaces of the disk exposed, and is quite different from the NMR tubes, which leave only the top surface exposed. Conversely, the NMR tubes can hold a maximum of 1.8 ml of buffer, so testing larger volumes than this requires additional apparatus to provide the buffer reservoir.

A device was created for this purpose using a cut-off NMR tube and a larger, 15 ml Falcon tube (Fig. B.2). As in the regular NMR experiments, CPP disks were mounted on Ultem spacers and fastened in the tubes using cyanoacrylate, but the tubes were cut off 5 mm above the disk bottom. This was done to allow mixing of the buffer in the NMR tube with buffer in the larger reservoir of the Falcon tube, as well as to allow the disk to swell to its full height. To keep the NMR tube standing upright, a sheath was fashioned from the end of a glass pipette and fitted around the

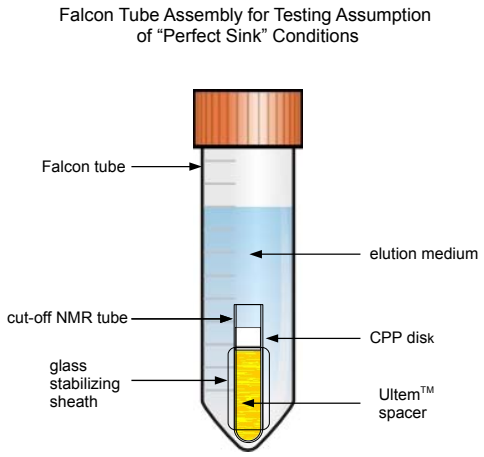

Figure B.2: An NMR tube mounted in a Falcon tube provides a larger volume for sink analysis.

bottom of the tube.

The volumes used for the sink analysis were 1.8 ml (the maximum volume held by a NMR tube), 14.0 ml (the maximum volume held by a Falcon tube with disk/NMR tube fixture inside), and 7.9 ml (the midpoint of the other two volumes).

CPP Disks

G1 disks loaded with vancomycin (VCM) were prepared according to the procedure in Chapter 3. Because the aim of this experiment was to investigate the dependence (or lack thereof) of drug release on elution volume, *only* G1 disks were used. This is because G1 disks are known to release drug at greater rates than G2 disks, and therefore provide the more aggressive test of the limits of concentration effects.

For each of the three volumes used, five CPP disks were fabricated—four loaded with VCM and one left blank, containing no drug.

B.3.2 Procedure

The disks were set up in the elution apparatus, and at $t = 0$ hours the sample tubes were filled with the 1.8, 7.9, or 14.0 ml volume of phosphate buffer (0.14 M, pH 7.2). The samples were stored on an orbital lab shaker rotating at (40 ± 2) rpm.

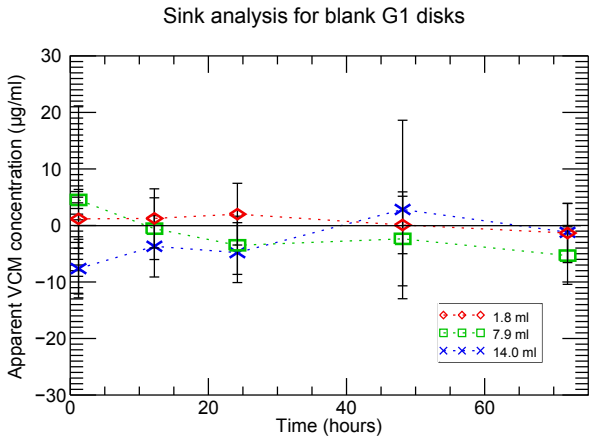

Figure B.3: Apparent vancomycin absorbance in the blank samples exhibits no dependence on the elution volume. Within uncertainty, the readings from the blank samples are effectively zero.

At times $t = 1$, 12, 24, 48, and 72 hours, the elution medium was sampled in the standard way, and the concentrations were used to calculate the mass of vancomycin that had been eluted.

B.3.3 Results

Absorbance Readings From Blank Samples

The absorbance readings (converted to µg/ml using the VCM calibration) from the blank samples for all three volumes are plotted in Fig. B.3. The readings are zero, within uncertainty, which shows that the presence of dissolved calcium and phosphorous degradation products do not influence the vancomycin absorbance readings.

Vancomycin Release

The cumulative vancomycin release is shown in Fig. B.4. Even accounting for the uncertainties, the plot does not strictly show agreement between all points at all times—at some times one point will appear to deviate significantly from the others. However, there does not seem to be any trend to these deviations, and they do not occur consistently for one volume over another. These observations suggest that vancomycin release does not depend on buffer volume in the range of 1.8 – 14.0 ml.

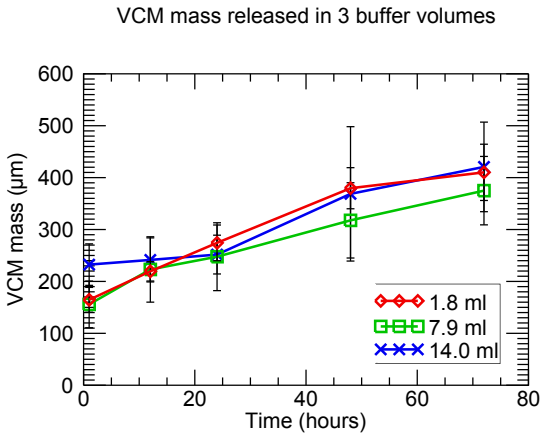

Figure B.4: Cumulative vancomycin mass released over time in buffer volumes of 1.8, 7.9, and 14.0 ml. The uncertainties shown are the standard deviations for $n = 4$ samples, and (for comparison).

B.3.4 Conclusions

Vancomycin release was measured from G1 disks in a range of buffer volumes from 1.8 ml – 14.0 ml. From measurements performed on unloaded (blank) disks, it was determined that the presence of dissolved CPP degradation by-products (calcium and phosphorous) had no effect on the vancomycin absorbance measurements. Furthermore, it was found that there is no significant difference in release rates of vancomycin for buffer volumes in the range 1.8 – 14.0 ml. Because of this, the conditions in the elution setup approximate a perfect sink.

Bibliography

[1] J. C. Richardson, R. W. Bowtell, K. Mäder, and C. D. Melia. Pharmaceutical applications of magnetic resonance imaging (MRI). *Adv. Drug Del. Rev.*, 57:1191–1209, 2005.

[2] C. D. Melia, A. R. Rajabi-Siahboomi, and R. W. Bowtell. Magnetic resonance imaging of controlled release pharmaceutical dosage forms. *Pharm. Sci. Technol. To.*, 1(1):32–39, April 1998.

[3] D. W. Haas and M. P. McAndrew. Bacterial osteomyelitis in adults: evolving considerations in diagnosis and treatment. *Am. J. Med.*, 101:550–561, 1996.

[4] P. D. Holtom and A. M. Smith. Introduction to adult posttraumatic osteomyelitis of the tibia. *Clin. Orthoped. Relat. Res.*, (360):6–13, 1999.

[5] A. Dion, B. Berno, G. Hall, and M. J. Filiaggi. The effect of processing on the structural characteristics of vancomycin-loaded amorphous calcium phosphate matrices. *Biomaterials*, 26:4486–4494, 2005.

[6] A. Dion, M. Langman, G. Hall, and M. Filiaggi. Vancomycin release behaviour from amorphous calcium polyphosphate matrices intended for osteomyelitis treatment. *Biomaterials*, 26(35):7276, 2005.

[7] C. Petrone, G. Hall, M. Langman, and M. J. Filiaggi. Compaction strategies for modifying the drug delivery capabilities of gelled calcium polyphosphate matrices. *Acta Biomater.*, 4(2):403–413, March 2008.

[8] D. T. Tsukayama. Pathophysiology of posttraumatic osteomyelitis. *Clin. Orthoped. Relat. Res.*, (360):22–29, 1999.

[9] L. Lazzarini, J. T. Mader, and J. H. Calhoun. Osteomyelitis in long bones. *J. Bone Joint Surg. Am.*, 86-A(10):2305–2318, 2004.

[10] J. T. Mader, D. Mohan, and J. Calhoun. A practical guide to the diagnosis and management of bone and joint infections. *Drugs*, 54(2):253–264, 1997.

[11] C. L. Nelson, S. G. McLaren, R. A. Skinner, M. S. Smeltzer, J. R. Thomas, and K. M. Olsen. The treatment of experimental osteomyelitis by surgical debridement and the implantation of calcium sulfate tobramycin pellets. *J. Orthop. Res.*, 20(4):643, 2002.

[12] K. Adams, L. Couch, G. Cierny, J. Calhoun, and J.T. Mader. In vitro and in vivo evaluation of antibiotic diffusion from antibiotic-impregnated polymethylmethacrylate beads. *Clin. Orthoped. Relat. Res.*, 278:244–52, 1992.

[13] R.C. Ropp. *Inorganic Polymeric Glasses*, volume 15 of *Studies in Inorganic Chemistry*. Elsevier, 1992.

[14] R. Z. LeGeros. Properties of osteoconductive biomaterials: calcium phosphates. *Clin. Orthoped. Relat. Res.*, (395):81–98, 2002.

[15] A. Lasserre and P. K. Bajpai. Ceramic drug-delivery devices. *Crit. Rev. Ther. Drug. Carrier*, 15(1):1–56, 1998.

[16] J.H. Calhoun and J.T. Mader. Treatment of osteomyelitis with a biodegradable antibiotic implant. *Clin. Orthoped. Relat. Res.*, 341:206–14, 1997.

[17] M. D. Grynpas, R. M. Pilliar, R. A. Kandel, R. Renlund, M. Filiaggi, and M. Dumitriu. Porous calcium polyphosphate scaffolds for bone substitute applications—in vivo studies. *Biomaterials*, 23(9):2063–2070, May 2002.

[18] D. Shi. *Biomedical Devices and Their Applications*. Springer, Germany, 2004.

[19] E. M. Haake, R. W. Brown, M. R. Thompson, and R. Venkatesan. *Magnetic Resonance Imaging—Physical Principles and Sequence Design*. Wiley, New York, 1999.

[20] N. Bloembergen, E. M. Purcell, and R. V. Pound. Relaxation effects in nuclear magnetic resonance absorption. *Phys. Rev.*, 73(7):679–712, 1947.

[21] P. T. Callaghan. *Principles of Nuclear Magnetic Resonance Microscopy*. Oxford University Press, New York, 1993.

[22] B. Blümich. *NMR Imaging of Materials*, chapter 10.1, pages 424–439. Oxford, New York, 2000.

[23] J. M. Bray, C. Petrone, M. Filiaggi, and S. D. Beyea. Measurement of fluid ingress into calcium polyphosphate bioceramics using nuclear magnetic resonance microscopy. *Solid State Nucl. Magn. Reson.*, 32(4):118–128, December 2007.

[24] L. L. Hench. Bioceramics. *J. Am. Ceram. Soc.*, 81(7):1705–1728, 1998.

[25] W. Paul and C. P. Sharma. Ceramic drug delivery: a perspective. *J. Biomater. Appl.*, 17:253–264, 2003.

[26] R. M. Pilliar, M. J. Filiaggi, J. D. Wells, M. D. Grynpas, and R. A. Kandel. Porous calcium polyphosphate scaffolds for bone substitute applications—in vitro characterization. *Biomaterials*, 22(9):963–972, 2001.

[27] R. A. Jain. The manufacturing techniques of various drug loaded biodegradable poly(lactide-co-glycolide) (PLGA) devices. *Biomaterials*, 21(23):2475–2490, December 2000.

[28] A. Djemai, L.F. Gladden, J. Booth, R.S. Kittleby, and P.R. Gellert. MRI investigation of hydration and heterogeneous degradation of aliphatic polyesters derived from lactic and glycolic acids: a controlled drug delivery device. *Magn. Reson. Imag.*, 19:521–523, 2001.

[29] R. P. Evans and C. L. Nelson. Gentamicin-impregnated polymethylmethacrylate beads compared with systemic antibiotic therapy in the treatment of chronic osteomyelitis. *Clin. Orthoped. Relat. Res.*, (295):37–42, 1993.

[30] A. Krajewski, A. Ravaglioli, E. Roncari, P. Pinasco, and L. Montanari. Porous ceramic bodies for drug delivery. *J. Mater. Sci. Mater. Med.*, 12:763–771, 2000.

[31] A. Sinha, A. Ingle, K. R. Munim, S. N. Vaidya, B. P. Sharma, and A. N. Bhisey. Development of calcium phosphate based bioceramics. *Bull. Mater. Sci.*, 24(6):653–657, 2001.

[32] C.X. Wang, X. Zhou, and M. Wang. Influence of sintering temperature on hardness and Young's modulus of tricalcium phosphate bioceramic by nanoindentation technique. *Mater. Charact.*, 52:301–307, 2004.

[33] E. Landi, L. Orlandi, G. Spagna, A. Tampieri, and N. Zaffaroni. Calcium phosphate ceramics as drug-delivery system for anticancer therapy. In *Key Engineering Materials*, pages 901–904. Trans Tech Publications, Switzerland, 2001.

[34] L. M. Rodriguez-Lorenzo and J. M. F. Ferreira. Development of porous ceramic bodies for applications in tissue engineering and drug delivery systems. *Mater. Res. Bull.*, 39:83–91, 2004.

[35] K. A. Hing, S. M. Best, and W. Bonfield. Characterization of porous hydroxyapatite. *J. Mater. Sci. Mater. Med.*, 10(3):135–145, March 1999.

[36] D. J. A. Netz, P. Sepulveda, V. C. Pandolfelli, A. C. C. Spadaro, J. B. Alencastre, M. V. L. B. Bentley, and J. M. Marchetti. Potential use of gelcasting hydroxyapatite porous ceramic as an implantable drug delivery system. *Int. J. Pharm.*, 213(1-2):117–125, February 2001.

[37] K. Qiu, C. Wan, C. Zhao, X. Chen, C. Tang, and Y. Chen. Fabrication and characterization of porous calcium polyphosphate scaffolds. *J. Mater. Sci.*, 41(8):2429–2434, April 2006.

[38] A. Dion. The evaluation of calcium polyphosphates as antibiotic delivery matrices for bone replacement applications. Master's thesis, Dalhousie University, 2003.

[39] M.J. Filiaggi, J.D. Wells, S.A.F. Peel, R.M. Pilliar, M.D. Grynpas, and R.A. Kandel. Condensed calcium phosphates for soft tissue and bone repair / regeneration. In R.Z. LeGeros and J.P. LeGeros, editors, *Bioceramics (Proceedings of the 11th International Symposium on Ceramics in Medicine)*, volume 11, pages 341–344. World Scientific Publishing Co. Pte. Ltd., 1998.

[40] H. Yuan, Z. Yang, Y. Li, X. Zhang, J. D. De Bruijn, and K. De Groot. Osteoinduction by calcium phosphate biomaterials. *J. Mater. Sci. Mater. Med.*, 9(12):723–726, December 1998.

[41] M. Filiaggi and G. Hall. A compaction route for low temperature processing of porous calcium polyphosphate matrices. In S. Brown, I. Clarke, and P. Williams, editors, *Proceedings of the 14th International Symposium on Ceramics in Medicine*, volume 14 of *Bioceramics*. Switzerland : Trans Tech Publications, 2002., 2001.

[42] T. Kasuga, T. Wakita, M. Nogami, M. Saurai, M. Watanabe, and Y. Abe. Hydrogelation of calcium metaphosphate glass. *Chem. Lett.*, 8:820–821, 2001.

[43] J. R. van Wazer. *Phosphorus and Its Compounds*. New York, Interscience Publishers, 1961.

[44] S. Ohashi and J. R. van Wazer. Structure and properties of the condensed phosphates. XIV. Calcium polyphosphates. *J. Am. Chem. Soc.*, 81:830–832, 1958.

[45] A. Durif. *Crystal Chemistry of Condensed Phosphates*. New York : Plenum Press, 1995.

[46] I. S. Kulaev. *The Biochemistry of Inorganic Polyphosphates*. Wiley InterScience, 1979.

[47] B. C. Bunker, G. W. Arnold, and J. A. Wilder. Phosphate glass dissolution in aqueous solutions. *J. Non-Crystalline Solids*, 64(3):291–316, May 1984.

[48] N. Djogbenou, U. Werner-Zwanziger, and M. J. Filiaggi. Monitoring structural changes occurring during gelation of calcium polyphosphate drug delivery matrices. World Biomaterials Congress, May 2008.

[49] N. Djogbenou. Understanding the interaction of amorphous calcium polyphosphate with aqueous environments to optimize its use as a localized drug delivery matrix. Master's thesis, Dalhousie, 2009.

[50] A. R. Rajabi-Siahboomi, R. W. Bowtell, P. Mansfield, A. Henderson, M. C. Davies, and C. D. Melia. Structure and behaviour in hydrophilic matrix sustained release dosage forms: 2. NMR-imaging studies of dimensional changes in the gel layer and core of HPMC tablets undergoing hydration. *J. Control. Release*, 31(2):121–128, 1994.

[51] A. R. Rajabi-Siahboomi, R. W. Bowtell, P. Mansfield, M. C. Davies, and C. D. Melia. Structure and behavior in hydrophilic matrix sustained release dosage forms: 4. Studies of water mobility and diffusion coefficients in the gel layer of HPMC tablets using NMR imaging. *Pharm. Res.*, 13:376–380, 1996.

[52] C.A. Fyfe and A.I. Blazek. Investigation of hydrogel formation from hydroxypropylmethylcellulose (HPMC) by NMR spectroscopy and NMR imaging techniques. *Macromolecules*, 30(20):6230–6237, October 1997.

[53] C.A. Fyfe and A.I. Blazek-Welsh. Quantitative NMR imaging study of the mechanism of drug release from swelling hydroxypropylmethylcellulose tablets. *J. Control. Release*, 68(3):313–333, 2000.

[54] C. Dahlberg, A. Fureby, M. Schuleit, S. V. Dvinskikh, and I. Furo. Polymer mobilization and drug release during tablet swelling—a ^{1}H NMR and NMR microimaging study. *J. Control. Release*, 122(2):199–205, September 2007.

[55] S. Gravina and D. G. Cory. Sensitivity and resolution of constant-time imaging. *J. Magn. Reson. Imaging*, 104(1):53–61, 1994.

[56] J.E.M. Snaar, R. Bowtell, C.D. Melia, S.Morgan, B. Narasimhan, and N.A. Peppas. Self-diffusion and molecular mobility in PVA-based dissolution-controlled systems for drug delivery. *Magn. Reson. Imag.*, 16:691–694, 1998.

[57] B. Narasimhan and N. A. Peppas. On the importance of chain reptation in models of dissolution of glassy polymers. *Macromolecules*, 29:3281–3291, 1996.

[58] G. E. Milroy, R. E. Cameron, M. D. Mantle, L. F. Gladden, and H. Huatan. The distribution of water in degrading polyglycolide. Part II: magnetic resonance imaging and drug release. *J. Mater. Sci. Mater. Med.*, 14(5):465–473, May 2003.

[59] K. Mäder, Y. Crémmilleux, A. J. Domb, J. R. Dunn, and H. M. Swartz. In vitro/in vivo comparison of drug release and polymer erosion from biodegradable P(FAD-SA) polyanhydrides—a noninvasive approach by the combined use of electron paramagnetic resonance spectroscopy and nuclear magnetic resonance imaging. *Pharm. Res.*, 14:820–826, 1997.

[60] C. Ramanathan and J.L. Ackerman. Quantitative solid-state NMR imaging of synthetic calcium phosphate implants. *Magn. Reson. Med.*, 41:1214–1220, 1999.

[61] M. Marcos, P. Cano, P. Fantazzini, C. Garavaglia, S. Gomez, and L. Garrido. NMR relaxometry and imaging of water absorbed in biodegradable polymer scaffolds. *Magn. Reson. Imag.*, 24(1):89–95, 2006.

[62] D. J. Griffiths. *Introduction to Quantum Mechanics*. Prentice Hall, New Jersey, 1995.

[63] J. T. Bushberg, J. A. Seibert, E. M. Leidhold, and J. M. Boone. *The Essential Physics of Medical Imaging*. Lippincott Williams & Wilkins, Philidelphia, 2002.

[64] H. Y. Carr and E. M. Purcell. Effects of diffusion on free precession in nuclear magnetic resonance experiments. *Phys. Rev.*, 94(3):630–, May 1954.

[65] S. Meiboom and D. Gill. Modified spin-echo method for measuring nuclear relaxation times. *Rev. Sci. Instrum.*, 29(8):688–691, August 1958.

[66] H. S. Gutowsky and C. H. Holm. Rate processes and nuclear magnetic resonance spectra. II. Hindered internal rotation of amides. *J. Chem. Phys.*, 25(6):1228–1234, December 1956.

[67] Z. Luz and S. Meiboom. Nuclear magnetic resonance study of the protolysis of trimethylammonium ion in aqueous solution—order of the reaction with respect to solvent. *J. Chem. Phys.*, 39(2):366–370, July 1963.

[68] Adam Allerhand and H. S. Gutowsky. Spin-echo NMR studies of chemical exchange. I. Some general aspects. *J. Chem. Phys.*, 41(7):2115–2126, October 1964.

[69] M. D. Herbst and J.H. Goldstein. A review of water diffusion measurement by NMR in human red blood cells. *Am. J. Physiol.*, 256:1097–1104, 1989.

[70] E.O. Stejskal and J.E. Tanner. Spin diffusion measurements: spin echoes in the presence of a time-dependent field gradient. *J. Chem. Phys.*, 42:288–292, 1965.

[71] R. Kerssebaum. *DOSY and Diffusion by NMR.* Bruker BioSpin GmbH, Rheinstetten, Germany, 1.0 edition, 2002.

[72] H. Johansen-Berg and T. E.J. Behrens, editors. *Diffusion MRI: From Quantitative Measurement to in vivo neuroanatomy.* Elsevier Inc., first edition, 2009.

[73] S. Omelon, A. Baer, T. Coyle, R.M. Pilliar, R. Kandel, and M. Grynpas. Polymeric crystallization and condensation of calcium polyphosphate glass. *Mater. Res. Bull.*, 43(1):68–80, 2008.

[74] X.-A. Mao and C.-H. Ye. Understanding radiation damping in a simple way. *Conc. Magn. Res.*, 9:173–187, 1997.

[75] M. A. Connell, P. J. Bowyer, P. A. Bone, A. L. Davis, A. G. Swanson, M. Nilsson, and G. A. Morris. NMR measurements of diffusion in concentrated samples: avoiding problems with radiation damping. *Anal. Bioanal. Chem.*, 378(6):1568–1573, 03 2004.

[76] W. S. Price, P. Stilbs, B. Jönsson, and O. Söderman. Macroscopic background gradient and radiation damping effects on high-field PGSE NMR diffusion measurements. *J. Magn. Reson.*, 150(1):49–56, May 2001.

[77] Y. P. Syrnikov. Calculation of the self-diffusion coefficient of water. *J. Struct. Chem.*, 11(4):698–700, July 1971.

[78] Y. I. Tarasevich and G. M. Klimova. Complex-forming adsorbents based on kaolinite, aluminium oxide and polyphosphates for the extraction and concentration of heavy metal ions from water solutions. *Appl. Clay Sci.*, 19(1-6):95–101, July 2001.

[79] C. B. Markwardt. Non-linear least-squares fitting in IDL with MPFIT. In D. Bohlender, P. Dowler, and D. Durand, editors, *Astronomical Data Analysis Software and Systems XVIII*, volume 411, pages 251–254. Quebec, Canada, ASP Conference Series, Astronomical Society of the Pacific: San Francisco, 2008.

[80] D. W. Oxtoby, H.P. Gillis, and N. H. Nachtrieb. *Principles of Modern Chemistry*. Saunders College Publishing, fourth edition, 1999.

[81] E. McGown. UV absorbance measurements in SpectraMax microplate spectrophotometers (MaxLine application note #32). internet, July 1999.

[82] J. Siepmann and N. A. Peppas. Modeling of drug release from delivery systems based on hydroxypropyl methylcellulose (HPMC). *Adv. Drug Del. Rev.*, 48(2-3):139–157, June 2001.

[83] N. A. Peppas. Analysis of Fickian and non-Fickian drug release from polymers. *Pharm. Acta Helv.*, 60(4):110–111, 1985.

[84] T. Dürig and R. Fassihi. Mechanistic evaluation of binary effects of magnesium stearate and talc as dissolution retardants at 85% drug loading in an experimental extended-release formulation. *J. Pharm. Sci.*, 86(10):1092–1098, 1997.

[85] C. Petrone. Degradable calcium polyphosphate compaction strategies for the delivery of therapeutic agents. Master's thesis, Dalhousie, 2005.

[86] N. A. Peppas and L. BrannonPeppas. Water diffusion and sorption in amorphous macromolecular systems and foods. *J. Food Eng.*, (1-4):189–210, 1994.